Unione Europea

Università degli Studi di Salerno

DIPARTIMENTO DI INGEGNERIA MECCANICA

Dottorato di Ricerca in Ingegneria Meccanica
IX Ciclo N.S. (2007-2010)

"Innovative techniques for Structural Health Monitoring: a theoretical and experimental study"

Ing. Rossella Valiante

Tutor:
Prof. Domenico Guida
Co-Tutor:
Prof. Fernando Fraternali
Ing. Generoso Iannuzzo (Alenia)

Coordinatore:
Prof. Vincenzo Sergi

The present work, carried out at Alenia Aeronautica, contains sensitive information and data covered by the Intellectually Property Rights. Therefore, the use of such information and data is allowed only under permission of Alenia Aeronautica.

RINGRAZIAMENTI

E' per me doveroso, oltre che sentito, ringraziare l'ing. Iannuzzo, il quale, oltre ad avermi supportato come tutor nella stesura del presente lavoro, mi ha, innanzitutto, concesso la preziosa possibilità di affrontare quest'avventura.

Vorrei, inoltre, dire il mio forte grazie al prof. Guida che, non pago di avermi sopportato durante la tesi di laurea, mi ha invogliato a tentare questo arduo percorso, ancora una volta sotto la sua guida.

Un ringraziamento particolare lo dedico al prof. Fraternali, il quale mi ha fornito lo sprone necessario a seguitare col lavoro di dottorato, oltre ad avermi guidata attentamente nella stesura dello stesso.

Non posso dimenticare il prof. Ruzzene, che mi ha introdotto nel mondo delle onde di Lamb, né la sua collaboratrice, Nicole Apetre, la quale tanti preziosi consigli sulla modellazione numerica delle stesse mi ha dispensato.

Tengo particolarmente a ringraziare il Prof. D'Agostino che, col garbo che lo contraddistingue, ha seguito, seppur da lontano, quest'altro mio percorso di studi, dandomi sempre l'impagabile sensazione di sentirmi a casa ogniqualvolta mettessi piede a Fisciano.

Ringrazio il nostro Coordinatore, Prof. Vincenzo Sergi, per la gestione ineccepibile del corso di dottorato, accompagnata sempre da atteggiamento disponibile e cortese.

Dico grazie infinite a Pierpaolo D'Agostino, che mi ha più volte salvato dal panico 'da dottorato', oltre che aiutato fattivamente in questi tre anni sempre col sorriso sulle labbra. Grazie, Pierpaolo!

Non posso dimenticare Luca, Rosario, e tutte le persone coinvolte nel coordinamento del corso, né i miei colleghi d'avventura, Roberta, Marzia, Gino, Renzo, sempre disponibili e gentili.

Vorrei, inoltre, ringraziare il collega Michele Rotondano, per il suo fondamentale contributo informatico.

Un mega grazie va alla mia amica, nonché collega, Maria Pagano, per la preziosa collaborazione ed il supporto morale! Merci, Mary!

Particolarmente doveroso ed al contempo piacevole per me ringraziare Damiano Laurenza, il quale mi ha fornito aiuto concreto, oltre ad avermi spronata ad ogni ostacolo incontrato sulla via. Grazie!

Tengo a dire grazie alle mie super amiche Ylenia e Stefania, per l'incoraggiamento continuo ricevuto, sempre e comunque. Grazie, tesorucce!

Ringrazio l'Amico cui devo moltissimo, don Dolindo; un ringraziamento particolare lo dedico a don Peppino, imprescindibile presenza di questi anni.

Un grazie speciale lo dedico alla persona più che speciale che mi ha letteralmente sopportato, oltreché sopportato in questo periodo, con una presenza delicata e costante. Grazie di cuore.

Vorrei, infine, disporre del vocabolario di Dante per dire grazie alle persone della mia famiglia, papà, mamma e Pina, le quali mi hanno dato, ciascuna a proprio distintivo ed unico modo, la forza di raggiungere il traguardo. Vi amo.

A PAPÀ, MAMMA E PINA,

RISPETTIVAMENTE IL MIO CUORE,

LA MIA ANIMA E

LA MIA GEMELLA SIAMESE

CONTENTS

LIST OF FIGURES AND TABLES

ABSTRACT OF DISSERTATION

Aerospace industry is characterized by continuously growing safety cost requirements. This fact leads to the exponential increase in the use of composite materials. With such feature as high strength-to-weight and stiffness to weight ratios, these materials allow the manufacturing of lighter and more efficient structure, with respect to aluminum alloys, in order to increase the payload and to reduce the fuel consumption. However, composite structures are very vulnerable to structural damage, in particular to the delamination that can be introduced during manufacturing or service. The occurrence of delamination could potentially lead to a catastrophic failure of the whole structure, if it accumulates above a critical level. Cost saving must never be considered without safety. For this reason, in the last years researchers have been developing ever more sophisticated damage monitoring systems, which are able to evaluate the health of a structure in real-time. This branch of research is known as Structural Health monitoring (SHM).

This study investigates the use of Lamb waves and laser vibrometry for the identification and localization of damage/defects occurring within critical components of aircraft structure. In the present study, a SHM strategy based on dynamic structural analysis performed over a wide frequency range is presented. The frequency band of investigation spans from the lowest mode of the structure up to the low ultrasonic range, and so, potentially, it allows the detection of various sizes of defects. The tests are performed using a single actuator/sensor pair: piezoelectric discs are employed as actuators, while a Scanning Laser Doppler Vibrometer is used as a sensing device. The piezoceramic discs are inexpensive and easy to operate and the Scanning Laser Doppler Vibrometer measures the velocity of the structure at points on a user-defined grid, thus providing an unprecedented amount of information.

The aim is to obtain a comprehensive structural monitoring methodology able to overcome drawbacks and exploit advantages of various techniques. In the low-to-medium frequency range, modal parameters are normally less sensitive to localized defects, but generally provide indications regarding global changes as a result of damage. Such changes localize defects and potentially estimate their severity. In addition to modal monitoring, the Scanning Laser Doppler Vibrometer is used as an ultrasonic sensor. The two techniques are applied sequentially: vibration-based monitoring first provides indication of potential areas of damage, on which the scanning laser Doppler vibrometer then focuses to perform ultrasonic testing and to obtain detailed damage information. The technique is demonstrated experimentally on plate-like stringerized structures affected by artificial delaminations or by wrinkling caused by manufacturing process and, subsequentially, on numerical models of the previous tested components. The approach followed in this thesis is divided into five chapters.

The first one presents a description of the SHM, along with the state of the art on this technique. Moreover a brief introduction to the theory of waves in solid materials is provided. Then, in the second chapter the description of the two innovative SHM techniques (i.e. the signal filtering technique in wavenumber-frequency domain and the comprehensive damage index), developed by Ruzzene and on which this work relies on, is extensively described. The third chapter is centered on the innovative experimental analysis carried out at Alenia Aeronautica laboratories in Pomigliano. An explanation of the experimental setup is provided along with the obtained results. Then, the post-processing techniques, explained in the previous chapter, are applied and the obtained results are reported. In the fourth chapter the two adopted FE modeling techniques (with CQUAD4 elements and with HEX8 elements) are extensively described, focusing on the possibility of correctly modeling the wave propagation in composite strengthened plates through the use of the finite element method (there are no published works in this field, regarding strengthened panels). This is no trivial task because of the complex nature of wave propagation in plates, especially for the composite materials case. Then, the confrontation between experimental data and the numerical approach is reported. In the fifth chapter conclusions and future work are reported.

The most significant technological innovations achieved through this work are:

- The option key to excite the surface of a complex structure (in this case, the skin of a composite stringerized panel) and to derive the velocity profile on a surface which is orthogonal to the excited one (in our case the web of the stringer) has been checked. Obviously, in such a way, it is also automatically validated the opposite approach. This is crucial, since it would allow technicians to install fixed piezo elements on the stringers, to excite them (when the plane is in the hangar) and to read velocities of points over the entire surface of the skin, without disassembly. A configuration of great practical utility may be obtained permanently placing some actuators on the two opposite sides of the web and measuring the response on the external side of the skin, easily accessible.
- Up to now, only cases of standard solicitation (i.e. cases in which the velocities were acquired on the same surfaces excited) have been analyzed in literature.
- The Damage Index has been also applied to greatly complex geometries. Up to now, in literature only articles concerning tests on simple flat panels can be found.
- The FEM simulation has been carried out on stiffened panels. In literature, only works regarding simulations carried out on simple structural elements like flat panels without any stiffener can be found.

1. INTRODUCTION

All civil, mechanical and aerospace structures are subject to damage as a result of fatigue, overloading conditions, material degradation through environmental effects and unanticipated discrete events such as impacts or seismic events. Damage compromises the ability of the structure to perform its primary functions. Therefore, to ensure performance standards, extend the operational lifespan and maintain life-safety, many structural systems undergo routine inspections and maintenance. Common non-destructive evaluation (NDE) methods for evaluating the integrity of a structural component include the use of Eddy currents, acoustic emission, ultrasonic inspection, radiography, thermography or just basic visual inspections [1]. Depending upon the structural system, the cost associated with systematic time-based NDE inspection and maintenance can be substantial relative to the total life-cycle costs of the system. For commercial and military aircraft, it is estimated that 27% of the average life cycle costs are related to inspection and repair [2]. In addition, there is a corresponding opportunity cost associated with the loss in operational availability during maintenance. Within the aircraft industry in particular, maintenance procedures are dependent upon the design methodology adopted for the vehicle components.

The two dominant design methodologies are safe-life and damage tolerant [1]. For safe-life design, the operational lifespan of structural components is estimated through a statistical analysis. Inspection is not necessary for this methodology, since the components are simply replaced prior to its specified design life. As a result, safe-life design is the least economical. Currently, many aircrafts are designed according to damage tolerant methodology. In this approach, models are used to predict the emergence of damage in various components under specified loading conditions. Based upon these models, NDE (Non Destructive Evaluation) inspection and preventive maintenance is performed at frequent time intervals to identify incipient damage and to prevent critical damage growth. An effort is currently being made to implement a newer condition based design methodology. In this case, maintenance is only performed when the system has undergone damage beyond a tolerable level.

Ideally, routinely scheduled inspection would be replaced by the integration of a built-in structural health monitoring (SHM) system that can perform continuous on-line diagnostics as well as prognostics. The objective for the diagnostics is to perform damage identification while the prognostics allows for an estimation of the remaining useful life of the system. Condition based maintenance, based upon a SHM philosophy, is the most economical option. Ideally, an SHM system will increase the operational availability, extend the lifespan of an aircraft, enhance life-safety and dramatically reduce life-cycle costs. It is estimated that a savings of 40% on inspection time and 20% on inspection/maintenance costs could result from the implementation of a properly designed SHM system [1].

The function of an SHM system is to collect periodically sampled dynamic response measurements of the structure using an integrated network of strategically placed transducers [3]. From these measurements, extracted damage sensitive features are then used to solve a forward or inverse problem with system models or applied in statistical pattern recognition algorithms in order to evaluate the structural condition of the system.

One of the primary objectives of an SHM system is damage identification. Damage identification can be organized into a hierarchical pattern as follows [4]:

Level 1 (Damage Detection): Recognition that damage exists within the structure

Level 2 (Damage Localization): identification of the geometric position of damage

Level 3 (Damage Classification): Classification of damage type when multiple damage scenarios exist

Level 4 (Damage Assessment): Quantification of damage extent

Level 5 (Damage Prediction): Estimation of residual life of the structure.

1.1. GENERAL SHM PARADIGM

Damage identification in accordance with an SHM paradigm involves progressive stages. According to Sohn at al. [3] and Worden and Dulieu-Barton [4], this sequential process includes operational evaluation, data acquisition, signal processing, feature extraction and statistical pattern processing (Fig. 1.1).

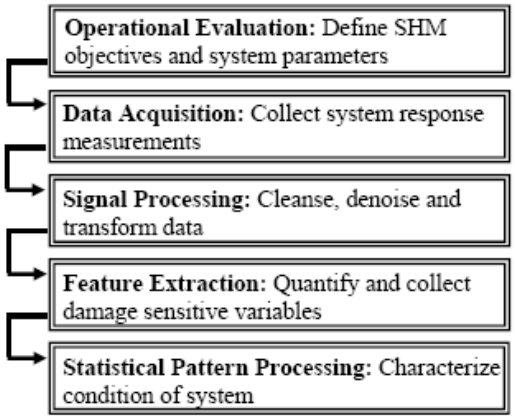

Fig. 1.1 - Scheme of SHM based damage identification process.

The operational evaluation entails the appraisal of economic and life safety motives for the SHM system, definition of damage within the structure, determination of the operational and environmental conditions under which the structure is subjected and how this may affect the ability for data acquisition, which involves the collection of the dynamic response measurements in the system.

Signal processing, which includes data cleansing, denoising and data transformation, is paramount in the damage identification procedure. Common methods of data cleansing and de-noising include digital or analogical filters, signal averaging and more recently, the use of discrete wavelet transform and of multi-dimensional Fourier transforms.

Feature extraction consists of quantifying and collecting damage sensitive variables. For enhanced damage identification reliability, it is necessary to carefully select features that allow for maximum sensitivity to the particular damage of interest while also ensuring that their sensitivity to operational and environmental variability is minimal. Due to likely stringent memory and processing limitations of on-board applications, features should be dimensionally low and computationally simple.

1.2. DEFINITION OF DAMAGE IN CFRP COMPOSITE COMPONENTS

Damage can be defined as changes in the material, geometry or connectivity of the system that adversely affect its current or future performance. Although defects exist within any engineering material at the microscopic level, it is generally accounted for in the initial design of the structure, such as through the appropriate designation of material yield strength. As a result, the system can still perform according to the optimal design specifications. Contrarily, damage results in system performance below idealized conditions. Common damage sources include fatigue, overloading conditions, material degradation through environmental effects, and unanticipated discrete events such as impacts or seismic events. Carbon Fiber Reinforced Polymer (CFRP) composites are becoming widely used within the aerospace industry due to its very high specific strength and stiffness properties. However, FRP composites are also quite susceptible to various forms of damage. Common damage modes within FRP composites include matrix cracking, delamination, and fiber breakage [28].

For composite laminates, delamination is a major concern, since this can significantly reduce the load carrying capacity of the laminate. Unlike metallic structures, which are homogenous and have the ability to dissipate energy through yielding, composite structures are relatively brittle and exhibit weak interfacial strength between laminae. As a consequence, even low velocity impacts on FRP composites can introduce significant delamination that is not visible from the surface. In addition to the laminate damage described above,

damage mechanisms in composite panels include core-face sheet debonding and core crushing [29]. The debonding between core and face sheet is a more prominent damage source for the reason that it can be induced by transverse loading conditions, such as low-velocity impact. Although the damage mechanisms described above may be the primary concern for many applications, they do not necessarily constitute the most critical type of damage that can occur in a composite structure. For many structural systems, the connection joints of individual load bearing members are critical regions for maintaining overall structural integrity. In CFRP composite joints, the connection is often epoxy bonded as opposed to bolted to prevent the introduction of stress concentrations.

Damage, that can occur in adhesive bonded joints and in skin to stringer bonding, includes disbonds, porosity, poor bond adhesion and reduced cohesive strength of the adhesive. Disbonds have a more likelihood of occurring during service while porosity, poor adhesion, and reduced cohesive strength are, generally, a consequence of the manufacturing process. Disbonding due to overloading conditions is likely to result in a kissing bond scenario. For this disbond type, the surfaces are touching. Therefore, shear stress transfer is greatly reduced across the bond-line while normal stress continuity is maintained. The existence of disbonds in the wing skin-to-spar joint diminishes the torsional rigidity of the aircraft's wing, compromising both performance and safety. In skin to stringer bonding, wrinkling is also a problem very relevant. Damage detection in CFRP composites presents more difficulty than metallic structures due to its mechanical anisotropy and heterogeneous composition. Damage, generally, occurs beneath the material surface and the brittle nature of high strength CFRP composites can lead to sudden failure mechanisms. Current NDE methods are often unreliable or impractical for inspection of large scale composite structures. Therefore, an SHM philosophy for damage identification is particularly well suited for aircraft comprised mainly of CFRP components.

1.3. GLOBAL VERSUS LOCAL SHM APPROACHES

The objective of a Structural Health Monitoring (SHM) system is to identify anomalies or damages such as cracks, delaminations and disbonds in structures. In this work in particular, attention is placed upon defects like delaminations and wrinkling. SHM diagnostic methods can be generally classified as either global or local. Global approaches are based upon relatively low frequency vibration measurements of the structure. Data acquisition can be done passively by relying upon the natural operational vibrations for source excitation or actively by forced vibration of the structure (as in this work). The structural response is measured at discrete locations in terms of acceleration through the use of accelerometers or strain by employing conventional foil gages, piezoelectric transducers, fiber Bragg gratings in some instances or velocity through the use of Laser Scanning Doppler Vibrometer, as in our case. Dynamics-based inspection techniques are typically classified as vibration-based methods (global methods) and wave-propagation methods (local methods). Vibration-based damage detection techniques, typically, monitor changes in measured flexibility coefficients, while wave propagation inspections look for reflections and mode conversion phenomena caused by the presence of damage.

All global methods consider low frequency excitation, generally less than 50 kHz. As a result, they are inherently only sensitive to fairly large levels of damage. To detect smaller levels of damage, local SHM diagnostic methods can be utilized. These methods consider high frequency excitations; typically, within the range of 10 kHz to 500 kHz. Consequently, local SHM methods are capable of measuring more localized response within the structure at the expense of requiring a more densely arranged sensing system. In this work, the detailed spatial information required is provided by the Scanning Laser Doppler Vibrometer (SLDV). A wide range of local damage identification methods exist. For active diagnostics, excitation of the system occurs through the use of an actuating source such as piezoelectric device. Conversely, passive diagnostics rely on excitation sources occurring from the quasi-static loading conditions or damage itself, i.e. impact or acoustic emission. Both methods of local system

diagnostics have associated advantages and disadvantages. The most common active techniques are based upon the measurement of the electro-mechanical impedance or the use of ultrasonic guided waves. With few exceptions, active methods require the measurement and storage of a vast amount of baseline information and, often, require a fairly dense array of transducers. However, active methods control the excitation characteristics within the system. Therefore, they possess the capability to customize the excitation in order to achieve greater sensitivity to specific defect types.

Local passive methods for damage identification can alleviate complications associated with the requirement of dense sensor arrays, large storage of baseline feature measurements, complex signal processing and statistical pattern process algorithms. The most common passive approaches use piezoelectric transducers to monitor impacts or acoustic emissions generated from internal material damage. These methods, thereby, rely on measurement of propagating waves within the structure. In this scenario, damage detection is straight forward. Measurements above a specified threshold are assumed to correspond to the onset of damage. Damage localization can be evaluated through the use of simple triangulation algorithms. Otherwise, higher levels of damage identification can be achieved by incorporating neural networks or dynamic models. A disadvantage of passive approaches is the requirement of continuous system monitoring, since it is generally not known when damage may occur. In addition, each of the passive methods discussed show difficulty in accurate damage identification for large scale complex structures.

1.4. VIBRATION-BASED VS GUIDED WAVES-BASED TECHNIQUES: OUR CHOICE

Many structural health monitoring techniques developed over the years are based on the detection of changes in the dynamic behaviour of the monitored components. Valuable review of the state-of-the-art in dynamics-based structural health monitoring can be found in [8, 9, 10]. Early studies evaluated the influence on the natural frequencies of localized stiffness reduction caused by

damage. These investigations have generally proven that natural frequencies are damage indicators which generally show low sensitivity and they do not allow the determination of the location of damage. More recent studies have investigated the effect of localized and distributed damage on mode shapes, operational deflection shapes (ODS) and corresponding curvatures. The detection of small changes in the deformed configuration of the structure can be used to localize damage and, potentially, estimate its severity. The existing techniques vary on the basis of the type of dynamic response signals used for the analysis and on the features or parameters considered as damage indicators. Such features or parameters must obviously be sensitive to damage and must vary monotonically with the extent of damage.

In particular, small variations from an undamaged state can be highlighted by successive spatial differentiations of the deflections, as typically required for estimating curvature modes and associated strain energy. These modal-based methods are very attractive as they provide information regarding the general state of health of the structure. However, they tend to have limited sensitivity and, generally, they are not accurate enough to provide detailed information regarding damage type and extent.

The lack in sensitivity and capability of discriminating damage from changes in the operating conditions of modal-based methods can be overcome by applying inspection techniques based on Guided Ultrasonic Waves (GUWs) propagation [5, 6, 7]. Guided waves, such as Lamb waves, show sensitivity to a variety of damage types and, as opposed to bulk waves used in traditional ultrasonic techniques, have the ability to travel relatively long distances within the structure under investigation. For this reason, GUWs are particularly suitable for SHM applications, which may employ a built-in sensor/actuator network to interrogate and assess the state of health of the structure. In most applications, GUWs are generated and received by piezoelectric transducers which can both excite the structure and record its response. In our case, the sensing device is the SLDV. The fundamentals of this type of operation consist in evaluating the characteristics of the propagation along the wave path between each transducer/receiver pair and detecting reflections associated with damage. The interpretation of the signals characteristics and the detection of reflections are,

however, complicated by the multi-modal and dispersive nature of GUW signals. For this reason, advanced signal processing techniques are being employed to highlight signal features which are sensitive to the presence of damage, which can be used for its classification and for the estimation of its extent. This work presents an attempt to integrate modal-based and guided waves inspections, in order to overcome the drawbacks of the two techniques, while combining their advantages. Most of the damage measurements assume the possibility of comparing current measurements with baseline information regarding the undamaged state of the structure. This is a significant drawback, as it assumes the availability of data on the component under test in its pristine state and the basic assumption that any measured change is due to damage only and not to environmental or boundary conditions changings applied to the component. The techniques presented below are examples of solutions proposed over the years, whose practicality can be significantly improved, if coupled with procedures aimed at generating data approximating the undamaged response of the structure. An example of such procedure, proposed in [8] and implemented through this work, is presented in the next chapter.

1.5. VIBRATION-BASED DAMAGE MEASURES

1.5.1. FREQUENCY CHANGES

Modal parameters are global properties of a vibrating structure, so their change can indicate the presence of damage without performing direct measurements at or near the damage site. One of the typical effects of damage is a localized reduction of stiffness, which produces a corresponding change in modal frequencies. Analytical quantification of the change in modal frequencies related to loss of stiffness in simple beam and plate structures can be found in [9, 10, 11] where perturbation methods are applied to estimate modal properties in the presence of notch-type defects. It is nowadays quite accepted that simple monitoring of frequency changes is not a reliable and sensitive enough method for early damage detection and cannot easily provide location information. Noteworthy attempts include the work of Cawley and Adams [12] who investigated frequency shifts due to damage in composite materials. The ratio

between shifts at various modes $\Delta\omega_i / \Delta\omega_j$ is used to construct an error term which allows estimating the damage location. This technique, which does not account for multiple damage sites, was revised in [13, 30] using the sensitivity of modal frequency changes in terms of local stiffness and mass changes. The following error function for the i-th mode and p-th structural member was introduced:

$$e_{ip} = \frac{z_i}{\sum_j z_j} - \frac{F_{ip}}{\sum_j F_{jp}} \qquad (1.1)$$

where z_i is the i-th term in the array of squared modal frequency changes, which is defined as:

$$\{z\} = [F]\{a\} - [G]\{\beta\} \qquad (1.2)$$

where $[F]$ and $[G]$, respectively denoting the changes in elemental stiffness and mass magnitudes. The member that minimizes the error in eq. (1.1) is determined to be the damaged one, again under the assumption of single defect. The estimation of the frequency change sensitivity is obviously based on the Finite Element (FE) model of the structure under consideration, which may be problematic in the case of complex structures. Hearn and Testa [14] employed the FE formulation to introduce a damage severity parameter for structural member n representing the element's stiffness loss, i.e.:

$$[\Delta k_n] = \alpha_n [k_n] \qquad (1.3)$$

which, under the assumption of single damage location, can be directly related to a frequency shift according to the following expression:

$$\Delta\omega_i^2 = \alpha_n \frac{\{\varepsilon_n(\phi_i)\}^T [k_n] \{\varepsilon_n(\phi_i)\}}{\{\phi_i\}^T [M] \{\phi_i\}} \qquad (1.4)$$

where $\{\varepsilon_n(\phi_i)\}$ are the n-th member's deformations computed on the basis of the undamaged mode shapes ϕ_i, while $[M]$ and $[k_n]$ describe the mass of the structure and the stiffness of the n-th member. This equation directly relates the effect of damage on a specific component n to the corresponding shift in frequency, under the assumption that the evaluation of this direct relation can be performed on the basis of pre-damage modal information. The hypothesis that damage only produces a change in stiffness $[\delta K]$ is exploited in Richardson and Mannan [15], where the orthogonality properties of the damaged and undamaged structure is used to obtain the following sensitivity equation:

$$\{\phi_i\}^T [\delta K] \{\phi_i\} = \left(\omega_i^{(d)}\right)^2 - \left(\omega_i^{(u)}\right)^2 \qquad (1.5)$$

where it is again assumed that damage causes a negligible change in the mode shapes.

1.5.2. MODE SHAPE CHANGES

Mode shape changes are found to be quite sensitive to damage, especially when higher modes are considered and are able to directly provide damage location information. The problem associated with mode shape monitoring is clearly related to the need of sufficient spatial measurement resolution, which complicates the experimental procedure. The required measurement resolution can be easily achieved through the use of a Scanning Laser Doppler Vibrometer, which has become an important tool for dynamic testing. Alternatively, the number of measurement locations can be reduced if the FE model of the structure under investigation is available for its use in increasing the information on the structure's behaviour and for interpolation purposes. Most of the early work, on mode shape analysis, considers the Modal Assurance Criterion (MAC) to compare measured or damaged modes with undamaged or numerical ones. For example, West [16] used the MAC to correlate the modes of an undamaged

Space Shuttle Orbiter body flap with those after the flap has been exposed to acoustic loading. Another technique presented in [17], considered a damage measure based on change in the mode shape and mode shape slope. Change were simulated for stiffness reductions in each structural member and compared to measured changes to determine the damage location.

Other techniques of various natures exploit comparisons through different types of modal correlation criteria. For example, Fox [18] proposed the concept of a MAC based on measurement points close to a node point for a particular mode ("Node line MAC"), Kim et al. [19] investigated the use of the Partial MAC (PMAC) to compare the MAC values of coordinate subsets of the modal vectors and Ko et al. [20] presented a method that uses a combination of MAC, COMAC and sensitivity analysis to detect damage in steel framed structures. Finally, a damage signature based on the mode shape normalized by the change in the modal frequency of another mode is proposed in [20], as a way to combine frequency shift and changes in mode shape as damage indicators.

More recent investigations apply the Wavelet Transform (WT) as a signal processing tool to highlight the presence of discontinuities in the modal deflections. The spatial information resulting from multi-point measurements are fed to wavelet algorithms to obtain information regarding anomalies related to damage in the deformed shapes. Plots obtained upon the wavelet analysis localize the damage and may be used, after proper calibration, to quantify the damage extent [21, 22, 23].

1.5.3. MODE SHAPE CURVATURE CHANGES

An alternative to using mode shapes to obtain spatial information about structural changes in using mode shape derivatives, such as curvature or strain energy distributions obtained from spatial integration of curvature modes. For example, in 1991 Pandey, Biswas and Samman [24] demonstrated the use of absolute changes in curvature as good indicators of damage for a beam-type structure. They used a central difference-based numerical differentiation technique to compute the curvature from numerically obtained mode shapes. Their results showed that absolute changes in curvature were localized around

the damaged region and that damage could be quantified by establishing a relationship between changes in curvature and damage extent. The evaluation of changes in the curvature of dynamic deflection shapes as a tool for damage detection and localization were also investigated in [10] and subsequently in [11]. In these studies, the dynamic behavior of beams with notch defects and delaminations was studied analytically and experimentally. Analytical models described the dynamic behavior and the curvature modes of cracked beams through perturbation of the modal parameters of the undamaged beams, so that approximated analytical expressions for the damaged modes were obtained. The analytical studies were supported by experimental investigations performed on simple beam structures. Their results show the potentials of the technique when applied to the first mode of the beam.

The limitation to a single mode was mainly dictated by the limited spatial resolution available in the accelerometers-based experiments. Ho and Ewins [24] formulated a damage index defined as the quotient squared of the corresponding modal curvatures of the undamaged and damaged structure. The damage index was found to be highly susceptible to noise, as measurement errors were amplified due to second derivative computations based on numerical techniques. They also demonstrated that spatially sparse measurements adversely affect the performance of the damage index. As an alternative Ho and Ewins [25] investigated the changes in the square of the slope of mode shapes of beams. Oscillations in the slope computations were reduced through polynomial fit of the measured mode shape as compared to the use of finite difference approximation. They also reported that higher derivatives can be more sensitive to damage, but are more subject to numerical errors. The same technique has then been extended to plate structures, where accelerometers are used to measure the detections to be interpolated for successive differentiation. The results presented in [30, 27], show the effectiveness of the technique, and are used as a basis for the developments presented in the present study.

1.6. GUIDED WAVES-BASED DAMAGE MEASURES

Guided waves are one of the most encouraging tools for SHM applications. In plates these waves can propagate for large distances, they are sensible even to small defects and they involve the whole material thickness, meaning that a defect can be identified also if it is in the middle of the plate. One distinction that can be done lies in the selection of the mode used for the investigation. The chosen mode should be able to offer a very low dispersion, low attenuation with the distance, high sensitivity to damages, easy excitability and good detectability. Some authors [30] consider the S_0 mode as the proper one, for its low dispersion, low attenuation in amplitude and its velocity of propagation. Other authors [31, 32] prefer the A_0 mode, because, even if it is more dispersive for low frequencies, it has lower wavelength than the S_0 mode, thus it can detect smaller defects.

Guided waves result from the constructive interference of bulk longitudinal and shear waves propagating within a confined geometry such as a railhead, wing skin, or pipeline. An illustration of the guided wave phenomenon, thought of as the superposition of bulk longitudinal and shear waves, is shown in figure 1.2. To satisfy the boundary conditions at each interface, mode conversion into to both longitudinal and shear waves occurs due to an incoming bulk wave. With enough propagation distance, the large number of mode converted bulk waves result in bulk wave resonances, otherwise known as guided waves.

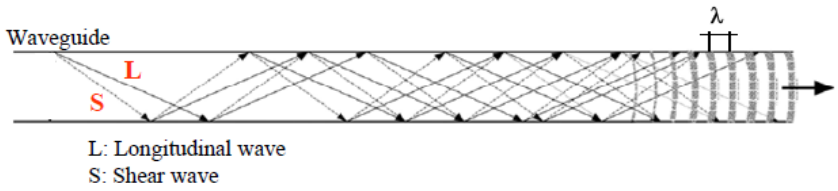

Fig. 1.2 - Guided waves propagating within a confined geometry.

Most structural elements of aerospace vehicles are natural waveguides, thereby lending themselves to ultrasonic guided wave based SHM methods. The guided wave method can be an effective diagnostic tool due to its capability of long-range inspection as well as its flexibility in selecting sensitive mode-frequency combinations. In addition, through the use of built-in actuators and sensors, the guided wave approach is complementary to the development of integrated systems for continuous on-line diagnostics as opposed to regularly scheduled NDE maintenance. The difficulties associated with the use of guided waves for SHM include their dispersive nature (wave velocity is frequency dependant) and the existence of multiple modes propagating simultaneously.

The objective is the extraction of relevant features from the recorded response, which may be related to damage. In the following chapter, the innovative filtering techniques, introduced by Ruzzene, followed in this work and applied to complex components for the first time, are presented. Since the argument of waves is widely discussed in this work, it is necessary to present an introduction to wave theory, dealing with the main aspects that will be treated. This introduction is presented in the following.

1.7. THEORY OF WAVES IN ELASTIC MEDIA

In this section a brief description of the main aspects of the wave theory in solid media is presented. The approach adopted by the authors of two reference books [33, 34] is followed. Waves in a taut string are first investigated, because they require a simple mathematical approach and because nearly all the basic concepts of propagation, such as dispersion and group velocity, are introduced. Then the waves in plate, such as the Lamb waves, will be investigated.

1.7.1. WAVES IN TAUT STRING

The governing equation for a taut string is now developed. Since boundaries introduce complications, an infinite length string is considered. The differential string element under tension F of Fig 1.3 is considered. It is assumed that any variation in tension, due to string displacement, is negligible.

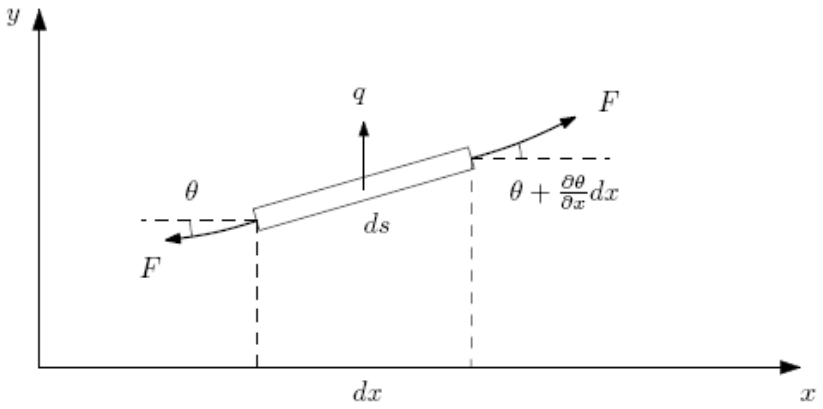

Fig. 1.3 - Differential element of taut string.

The mass density per unit length is ρ and the external loading is $q(x,t)$. The equation of motion in the vertical direction y is Eq.1.6.

$$-F\sin\theta + F\sin\left(\theta + \frac{\partial\theta}{\partial x}\partial x\right) + qds = \rho ds\frac{\partial^2 y}{\partial t^2} \qquad (1.6)$$

The arc length ds is given by $\sqrt{1+y'^2}\,dx$. If small deflection are assumed $ds \approx dx$, $\sin\theta \approx \theta$ and $\theta \approx \partial y/\partial x$, the preceding equation becomes Eq. 1.7

$$F\frac{\partial^2 y}{\partial x^2} + q = \rho\frac{\partial^2 y}{\partial t^2} \qquad (1.7)$$

Of particular interest is the form of the homogeneous equation obtained by setting q = 0, giving Eq 1.8

$$\frac{\partial^2 y}{\partial x^2} = \frac{1}{c_0^2}\frac{\partial^2 y}{\partial t^2} \qquad c_0 = \sqrt{\frac{F}{\rho}} \qquad (1.8)$$

This equation is known as the wave equation and the term c_0 denotes the velocity of wave propagation.

Now, using the separation of variable approach, the propagation of a simple harmonic wave is investigated. The term $y = Y(x)T(t)$ is substituted in Eq.1.8 giving Eq.1.9.

$$\frac{Y''}{Y} = \frac{T''}{c_0^2 T} = -k^2 \qquad (1.9)$$

The resulting solution for $y(x,t)$ is expressed in Eq.1.10

$$y = \left(A_1 \sin kx + A_2 \cos kx\right)\left(A_3 \sin \omega t + A_4 \cos \omega t\right) \qquad (1.10)$$

where the radial frequency is given as $\omega = kc_0$. Regrouping and multiplying Eq.1.11 is obtained.

$$y = A_1 A_4 \sin kx \cos \omega t + A_2 A_3 \cos kx \sin \omega t + A_2 A_4 \cos kx \cos \omega t + A_1 A_3 \sin kx \cos \omega t \qquad (1.11)$$

Using trigonometric identities, as $\sin(\alpha + \beta) = \sin\alpha \cos\beta + \cos\alpha \sin\beta$, the solution can be put in the form of Eq.1.12.

$$y = B_1 \sin(kx + \omega t) + B_2 \sin(kx - \omega t) + B_3 \cos(kx + \omega t) + B_4 \cos(kx - \omega t) \qquad (1.12)$$

Any of the four terms of this equation, as the one in Eq.1.13, can show the wave propagation in the direction of positive x.

$$y = A\cos(kx - \omega t) = A\cos k(x - c_0 t) \qquad (1.13)$$

Considering the argument of Eq.1.13 as the phase, which is defined in Eq.1.14, the wave can be visualized as in Fig.1.4.

$$\phi = kx - \omega t = k(x - c_0 t) \qquad (1.14)$$

It can be noted that for increasing time, increasing values of x are required to maintain the phase constant. The shape of the deflections at successive instants of time should be represented as in Fig.1.4. The propagation velocity of the constant phase is c0 and it is defined as phase velocity. Constancy of phase for increasing time requires $x = c_0 t$. Referring to Fig.1.4, the distance between two successive points of constant phase is called wavelength and indicated by the symbol λ. The wavelength is related to the parameter k by Eq.1.15.

$$k = \frac{2\pi}{\lambda} \qquad (1.15)$$

The parameter k is called wavenumber. It is inversely proportional to the wavelength and it represents the number of waves in the unit length. Having considered the characteristics of a typical harmonic wave, it is seen that the remaining terms of Eq.1.12 are similar in nature. The major point of difference is that terms having the argument $(kx + \omega t)$ are propagating in the negative x direction.

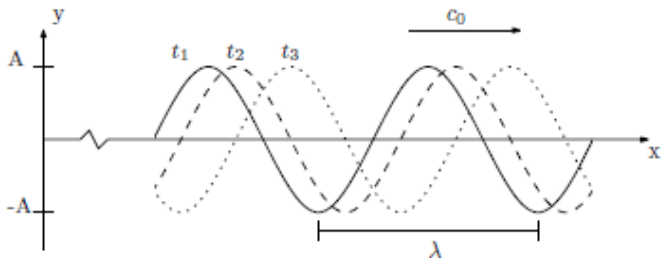

Fig. 1.4 - Deflections of an infinite long string at successive times

Another solution to the wave equation is given by D'Alembert and it is reported in Eq.1.16.

$$y(x,t) = f(x - c_0 t) + g(x + c_0 t) \qquad (1.16)$$

This equation satisfies Eq.1.8 for any arbitrary function f and g, as long as the initial and boundary conditions can eventually be satisfied. The functions f and g represent propagating disturbance. Whatever the initial shape of the disturbances, that shape is maintained during the propagation, so the waves propagate without distortion, as represented in Fig.1.5. The undistorted nature of wave propagation represents a fundamental characteristic of the one-dimensional wave equation.

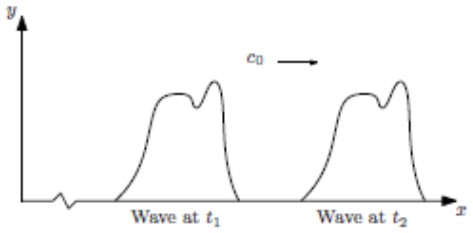

Fig. 1.5 - Undistorted propagation of wave envelope

1.7.2. STRING ON AN ELASTIC BASE – DISPERSION

The wave equation Eq.1.8 considered up to this point is simple. Moreover, in the system described by this equation, the pulses propagate without distortions. Now, a more complicated situation, in which the string rests on an elastic foundation, is considered. This situation is represented in Fig.1.6.

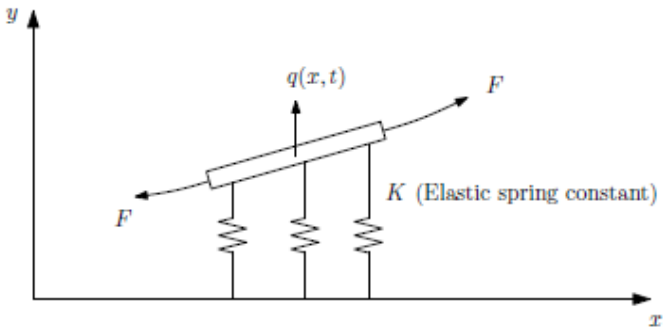

Fig. 1.6 - Differential element of a string on an elastic base

The external load may be interpreted as due to the elastic foundation, as expressed by Eq.1.17

$$q(x,t) = -Ky(x,t) \qquad (1.17)$$

where K is the elastic modulus of the foundation. The resulting governing equation, in the absence of other external forces, is given by Eq.1.18.

$$\frac{\partial^2 y}{\partial x^2} - \frac{K}{F} y = \frac{1}{c_0^2}\frac{\partial^2 y}{\partial t^2} \qquad c_0 = \sqrt{\frac{F}{\rho}} \qquad (1.18)$$

This equation is no longer of simple wave equation form. Thus, a solution of the form $f(x \pm c_0 t)$ may not satisfy it. Since the major characteristic of such a solution is undistorted wave pulse propagation, it is now logical to expect a distortion. This phenomenon is known as dispersion. Now, the necessary conditions for the propagation of harmonic waves are determined. Assuming the solution Eq.1.19

$$y(x,t) = Ae^{i(kx-\omega t)} \qquad (1.19)$$

and substituting it in Eq.1.18, it gives the expression Eq.1.20, which is called characteristic equation or dispersion equation.

$$\left(-k^2-\frac{K}{F}+\frac{\omega^2}{c_0^2}\right)e^{i(kx-\omega t)}=0 \qquad (1.20)$$

This equation must fulfill Eq.1.21 in order to admit non-trivial solutions

$$\omega^2=c_0^2\left(k^2+\frac{K}{F}\right) \qquad \omega=\omega(k) \qquad (1.21)$$

or, alternatively, Eq.1.22.

$$k^2=\frac{\omega^2}{c_0^2}-\frac{K}{F} \qquad k=k(\omega) \qquad (1.22)$$

Here the phase velocity, c_p, is different from the c_0 of the taut string. Indeed, substituting $\omega=kc_p$ in Eq.1.21 or Eq.1.22, the result of Eq.1.23 is obtained.

$$c_p^2=c_0^2\left(1+\frac{K}{Fk^2}\right) \qquad c_p=c_p(k) \qquad (1.23)$$

Alternatively, one can obtain the results in Eq.1.24.

$$k^2=\frac{K/F}{\left(c_p^2/c_0^2\right)-1} \qquad k=k(c_p) \qquad (1.24)$$

Another set of relations can be obtained by eliminating k from Eq.1.22 or ω from Eq.1.24, to give Eq.1.25

$$\omega^2=\frac{K/Fc_p^2}{\left(c_p^2/c_0^2\right)-1} \qquad \omega=\omega(c_p) \qquad (1.25)$$

and Eq. 1.26

$$k^2 = \frac{\omega^2 c_0^2}{\omega^2 - \left(k\, c_0^2 / F\right)} \qquad k = k(\omega) \qquad (1.26)$$

The results show that a harmonic wave of frequency ω can propagate only at a specific velocity, c_p, as it is indicated by the relation $\omega = \omega(c_p)$. Considering a pulse shape at a given time $t = t_0$ as a Fourier superposition of harmonic waves, as the time advance, each Fourier component of the original pulse will propagate with its own individual velocity. The various components will become increasingly out-of-phase relative to their original position, so that the original pulse shape will became increasingly distorted, as shown in Fig.1.7. In the taut string, where K=0, this phenomenon is not present. Another important result comes from the analysis of the roots of Eq.1.22,

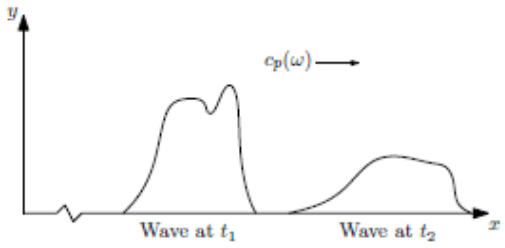

Fig. 1.7 - Distorted propagation of a wave envelope

which are reported in Eq.1.27.

$$k = \pm\sqrt{\frac{\omega^2}{c_0^2} - \frac{K}{F}} \qquad (1.27)$$

The roots are real if $\omega^2 / c_0^2 > K/F$, thus the propagation is possible to the right or left, depending on which sign is selected, as expressed by Eq.1.28.

$$y = Ae^{-i(\pm kx + \omega t)} \qquad (1.28)$$

On the other hand, if $\omega^2/c_0^2 < K/F$, then the wavenumber k is imaginary. Defining $\bar{k}^2 = -k^2$, the motion of the string is given by Eq.1.29.

$$y = Ae^{\pm\bar{k}x}e^{-i\omega t} \qquad (1.29)$$

This corresponds to a spatially varying, but non-propagating disturbance. Since the interest is on the conditions under which a harmonic wave can exist, the results for imaginary wavenumbers are not considered in the study of propagating waves, since they are non-propagating. Finally, the case $\omega^2/c_0^2 = K/F$ represents the transition from propagation to non-propagation. Defining $\omega_c = c_0\sqrt{K/F}$, the string motion is the one reported in Eq.1.30.

$$y = Ae^{-i\omega_c t} \qquad (1.30)$$

The frequency ω_c is called cut-off frequency of the propagating mode. There is no spatial variation in the motion, so the string is vibrating as a simple spring-mass system. The basic factors governing propagation in a string on an elastic foundation have been presented. Now, these results are displayed in graphical form. Typically, two types of displays are used: the plot of frequency versus wavenumber, which is called frequency spectrum of the system and the plot of phase velocity versus wavenumber, which is called dispersion curve of the system. To plot the frequency spectrum, the Eq.1.27 should be considered. Assuming the frequency as real and positive, it is possible to get both real and imaginary wavenumbers, if $\omega < \omega_c$ and $\omega > \omega_c$, respectively. The results are shown in Fig.1.8. The curves on the real plane are hyperbolas, while the imaginary curves are ellipses. The line $K = 0$ is the non-dispersive result for the taut string. It is possible to extract the phase velocity from the frequency spectrum by the relation $\omega = c_p k$.

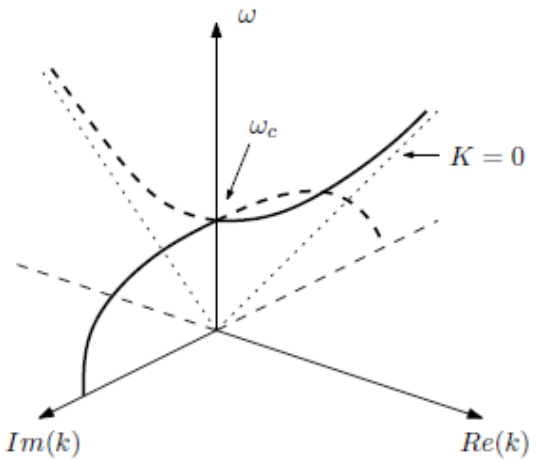

Fig. 1.8 - Frequency spectrum for a string on an elastic foundation

Graphically, taking a point on the real curve of the spectrum, the slope of the chord between the point and the origin is the phase velocity $c_p = \omega/k$. This relation is shown in Fig.1.9. In this figure an alternative way to represent the frequency spectrum is also shown.

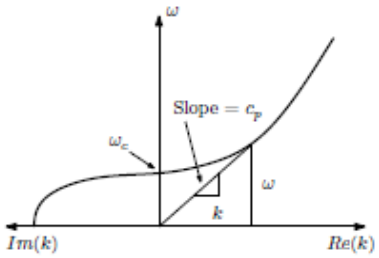

Fig. 1.9 - Two-dimensional representation of the frequency spectrum showing relation between chord slope and phase velocity

Since the spectrum is usually symmetric with respect the $\mathrm{Re}(k)=0$ and the $\mathrm{Im}(k)=0$ planes, it is sufficient to present a two-dimensional plot of the ω on

the $\mathrm{Re}(k)>0$ and $\mathrm{Im}(k)>0$ axes. Phase velocity is often presented independently by dispersion curves. Although it is possible to consider c_p as positive, negative, real and imaginary, depending on k, the most physical meaningful information is contained in a plot which has as axes $\mathrm{Re}(c_p)>0$ and $\mathrm{Re}(k)>0$, as shown in Fig.1.10. The horizontal line is the result of the non-dispersive string, where all the wavelengths propagate at the same velocities c_0. Usually, in structural health monitoring applications the dispersion curves present the phase velocity as function of frequency ω.

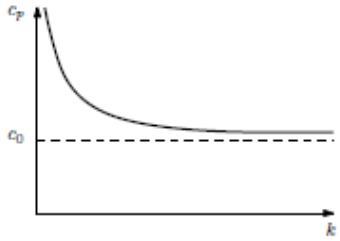

Fig. 1.10 - Dispersion curve for a string on an elastic foundation

1.7.1. GROUP VELOCITY

Group velocity is associated with the propagation velocity of a group of waves of similar frequency. In reference books this concept is always introduced by means of the pool example. A stone dropped in a pool of still water creates an intense local disturbance which does not remain localized, but spreads outward over the pool as a train of ripples. In this phenomenon, it can be observed that, when a group of waves advance into still water, the velocity of the group is less than the velocity of individual waves of which it is composed. The waves appear to originate at the rear of the group, propagate to the front and disappear. A simple analytical explanation is to consider two propagating harmonic waves of equal amplitude, but slightly different frequency, ω_1 and ω_2. Such harmonic waves will have the expression of Eq.1.31,

$$y = A\cos(k_1 x - \omega_1 t) + A\cos(k_2 x - \omega_2 t) \qquad (1.31)$$

where $\omega_1 = k_1 c_{p1}$ and $\omega_2 = k_2 c_{p2}$. Using trigonometric identities, this expression can be written as Eq.1.32.

$$y = 2A\cos\left[\frac{1}{2}(k_2 - k_1)x - \frac{1}{2}(\omega_2 - \omega_1)t\right]\cos\left[\frac{1}{2}(k_1 + k_2)x - (\omega_1 + \omega_2)t\right] \tag{1.32}$$

Since the frequencies are only slightly different, the wavenumber $k = \omega/c_p$ also will slightly differ, as expressed in Eq.1.33.

$$\omega_2 - \omega_1 = \Delta\omega \qquad k_2 - k_1 = \Delta k \tag{1.33}$$

Similarly, the average frequency, wavenumber and velocity are defined in Eq.1.34.

$$\omega = \frac{1}{2}(\omega_1 + \omega_2) \qquad k = \frac{1}{2}(k_1 + k_2) \qquad c_p = \frac{\omega}{k} \tag{1.34}$$

Thus, Eq.1.32 can be written as Eq.1.35.

$$y = 2A\cos\left[\frac{1}{2}\Delta k x - \frac{1}{2}\Delta\omega t\right]\cdot\cos[kx - \omega t] \tag{1.35}$$

In this equation the cosine term, containing the difference terms Δk and $\Delta\omega$, is a low-frequency term, since $\Delta\omega$ is a small number. The propagation velocity of the low-frequency term is expressed in Eq.1.36,

$$c_g = \frac{\Delta\omega}{\Delta k} \tag{1.36}$$

which in the limit becomes Eq.1.37.

$$c_g = \frac{\partial\omega}{\partial k} \tag{1.37}$$

This velocity is called group velocity. On the other hand, the cosine term containing the average wavenumber k and frequency ω will be a high-frequency term, propagating at the average velocity c_p. The low-frequency term acts as a modulation on the high-frequency carrier as shown in Fig.1.11. The individual harmonics travel with different phase velocities c_p, but the superimposed packet travels with the group velocity c_g. The velocity of the high-frequency carrier may actually be greater than, equal to, or less than the velocity c_g. The actual relation will depend on the dispersion characteristics of the elastic system. Graphically the various cases can be represented considering Eq.1.37, which states that the group velocity is equal to the local slope of the frequency spectrum curve, as shown in Fig.1.12. Recalling that the slope of a chord to a point is the phase velocity, if that slope is higher than the local slope of the curve $(\theta_p > \theta_g)$, then $c_g < c_p$, otherwise if the slope of the chord to a point is lower than the local slope of the curve $(\theta_p < \theta_g)$, then $c_g > c_p$.

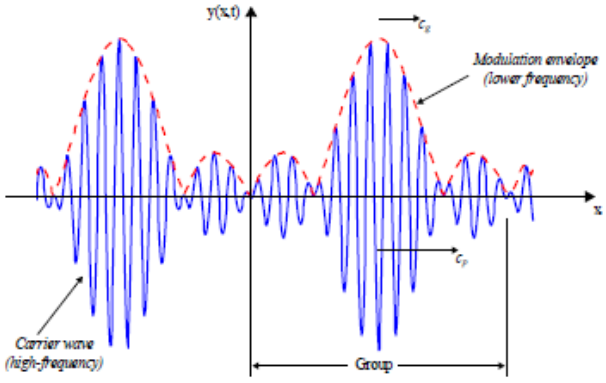

Fig. 1.11 - Group velocity example

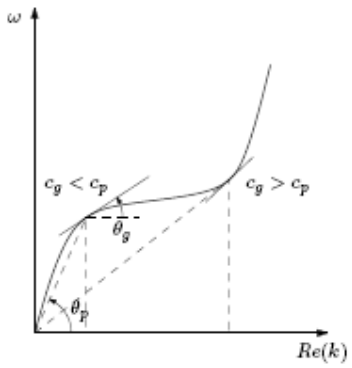

Fig. 1.12 - Group velocity variation with phase velocity

1.7.1. WAVE IN PLATES - LAMB WAVES

Now a more practical aspect of the wave propagation is presented. First, it is necessary to distinguish between bulk waves and guided waves. They are both governed by the same set of partial differential wave equations (reported in [33, 34]), but they differ in the boundary conditions. Bulk waves travel in the bulk of the material, hence away from the boundaries, for this reason mathematically there are no boundary conditions that need to be satisfied by the proposed solution. In contrast, the solution to a guided wave problem must satisfy the governing equation as well as some physical boundary conditions. The introduction of boundary conditions makes the guided waves problem difficult to solve analytically. However, some special cases of guided waves problems have been solved and these solutions take the names of the investigator. The Rayleigh waves are free waves on the surface of a semi-infinite solid. Stonely waves are free waves that occur at an interface between two media. Lamb waves are waves of plain strain that occur in a free plate. Another difference between bulk waves and guided waves is that bulk waves have just two mode of propagation that are the longitudinal mode and the transverse mode, whereas the guided waves have an infinite number of modes. Longitudinal waves, also called volumetric wave, imply no rotations of medium particles, whereas transverse waves, also called rotational waves, do not imply volume change in material. These waves propagate in infinite media at two different speeds, which are

c_L for the longitudinal mode and c_T for the transverse mode. The expressions of these velocities are reported in Eq.1.38

$$c_L = \sqrt{\frac{E(1-\nu)}{\rho(1+\nu)(1-2\nu)}} \qquad (1.38a)$$

$$c_T = \sqrt{\frac{E}{2\rho(1+\nu)}} \qquad (1.38b)$$

where E is the Young's modulus, ν is the Poisson's ratio and ρ is the density of the material. A graphical representation of the particle motion for the longitudinal and transverse mode is shown in Fig.1.13. The interactions of these two basic modes with the boundaries generate reflections, refractions and mode conversions [33, 34]. The superpositions of all these waves cause the formation of guided wave modes in the plate, which are infinite. The interest in the present work is focused on stringerized plates. Thus, guided waves in plates are now analyzed: these waves are also known as Lamb waves.

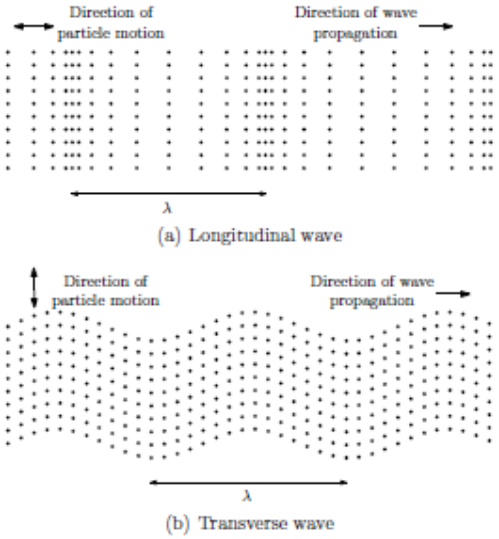

Fig. 1.13 - Directions of particle motion for the case of harmonic waves in infinite media

Lamb waves, like other elastic waves, can be described in a form of Cartesian tensor notation, as expressed in Eq.1.39

$$\mu u_{i/jj} + (\lambda + \mu) u_{j/ji} + \rho f_i = \rho \ddot{u}_i \qquad (1.39)$$

where i, j = 1, 2, 3, where u_i and f_i are the deformation and the body force in the i direction, respectively. These equations of motions, which contain only the particle displacements, are the governing partial differential equations for displacement. They are defined through the use of Lame constants, λ and μ, which can be expressed in terms of Young's modulus and Poisson's ratio through the relations reported in Eq.1.40.

$$E = \frac{\mu(3\lambda + 2\mu)}{\lambda + \mu} \qquad (1.40a)$$

$$\nu = \frac{\lambda}{2(\lambda + \mu)} \qquad (1.40b)$$

To well-define the problem of Lamb waves in plates, boundary conditions must be applied at both free surfaces of the plate. On these surfaces the traction must vanish. Moreover, the assumption of plain stress must be done. Under these conditions, it is possible to find a solution to Eq.1.39, which describes Lamb waves in a homogeneous plate. To solve this problem, the method of the displacements potentials can be used [35]. The solution can be split into two parts with symmetric and anti-symmetric properties. Each part leads to a different Lamb wave mode, one symmetric and one anti-symmetric, as expressed in Eq.1.41,

$$\frac{\tan(qh)}{\tan(ph)} = -\frac{4k^2 qp}{\left(k^2 - q^2\right)^2} \qquad (1.41a)$$

$$\frac{\tan(qh)}{\tan(ph)} = -\frac{\left(k^2 - q^2\right)^2}{4k^2 qp} \qquad (1.41b)$$

where p and q are defined in Eq.1.42,

$$p^2 = \frac{\omega^2}{c_L^2} - k^2 \qquad (1.42a)$$

$$q^2 = \frac{\omega^2}{c_T^2} - k^2 \qquad (1.42b)$$

and h, k and ω are the half-thickness of the plate, wavenumber and frequency respectively. The graphical representation of the symmetric and the anti-symmetric modes is shown in Fig.1.14, the arrows represent the displacements of the material. Equations Eq.1.41 can be solved analytically just

for very simple cases. At a given frequency, there are an infinite number of wavenumbers, either real or purely imaginary, that can solve Eq.1.41.

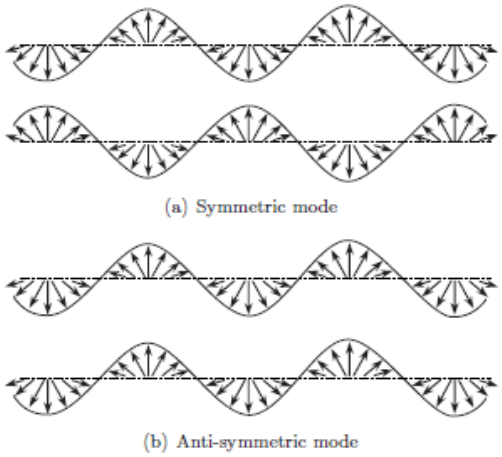

Fig. 1.14 - Symmetric and anti-symmetric Lamb wave modes

To each wavenumber corresponds a wave mode, but just the modes deriving from real wavenumber are considered. Hereinafter the symbols S_i and A_i are used to define the symmetric and the anti-symmetric modes, respectively, with the subscript indicating the order of the mode. Equations in Eq.1.41 also indicate that the Lamb waves, regardless of mode, are dispersive, because velocity is dependent on frequency. For this reason dispersion curves can be plotted. This curves represent how the phase velocity used to define the symmetric and the anti-symmetric modes, respectively, $c_p = \omega / k$ or the group velocity, vary with the frequency. An example of dispersion curves plotting the phase velocity, as function of the frequency-thickness product, for an aluminum plate is shown in Fig.1.15. In this figure are reported both the symmetric and the anti-symmetric Lamb waves modes up to the second order.

It can be noticed that ,for lower frequencies, just two Lamb waves mode are present. This means that the other modes, for those frequencies, have imaginary

wavenumbers. In a plate, in addition to the Lamb waves' modes, there also exists a set of wave motions known as shear horizontal (SH) modes. The particle displacements caused by any of these SH modes are in a plane that is parallel to the surface of the plate, as shown in Fig.1.16. In this figure the wave propagates in direction x_1 and the particles displacements are in the direction x_3. Also the SH modes derive from the superpositions of the fundamental bulk waves. However, these modes do not have such an important role in SHM applications, so the interest in this work is focus mainly on Lamb waves modes.

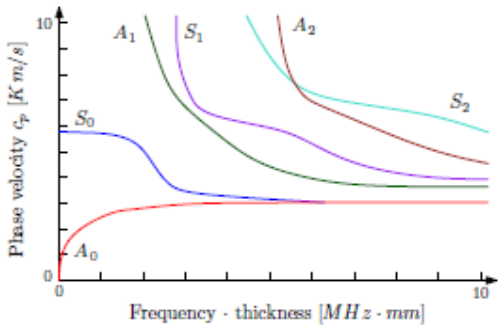

Fig. 1.15 - Phase velocity dispersion curves for an aluminum plate

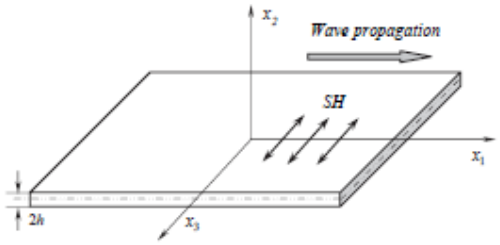

Fig. 1.16 - SH wave mode propagation

2. INNOVATIVE SHM TECHNIQUES BASED ON SLDV MEASURES

The SHM procedure here considered concerns innovative techniques for a structural monitoring of aeronautical components, all of them based upon the use of a Scanning Laser Doppler vibrometer SLDV. The vibrometer is used to detect the dynamic response of the component under test, in wave propagation regime. The signal so recorded consists of space and time maps of vibration velocity off-plane. The purpose of the study lies in the analysis of such maps, using filtering techniques that separate reflected waves from the incident ones, so that they can enable to identify defects. The study also intends to evaluate the possibility of diffused defects of "wrinkling" kind, using the filtering methods above mentioned or other techniques to be considered later on in this study.

In a SLDV, the laser beam placement is controlled by a user-defined grid on the structure. This offers the possibility of accurately estimating deflection derivatives of various orders and in turn allows the estimation of curvatures and strain energy distributions. Such measurement refinement is unattainable in a timely manner using accelerometers and/or strain gauges. Furthermore, the damage index formulation presented in [30, 27] requires the use of data from an undamaged structure to be used as a reference. This can represent a problem towards the practical implementation of the technique, as historical data may not always be available and variations may be induced by a number of reasons other than structural damage. A novel technique, introduced by Ruzzene and applied in this work to composite specimens, allows the generation of baseline information directly from the measured dataset. Specifically, reference data are synthesized by under-sampling measurements recorded directly on the damaged specimen. In the first paragraph details of the technique in object can be found, while in the following chapter our practical application of such a technique descending from the experimental analysis is reported. Through this technique, it is possible to by-pass the ignorance of baseline data, obtaining detailed information inhering the damaged sites.

Furthermore, full wavefield measurements obtained with a scanning laser vibrometer can be combined with effective signal and imaging processing algorithms to support characterization of guided waves as well as detection, localization and quantification of structural damage. These wavefield images contain a wealth of information that clearly show details of guided waves as they propagate outward from the source, reflect from specimen boundaries, and from discontinuities within the structure. The analysis of weaker scattered waves is facilitated by the removal of source waves and the separation of wave modes, which is effectively achieved via wavenumber–frequency domain filtering in conjunction with the subsequent analysis of the resulting residual signals. Incident wave removal highlights the presence and the location of weak scatterers, while the separation of individual guided wave modes allows the characterization of their separate contribution to the scattered field and the evaluation of mode conversion phenomena. The effectiveness of this method is demonstrated through its application to detection of a delamination in a composite stiffened plate and detection of defect/wrinkling in a T-shaped skin to stringer component, as shown in chapter 3.

2.1. DAMAGE MEASURE BASED ON ENERGY FUNCTIONAL DISTRIBUTION

Some authors have used curvatures for the evaluation of the strain energy distribution over the structure under consideration. This approach has been pursued for example by [26] to formulate a damage index based on the comparison of strain energy distribution for damaged and undamaged structures. In [26] and in subsequent papers by the same authors, the technique is applied to beam structures using mode shapes, ODS or time-domain data to obtain information on both damage location and extent. The same technique was extended to plate structures in [27], where accelerometers are used to measure the deflections to be interpolated for successive differentiation. The basis if the technique can be easily illustrated in the case of a beam in bending, for which the strain energy is given by:

$$U_i = \frac{1}{2}\int_0^L EI(x)\phi_i^2(x)_{,xx}\,dx \qquad (2.1)$$

where L and EI respectively denoting the beam's length and flexural stiffness, while $\phi_i(x)$ is the beam's Operational Deflection Shape (ODS) corresponding to its excitation at the i-th natural frequency. The beam is subdivided into N regions so that its total strain energy can be expressed as in [27] (fig. 2.1)

$$U_i = \frac{1}{2}\sum_{k=1}^{N} EI_k \int_{x_k}^{x_{k+1}} \phi_i^2(x)_{,xx}\,dx \qquad (2.2)$$

$$U_i = \sum_{k=1}^{N} U_{ik} \qquad (2.3)$$

where it is assumed that the flexural rigidity of the beam over each region is constant.

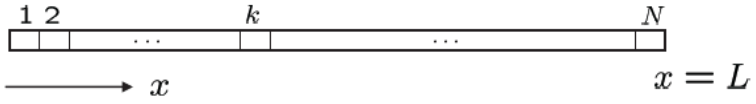

Fig. 2.1 - Flowchart of SHM based damage identification process

In addition, it is assumed that damage is localized in a single region k=p, and that at the damage location:

$$\frac{U_{ip}}{U_i} \approx \frac{U_{ip}^*}{U_i^*} \qquad (2.4)$$

So an estimation of the reduction in stiffness rigidity can be obtained as:

$$\frac{EI_p^*}{EI_p} \approx \frac{U_i^* \int_{x_p}^{x_p+1} \phi^2(x)_{,xx}\, dx}{U_i^* \int_{x_p}^{x_p+1} \phi_i^{*2}(x)_{,xx}\, dx} = f_{ip} \qquad (2.5)$$

Therefore, the ratio f_{ip} is considered damage measure. The damage measure is expected to be equal to 1 over the undamaged regions and different than one over a damaged region. It is in general convenient to combine information obtained from the analysis of several modes (I) and therefore to consider a cumulative damage measure, defined as

$$f_k = \frac{1}{I} \sum_{i=1}^{I} f_{i_k} \qquad (2.6)$$

This cumulative index provides a single piece of information, which combines the results from several ODS's and associated strain Energy distributions. ODS's not affected by damage, because its particular location will not contribute, will give unit contributions, whereas the index for modes altered by the defect will be combined to provide a robust indication of a defect.

2.2. INTERPOLATION OF THE MEASURED RESPONSE AND SYNTHESIS OF THE UNDAMAGED BASELINE

The damage index as proposed in [27] is based on a comparison between damaged and undamaged strain energy over the considered region of the structure. In practice, however, it may be difficult to have or to obtain baseline information from structures to be analyzed. This, in fact, assumes that either an undamaged specimen or that historical data of the same kind of those currently being collected are available. This limitation can be overcome in the presence of high spatial resolution of the measurements, as provided for example by SLDVs. The technique, introduced in [8], synthesizes undamaged information through spatial decimation of the response.

In the proposed approach, the ODSs are measured at several locations over the structures, so that spatial derivatives can be accurately estimated through spline interpolation of the measured data. The ODS $\phi(x, y)$ for a plate structure can for example be approximated as:

$$\phi(x, y) \cong \sum_{p,q} h_p(x) h_q(y) \Phi_{p,q} \qquad (2.7)$$

where $\Phi_{p,q}$ defines the value of the ODS measured experimentally at the sensor location p, q, or at a point of a SLDV grid, while $h_p(x)$, $h_q(y)$ are spline basis functions. The curvature estimations can be obtained by taking derivatives of the spline functions, while keeping the nodal or measured values as weighting parameters.

Baseline information can be generated by using a subset of the measurement points. The baseline interpolated deflection can be expressed as:

$$\phi^*(x, y) \cong \sum_{r,s} h_r(x) h_s(y) \Phi_{r,s} \qquad (2.8)$$

where r, s are a subset of the measurement grid points p, q, such that r<p, s<q. The resulting under-sampling of the data has the purpose of intentionally "missing" any discontinuity or anomaly corresponding to damage, which can generally be detected only through a refined measurement grid. The baseline information can be then differentiated and used for the estimation of the strain energy generically denoted as U^*.

This technique is demonstrated experimentally on a composite plate with stiffeners (never done before).

2.3. STRAIN ENERGY DISTRIBUTUION

The technique presented previously can be easily adapted to transient time signals corresponding to GUW propagation. The strain energy distribution of eq. (2.1) can be rewritten in terms of displacements $w(x,t)$ and corresponding curvatures in the time domain:

$$U_i(t) = \frac{1}{2}\int_0^L EI(x) w_{,xx}(x,t)^2 \, dx \qquad (2.9)$$

Again, undamaged or baseline information can be synthesized through the decimation process described in Section 2.2 assuming a sufficient number of measurement locations is available. This formulation leads to a time dependent damage, which can be represented as maps that evolve over time as waves propagate within the structure. The advantages of a time domain damage measure include the possibility of limiting the investigation to a particular time window. In fact, a recognized problem in wave propagation-based inspections arises when the incoming wave hides the presence of damage and resulting wave reflections. The analysis of the trailing part of the wave, after the main pulse has decayed, is often rich in information regarding damage location and extent, as damage generally behaves like a secondary wave source. The considered time domain formulation allows selecting the time interval where structural response and associated energy distribution are most affected by damage. Examples of results obtained through this approach are presented in what follows. Wave propagation tests are performed on composite stringerized specimens with artificial delamination and wrinkling. Looking at the snapshots of the recorded response will demonstrate the complexity of the wavefield, as a result of the structural complexity. In particular, it is shown how, in the case of the stiffened panel, the stiffeners tend to reflect the wave and cause it to propagate perpendicularly to their length. Such a behavior makes the interpretation of the signals through standard time-of-flight estimation particularly difficult, as it would be almost impossible to differentiate multiple reflections from the one associated with the damage. The application of the considered damage measure, on the contrary, does not require previous knowledge of the response of the

structure, nor does it rely on the availability of a model. It thus represents an attractive solution for the analysis of complex or built-up structures.

2.4. FILTERING OF SIGNALS IN DOMAIN WAVENUMBER / FREQUENCY

The paragraph aims to show the technique of filtering utilized, referring to a mono-dimensional illustrative case. Let us examine the propagation of a wave with 1D stress in a non dispersive medium defined by the limitations $0 \le x \le L$, x being a given Cartesian coordinate and L the whole longitudinal dimension of the medium. We assume here the presence of a discontinuity in the material corresponding to abscise x=x0, separating the medium in the region $0 \le x \le x0$ (region 1) and in the region $x0 < x \le L$ (region 2). If we indicate with t the variable of the time, the stress 1D $\sigma_x(x,t)$ in the region 1 can be expressed as the sum of an incident wave $\sigma_x^i(x,t)$ and of a reflected wave $\sigma_x^r(x,t)$, according to the following expression

$$\sigma_x(x,t) = \sigma_x^i(x,t) + \sigma_x^r(x,t) \tag{2.10}$$

where

$$\sigma_x{}^{(r)}(x,t) = g(t + \frac{x}{cL_1} - 2\frac{x_0}{cL_1}) \tag{2.11}$$

$$\sigma_x{}^{(i)}(x,t) = f(t - \frac{x}{cL_1}) \tag{2.12}$$

Being f e g two specific shape functions and cL1 the phase velocity in region 1. By imposing the additivity condition of velocity and stress at the interface x=x0

$$\dot{u}^{i}(x_0^{(-)},t)+\dot{u}^{r}(x_0^{(-)},t)=\dot{u}^{t}(x_0^{(+)},t) \tag{2.13}$$

$$\sigma_x^{i}(x_0^{(-)},t)+\sigma_x^{r}(x_0^{(-)},t)=\sigma_x^{t}(x_0^{(+)},t) \tag{2.14}$$

where $\dot{u}^{t}(x_0^{(+)},t)$ and $\sigma_x^{t}(x_0^{(+)},t)$ indicate, respectively, velocity and stress of the wave transmitted to the region 2, we get the known relation between the functions f and g:

$$g(\bullet)=Rf(\bullet) \tag{2.15}$$

The reflection coefficient is related to the density ρ and the wave velocity cL of the two domains 1 e 2 through the relation:

$$R=\frac{\rho_2 cL_2/\rho_1 cL_1-1}{\rho_2 cL_2/\rho_1 cL_1+1} \tag{2.16}$$

The transmitted stress wave is expressed as follows:

$$\sigma_x^{(t)}(x,t)=Tf\left(t-\frac{x}{cL_2}\right) \tag{2.17}$$

being T the Transmission coefficient provided by

$$T=\frac{2\rho_2 cL_2/\rho_1 cL_1}{\rho_2 cL_2/\rho_1 cL_1+1} \tag{2.18}$$

Let us consider the propagation of a harmonic stress wave of frequency ω_0 and amplitude A_0, which corresponds to the following shape function:

$$f(T)=A_0 e^{i\omega_0 T} \tag{2.19}$$

In this case, the stress distribution in region $0 \leq x \leq x0$ is provided by the relation:

$$\sigma_x(x,t) = A_0\left[e^{i\omega_0(t-\frac{x}{cL_1})} + \mathrm{Re}^{i\omega_0(t+\frac{x}{cL_1}-2\frac{x_0}{cL_1})}\right] = \quad (2.20)$$
$$A_0\left[e^{i(x_0t-k_0t)}(k-k_0) + \mathrm{Re}^{i(\omega_0t+k_0t-2k_0x_0)}\right]$$

In which $k_0 = \omega_0 \big/ cL_1$ denotes the wavenumber. Let us assume now that both the spatial information and the temporal one are available for the stress distribution in the domain. Under this assumption, the 2D Fourier Transform of $\sigma_x(x,t)$ can be evaluated, obtaining

$$\sum_x(k,\omega) = \int_{-\infty}^{+\infty}\int_{-\infty}^{+\infty}\sigma_x(x,t)e^{-i(\omega t+k_x)}dxdt = F_{2D}\left[\sigma_x(x,t)\right] \quad (2.21)$$

Specifically, in the present case

$$\sum_x(k,\omega) = A_0\delta(\omega-\omega_0)\left[\delta(k-k_0) + R^{2ik_0x_0}\delta(k+k_0)\right] \quad (2.22)$$

being δ the Dirac delta function. The 2D –FT graph defined by (2.22) will show two peaks in the frequency/wavenumber domain, in correspondence of frequency $\omega = \omega 0$ and of two wavenumbers $k = \pm k0$, which will coincide, respectively, to the incident and the reflected wave.

The 2D-FT separates in an efficient manner such two components and allow the application of a window that filters one of them, for example that corresponding to the reflected wave. Upon filtering, the residual signal can be transformed again through an inverse Fourier Transform in the domain space/time, easily obtaining a filtered wavefield ready for visualization and processing. Such a procedure is particularly useful for damage detection, because the reflected waves typically transport information regarding the presence and the nature of

structural damages and discontinuities. In a lot of practical situations, the reflections are small in amplitudes and hidden by noise and incident wave, which makes difficult damage identification and characterization. From a mathematical point of view, the 'windowing' process can be obtained by introducing the following product function of 2D-FT and of a 2D “window” function:

$$\sum\nolimits_x^{(r)} k,\omega \approx \left[1 - H(k - k_0, \omega - \omega_0)\right] \sum\nolimits_x (k,\omega) \qquad (2.23)$$

In the latter relation, the quantity $H(k - k_0, \omega - \omega_0)$ denotes the “window”, centred in the point of coordinates k0, ω0, in the frequency/wavenumber domain. The approximation in the space/time domain of the reflected wave is provided by the following relation:

$$\sigma_x{}^{(r)}(t,x) = F_{2D}^{-1}\left[\sum\nolimits_x^{(r)}(k,\omega)\right] \qquad (2.23)$$

in which F_{2D}^{-1} denotes the inverse Fourier transform F_{2D} .

In the following chapter, the practical application of the filtering techniques for the reflected wave detection, travelling in different sub-elements (for the first time placed perpendicular to each others) of the components under test can be found.

3. EXPERIMENTAL ANALYSIS

One of the tasks in this study has concerned the carrying out of a test as a proof of the SHM technique in a composite material: Lamb wave excitation in the structure and the analysis of the interaction of these with potential defects/damages present. The experimental activity was carried out in the acoustic laboratory of Alenia, using mainly instruments available in it. The phase considered has completed the following activities:

1.1 Instrumentation of the component under test;
1.2 Registering data through Polytec PSV 400 laser Vibrometer;
1.3 Data conversion from Vibrometer Laser to Matlab visualization;
1.4 Analysis of the maps indicating the velocity values observed and first hypothesis about the presence of structural defects.

Figures 3.1, 3.2 and 3.3 show the devices used and the component tested. Figure 3.4 shows, in detail, the area considered for the assessment of the presence of wrinkling damages, corresponding to a small portion of the connection between skin and web. In the following paragraphs we will describe the measurement setup and the main results obtained with the tests done over different sub elements of the component shown in picture 3.4; skin: external side and interior side 1 and 2; web: side 1 and side 2).

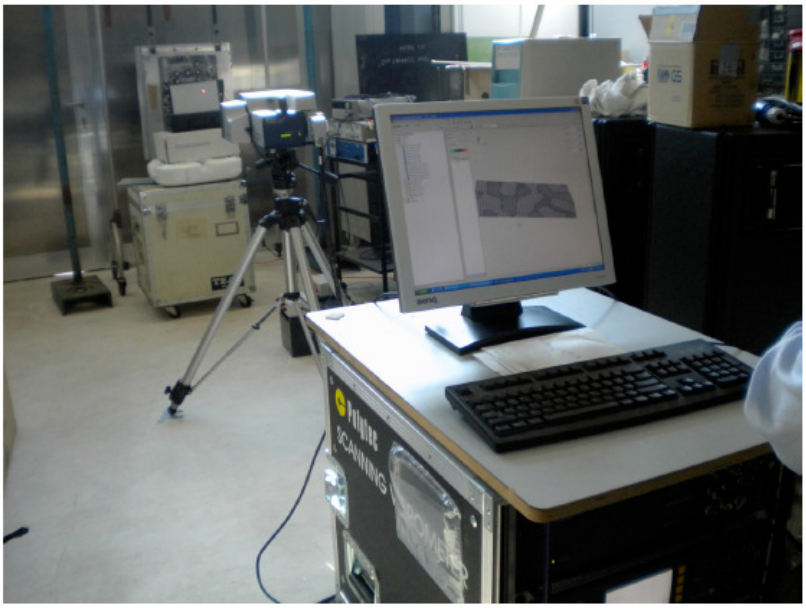

Fig. 3.1 - Laser Vibrometer used for the tests and for the data acquiring system

Fig. 3.2 - Voltage amplifier and signal generator employed for piezoelectric excitation

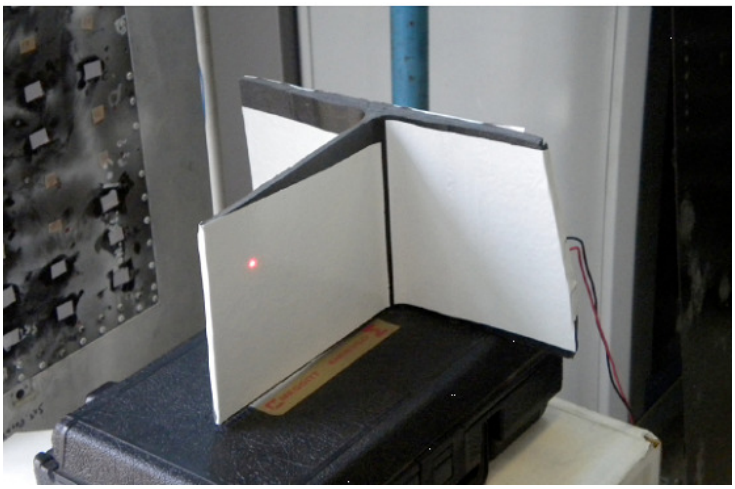

Fig. 3.3 - Component under test

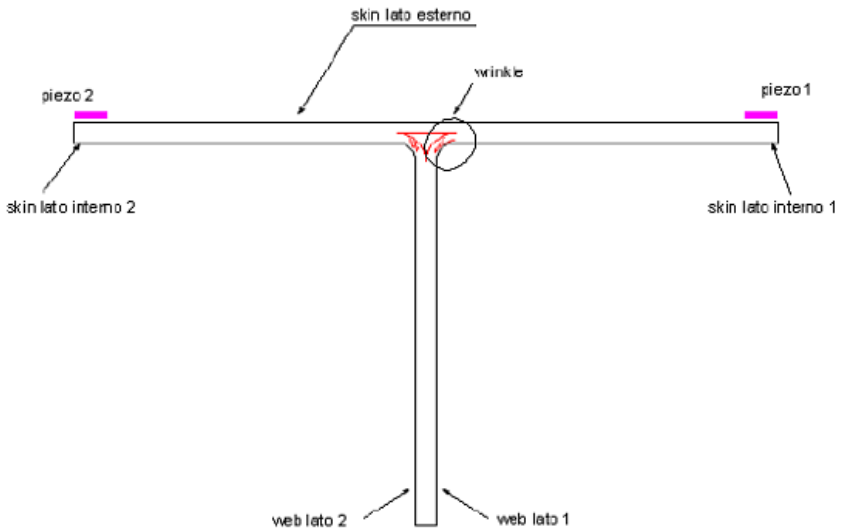

Fig. 3.4 - Section with a horizontal piano of the component under test, with indication of the position of the actuators used for the tests, of the nomenclature of the different subcomponents analyzed and of the area subject to potential wrinkling.

3.1. DESCRIPTION OF THE MEASURE SET UP

The Vibrometer used for the test ("Scanning Laser Doppler Vibrometer" o SLVD - type Polytec PI, Model PSV400M2) is characterized by a limited band frequency, with a maximum limit equal to 100 kHz, allowing the observation and visualization of ultrasonic waves. The component under test has been excited using a sinusoidal burst for a period of 0.2 ms, created by a signal generator HP 33120° amplified to 200 volt. The impulse has been transferred to the component using piezos with a diameter of 1 cm (piezo 1 and 2). The actuators have been fixed on the skin using epoxy glue, in order to enhance the best coupling and, then, the best transmission of energy between the vibration generated by the actuator and the component on which the latter has been fixed. The component has been covered with reflecting material to allow the best reflection of the incident laser ray and, therefore, a good measure sensitivity. The material used for the test, actually, absorbs a huge quantity of light, which reduces the accuracy of the test itself. The adding of the reflecting ray embodies a solution of easy application and doesn't at all influence the dynamic behaviour of the component itself, because of its very thin thickness. It's easily predictable that, during the practical implementation of this research system, it may be possible to realize an optimization of the excitation parameters (frequencies, amplitudes, wavelengths of the Laser) in order to carry out accurate measurement even without the presence of the reflecting ray.

3.2. ACQUISITION PARAMETERS

The vibration velocities excited in the sample have been registered by the SLVD on specific grids of placed on the sub-elements shown in pictures 3.4 of the component put under test (1 skin or wing panel: exterior side and inner side 1 e 2; web: side 1 and side 2). The phase information is kept by "triggering" of the excitement signal with an inferior frequency signal which also defines the scanning frequency. The schematic representation of the experimental setup availed is shown in Fig. 3.5. Corresponding to each point of the measure grid a media has been calculated among 20 measures on time, each one referring to the

same point at different instants, in order to reduce the background disturbance. The repetition frequency of the impulse in entrance has been set on 20 Hz. The data so acquired have been filtered through a pass band filter ranging from 10000 to 70000 Hz, to reduce even more the background noise of the signal.

Once ended the recording of the vibration velocity, corresponding to all of the points of the given grid, the measures recorded have been post-processed to obtain propagation maps of the wavefront. The measures taken have detected the vibration velocity off-plan of the points aligned with the laser ray during the scanning. Figures 3.6 and 3.7 show the signal generated in entrance and the answer velocity-time corresponding to a given measure point. For all of the tests carried out, the excitement signal (fig. 3.5), consists of a sinusoidal impulse of 0.02 msec period, corresponding to a frequency of about 50 kHz. The frequency of the signal has been selected so to be centred over the acquisition (band) available in the device, which is limited to about 100 kHz. The spectrum of the signal shown in fig. 3.6 attests how the selected signal is such to provide a broadband excitement covering the whole frequency interval available in acquisition. Figure 3.7 shows the time history of the answer measured at a point representative of the test. The signal highlights the presence of a first peak corresponding to the arrival in the given point of the main wave, followed by a series of oscillations of minor extent, corresponding to the decay of the response and to the subsequent arrival of reflections from the edges and of structural discontinuities of various natures.

The content in frequency of the signal shown in fig. 3.7 is particularly interesting for the following reasons:

- The spectrum of the signal shows the energetic content of the signal at the different frequencies.
- In the specific case considered, the energy of the signal is concentrated in particular frequency intervals which are determined by the dynamic interaction between the actuator and the component. Such interaction, essentially, filters the signal in entrance and alters its content in frequency. In this case, it can be observed that the frequency intervals between 20-40 Hz and 49-60 Hz show the highest energy values (spectrum amplitude).

- The frequency intervals with a maximum energy response are widely included within the limits of acquisition of the availed device which can be therefore considered adequate for the measurement of the propagation of the waves generated by the specific 50 kHz signal, used in these tests.
- The maximum frequency availed (about 100 kHz) is anyway a huge limitation as to the wavelengths that can be generated in the test. The wavelength is a basic parameter for the evaluation of the responsiveness of the non destructive inspection system based upon elastic waves, because the dimensions of the recordable defects are in the order of the wavelength itself. The here considered 50 kHz excitation, chosen according to the band-acquisition capacity of the SLVD device available produces wavelengths that are rather long and which then strongly limit resolution of investigation. The wavelengths detected during the tests are evaluated by the analysis presented later.

The results of the measurements taken corresponding to the various tested subcomponents are shown in the following paragraphs.

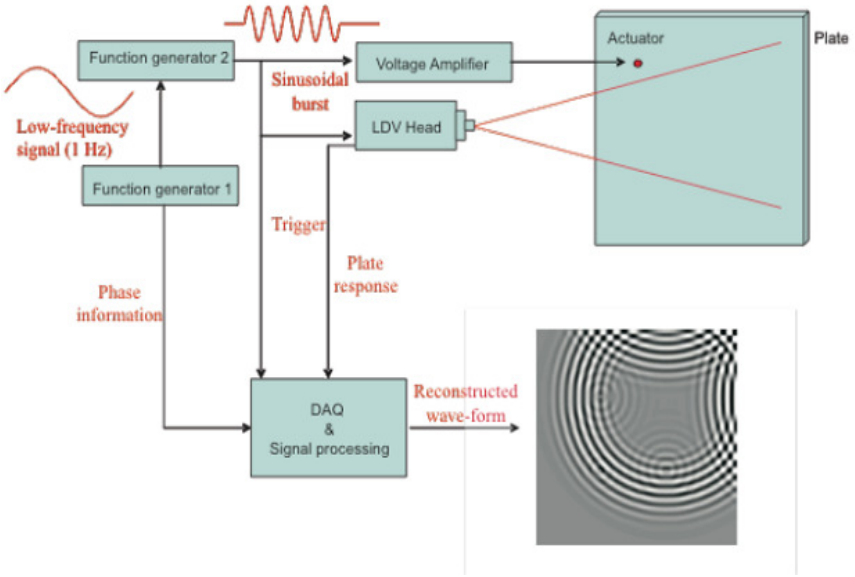

Fig. 3.5 - Schematical description of the measurement setup utilized

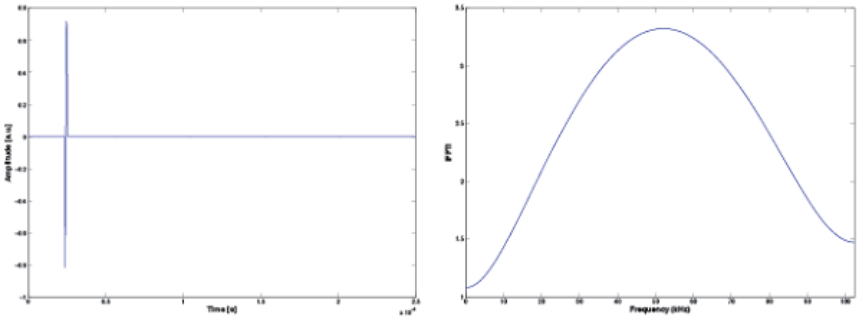

Fig. 3.6 - Impulse generated in entrance (left) and corresponding Fourier Transform (right)

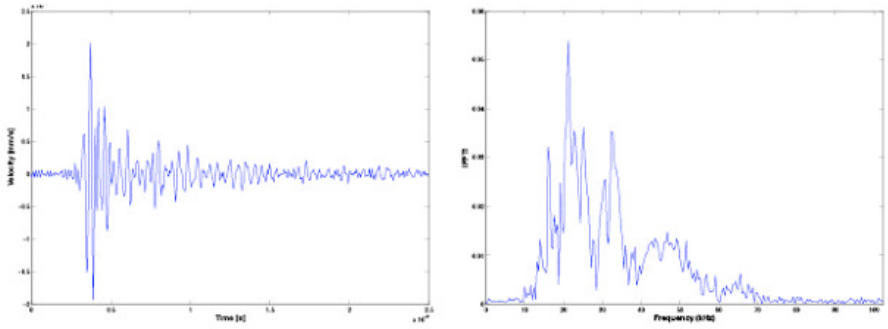

Fig. 3.7 - Signal recorded corresponding to a measure point of the laser vibrometer (left) and corresponding Fourier Transform (right).

3.3. RESULTS

Figure 3.8 shows the pattern of the Lamb waves excited in the two piezos placed on the exterior side of the skin panel. Such peculiar configuration has been examined to evaluate the interaction of the travelling waves with possible wrinkling defects in the area of connection skin - web. Such area consists of the union of the skin panel with the two C elements forming the web. The connection is filled with filler material, as shown in detail in fig. 3.9.

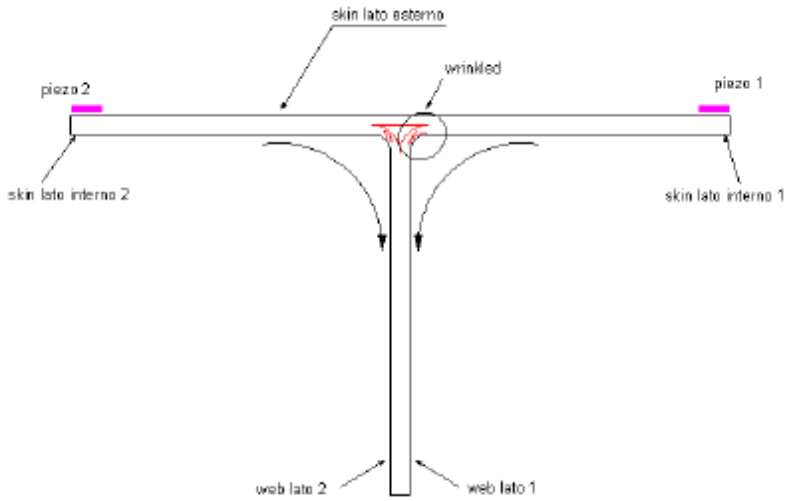

Fig. 3.8 - Pattern of the lamb waves excited in the component under test

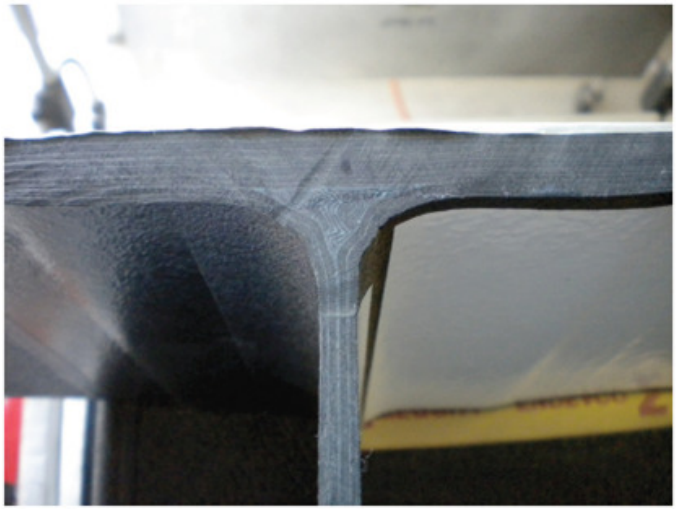

Fig. 3.9 - Detail of the connecting element skin-web

3.3.1. SKIN EXTERNAL SIDE

The vibration velocities excited on the skin panel - external side through the (piezo 2) have been recorded on an analysis grid consisting of 943 points. Figure 3.10 shows such grid and various "snapshots" of the frontwave propagating on the here considered subcomponent. Figure 3.11 shows, instead, a map of the mean square in time ("root mean squared" or RMS) of the response corresponding to each given point.

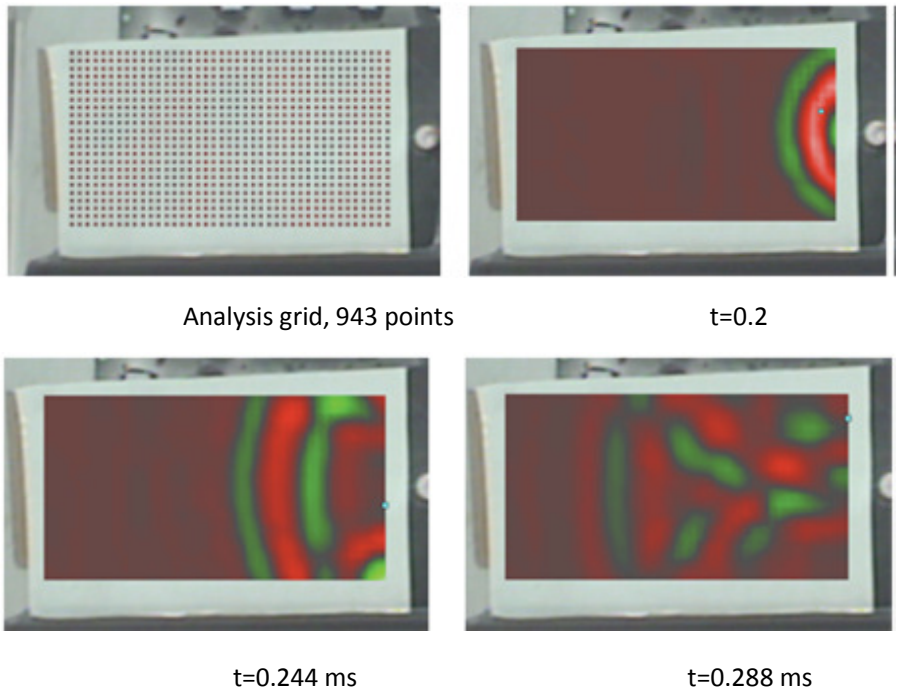

Fig. 3.10 - Sampling grid and snapshots of the wavefront at various instants on the skin external side

The RMS map of picture 3.11 provides essentially the spatial distribution of the energy corresponding to the wave propagation. In the considered case, it can be observed that the energy is mainly concentrated in right half of the measuring area that is corresponding to the piezo used for the excitation. The concentration

of the energy close to the excitement source is also produced by reflections caused by the presence of the web below, which has the effect to confine the waves mainly within the right half of the measurement area. This reflection caused by the web will be furthermore highlighted by the analyses of the filtered signals, which will be presented later on.

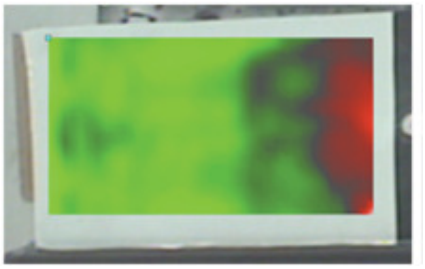

Fig. 3.11 - RMS map on the skin external side

3.3.2. SKIN INTERNAL SIDE '1'

The vibration velocities excited on the skin panel internal side 1 through the piezo 1 have been recorded on an analysis grid consisting of 2009 points. See figures 3.12 e 3.13 for the snapshots of the wavefront taken in different instants and for the response RMS map.

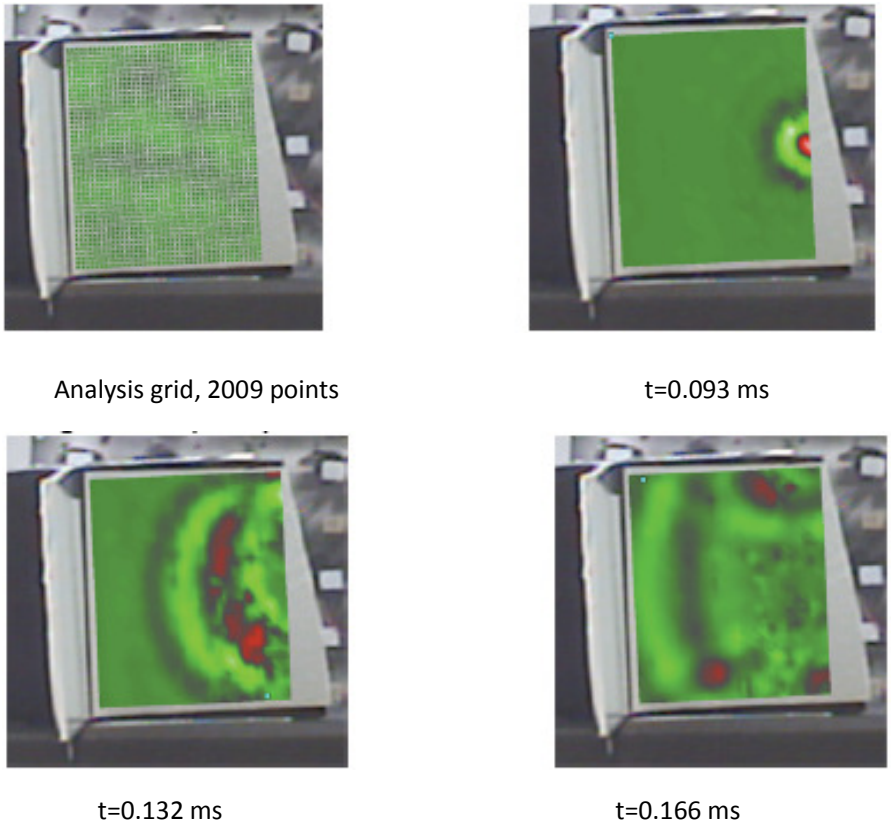

Fig. 3.12 - Sampling grid and snapshots of the wavefront at various instants on the skin internal side 1

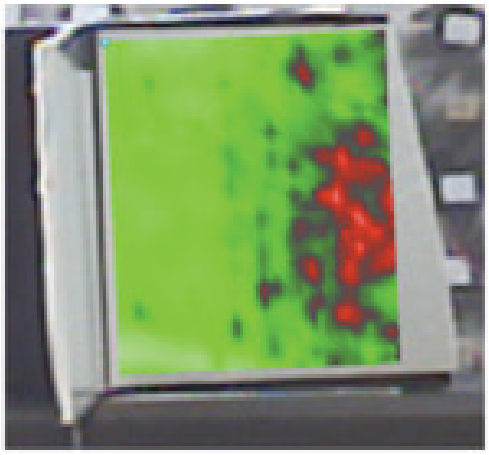

Fig. 3.13 - RMS map on the skin internal side

As in the previous case, the RMS response shows a concentration of energy close to the excitation source which may as well be caused by the increment of the component thickness, corresponding to the ply-drop-off (junction between skin and C web, see figure 3.14).

Fig. 3.14- Detail of the area with reducing thickness partially responsible for the energy concentration.

3.3.3. WEB SIDE '1'

The vibration velocities excited on the web panel side 1 through the piezo 1 have been recorded on an analysis grid consisting of 2541 points. See figures 3.15 and 3.16 for the snapshots of the wavefront at different instants and the RMS response map.

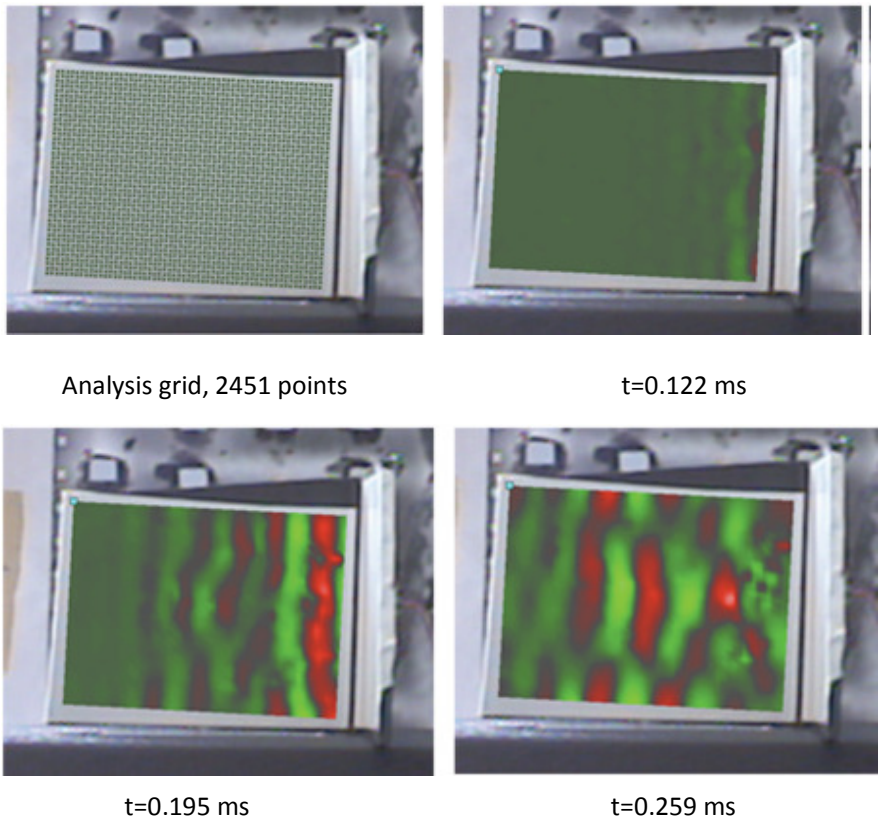

Fig. 3.15 - Sampling grid and snapshots of the wavefront at various instants on the webside 1

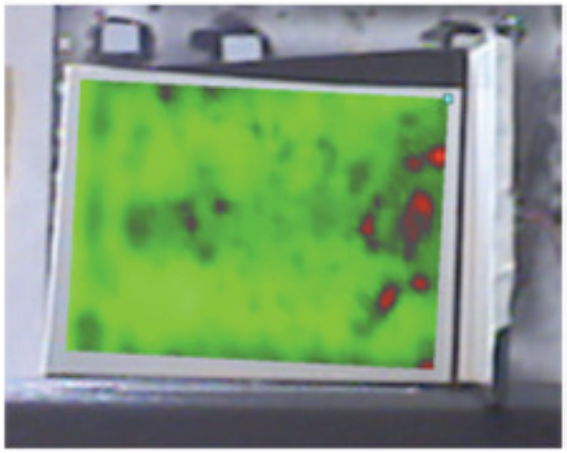

Fig. 3.16 - RMS map on the web side 1

The RMS map in fig. 3.16 shows an accumulation of energy close to the (junction) radius corresponding to the area of union of the two C webs. Such concentration of energy may denote the presence of porosity in the bonding zone. The presence of non homogeneous material in this area is also highlighted by the distortion of the wavefield that can be observed in the snapshots shown in fig. 3.16. The area potentially concerned with high porosity has been also underlined in the following fig. 3.17.

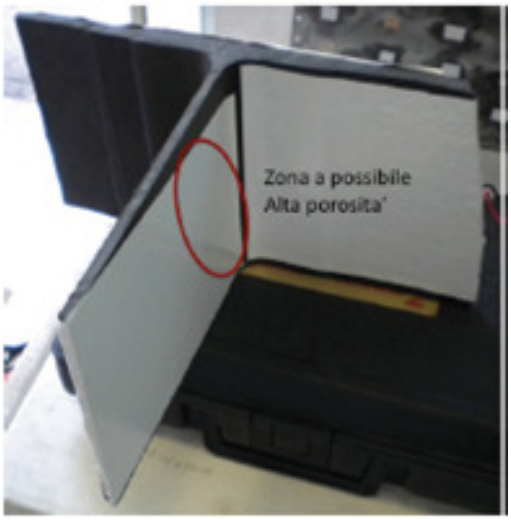

Fig. 3.17 - Detail of the area potentially concerned by high porosity

3.3.4. SKIN INTERNAL SIDE '2'

The vibration velocities excited on the skin panel internal side 2 through the piezo 2 have been recorded on an analysis grid consisting of 1295 points. See figres 3.18 and 3.19 for the snapshots of the wavefront at different instants and the RMS response map.

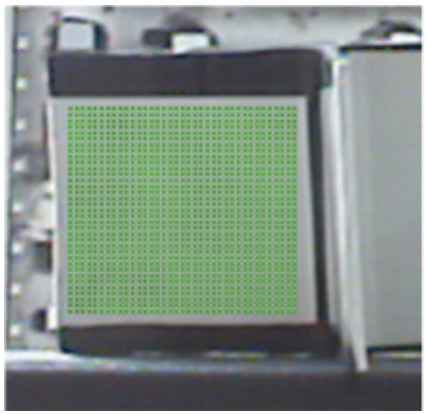

Analysis grid, 1295 points

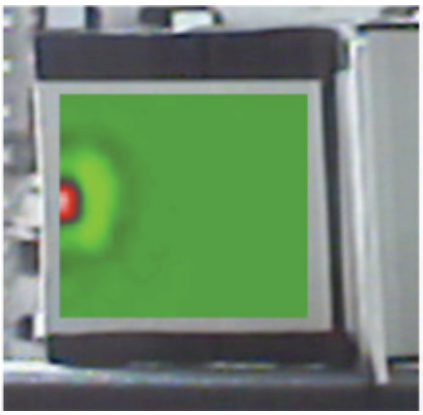

t=0.093 ms

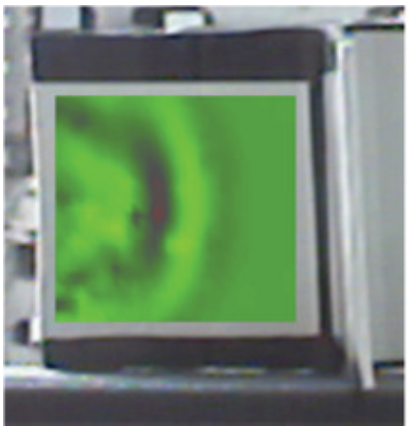

t=0.127ms

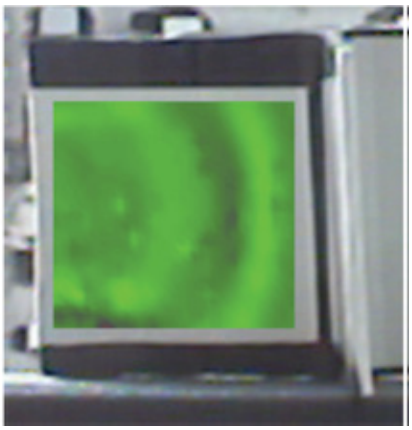

t=0.151 ms

Fig. 3.18 - Sampling grid and snapshots of the wavefront at different instants on the skin internal side 2

Fig. 3.19 - RMS map on the skin internal side 2

In the case here considered the RMS map doesn't highlight any particular observation and simply gives evidence of a peak of concentration close to the piezo (red zone in Fig. 3.19).

3.3.5. WEB SIDE ‘2’

The vibration velocities excited on the skin panel internal side 2 through the piezo 2 have been recorded on an analysis grid consisting of 1155 points. See figures 3.20 and 3.21 for the snapshots of the wavefront at different instants and the RMS response map.

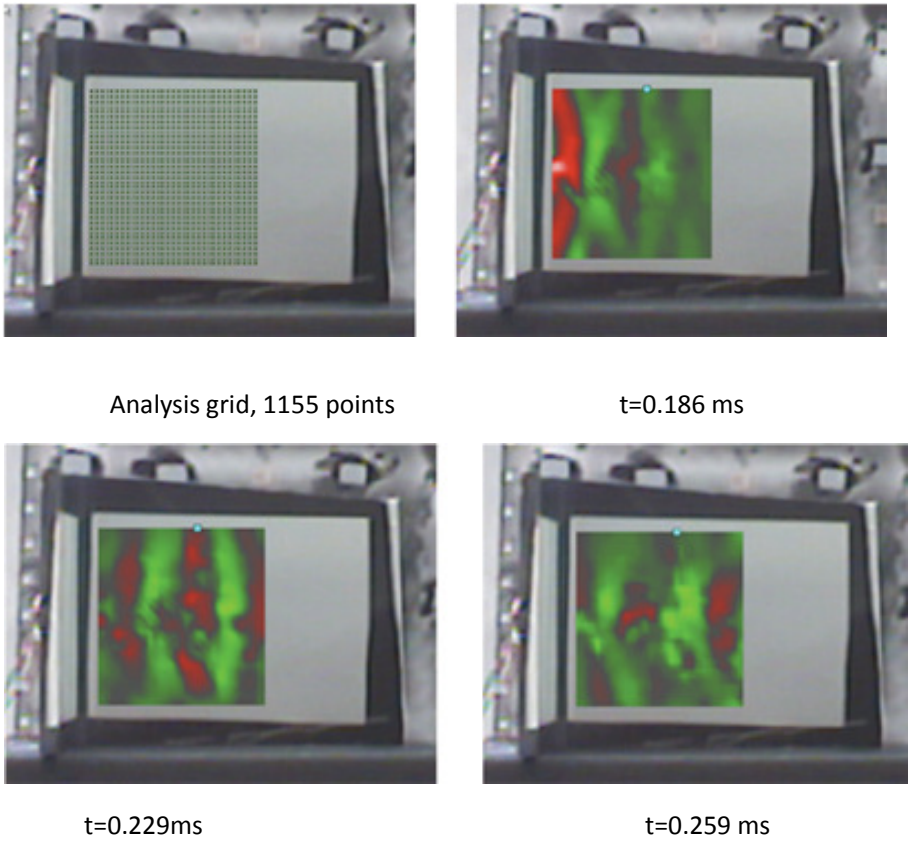

Fig. 3.20 - Sampling grid and snapshots of the wavefront at different instants on the web side 2

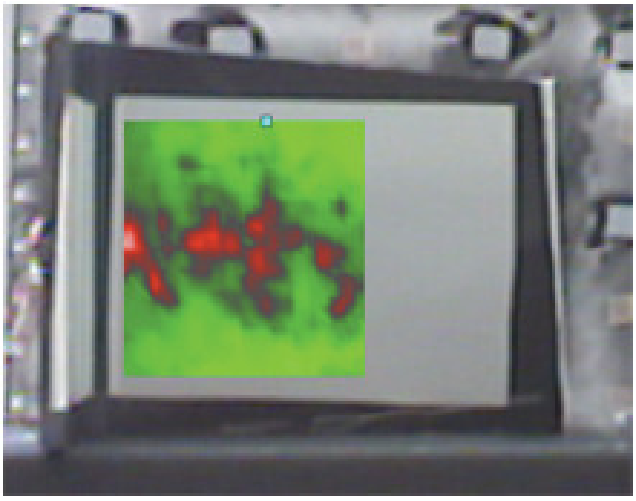

Fig. 3.21 - Map of the mean square recorded during the time of the vibration velocities measured on web side 2

3.4. ANALYSIS OF THE WAVELENGHTS GENERATED

In conclusion, it is necessary to analyze the wavelength excitable with the use of the available devices, in order to carry out a global evaluation over the defects that may be observed after the test made. The data measured on the skin are here taken as a benchmark, assuming that the measurements examined in the other areas express similar wavelengths. Figure 3.22 shows a snapshot of the wavefield enabling to evaluate roughly the wavelength by calculating the distance between two subsequent peaks in the front. A more accurate estimation may be obtained by analyzing the response in the domain of the wavenumbers and the frequency. The latter kind of analysis is based upon a Fourier transform 2DFFT of the response measured in the zone of the measure taken both in time

and in space. What we get at the same time is information about the content in terms of frequency and about the content in terms of wavenumber (spatial frequency) of the signal. The wavenumber is strictly depending on the wavelength according to the relation $\lambda = 2\pi/\kappa$, where λ is the wavelength, while κ is the wavenumber. Figure 3.23 shows the representation of the response on the skin in the domain wavenumber/frequency. In the chart the colors represent the amplitude of the signal, with the red color showing the highest amplitudes. The localization of the maximum in terms of frequency and wavenumbers κ enables to identify the main components in the response. Considering the tests described in the previous paragraphs, the wavenumber corresponding to the highest amplitude is more and less equal to k=150-200 rad/m, which corresponds to: $\lambda \equiv \frac{2\pi}{\kappa} = 3-4cm$.

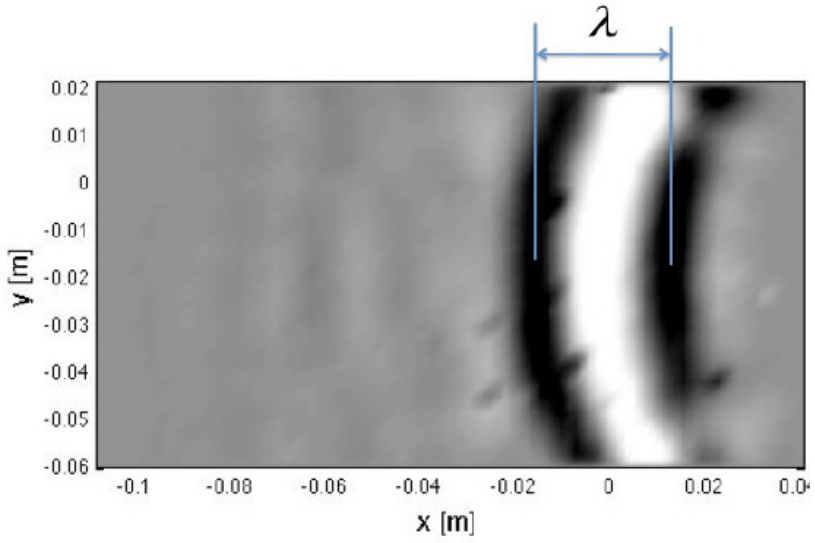

Fig. 3.22 - Wavelenght highlighted in a snapshot of the wavefront on the skin

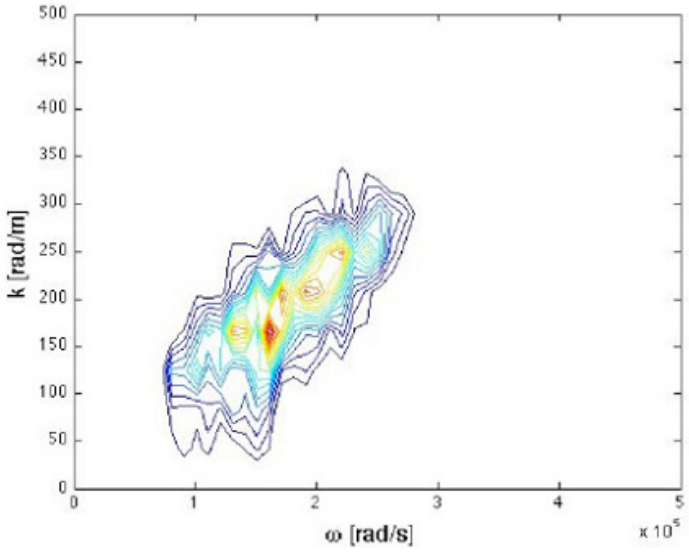

Fig. 3.23 - Representation of the response measured in the domain wavenumber/frequency

3.5. FIRST CONCLUSIONS

The results obtained allow concluding as follows:

- The tests carried out show how the device available, specifically the SLDV with a sampling frequency ranging up to 100 kHz, is able to measure the propagation of elastic Lamb waves in components of composite material.
- The excitation produced using piezoelectric discs determines a response whose energy concentrates itself on frequencies contained in the field of acquisition of the SLDV.
- The Lamb waves are a really good device for the analysis of the structural integrity and the detection of defects in the junction zone of components formed by skin + web. Tests show, in particular, that the Lamb waves propagate in such component

and are transmitted over parts placed perpendicular to each others. This suggests the possibility of generating waves on the skin to measure the response of the web and vice versa. A configuration of great practical utility may be obtained permanently placing some actuators on the two opposite sides of the web and measuring the response on the external side of the skin, easily accessible.

- The experimental results obtained show the possibility of detecting defects in the bonding zone between the two C web.
- The wavelengths recorded in the wavefields available are probably too big for little defects to be detected such as, for instance, localized wrinkling defects.

Further elaborations of the data obtained will include the analysis listed as follows:

- Filtering of the data in the domain wavenumber/frequency. These procedures will enable to remove the incident waves from the wavefield, emphasizing more neatly the presence of reflections corresponding to structural discontinuities due to manufacturing defects.
- Evaluation of differences in terms of shape and modalities of propagation/reflection of acoustic waves, comparing the relative results obtained to those concerning area with no wrinkling o little wrinkling to areas with a sharper wrinkling (web side '2' and web side '1', respectively, in the case of the component considered picture 4). This kind of analyses will also enable to evaluate the presence of possible distortion in the propagation of the waves produces by the wrinkling.
- Comparative analysis of the propagation of acoustic waves on the opposite sides of the web will represent a starting point to develop further diagnostic methods based upon the comparison of the wave amplitudes, the times for propagation, the contents in terms of frequency and the energy altogether transported by

acoustic (travelling) waves over the area touched or not by the wrinkling.

3.6. ELABORATION OF THE SLDV DATA PREVIOULSY OBSERVED

Hereinafter follows a study of elaboration of the SLDV data so far described.

The main processing technique used for the SLDV data in the present study analyzes the wave field within the domain wavenumber/frequency, in order to obtain the detection, visualization and characterization of possible structural damages. The data of the whole wavefield contain a lot of information concerning the variation in space and time of waves propagating in the analyzed component. Such information can be utilized to evaluate the response spectrum of the wave field in the domain wavenumber/frequency, enabling to separate effectively the incident waves from the reflections produced by possible discontinuities. It turns out to be particularly useful to remove the incident wave from the global response, by using proper filtering strategies, so that the reflections associated to the structural damage can be clearly and neatly observed. This technique has been applied to wavefields generated on both sides of the skin and of the web of the component put under test. A comparative analysis of the recorded results has also been carried out on the two opposite sides of the web, in terms of wave shape and energetic content of the signal- The various analyses shown in the next paragraphs made it possible to highlight the presence of defects attributable to the wrinkling and/or to the porosity on side '1' of the web of the component. Paragraph 3.8, instead, shows the application of the filtering techniques and of techniques of detection of damages maps on a different component, analyzed during a demonstration of use of a Vibrometer 3D by the firm Polytec Gmbh from Waldbronn (Germany).

3.6.1. SKIN EXTERNAL SIDE

The figures below show photograms of the whole wavefield, recorded directly by the SLDV, photograms concerning merely the field of elastic waves,

obtained with the filtering techniques shown in chapter 2 and the RMS maps of the filtering signal. The former ones provide information concerning the energetic levels of the field of reflected waves. The highest RMS values (appearing in red in the fond scale availed in the following pictures) show the position of the points with a higher energy of reflection, providing therefore indications over the area of maximum distortion of the signal recorded by the SLDV. The results shown in the pictures 3.24-26 emphasize how the signal on the external side of the skin is characterized by a reflection of high consistence in the area corresponding to the flange (or web). The signals detected don't show any other distortion or defects of particular relevance.

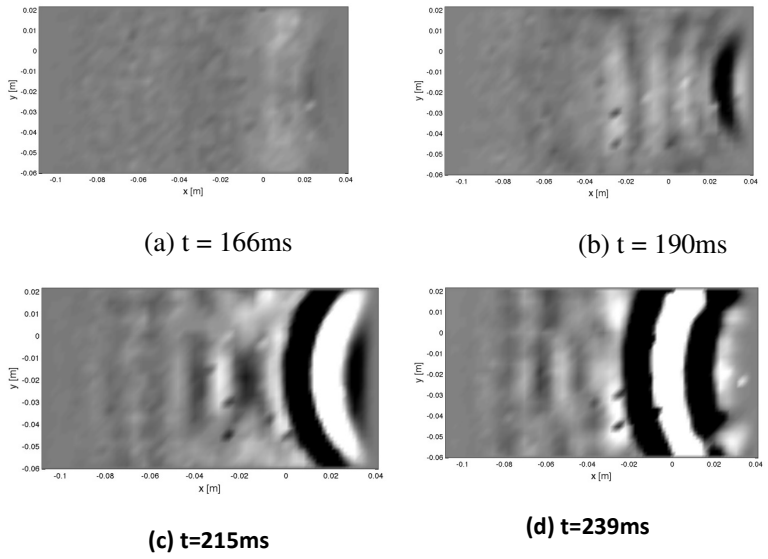

Fig. 3.24 - Photograms of the whole wave field (incident waves plus reflected waves) on the external side of the skin at given time intervals.

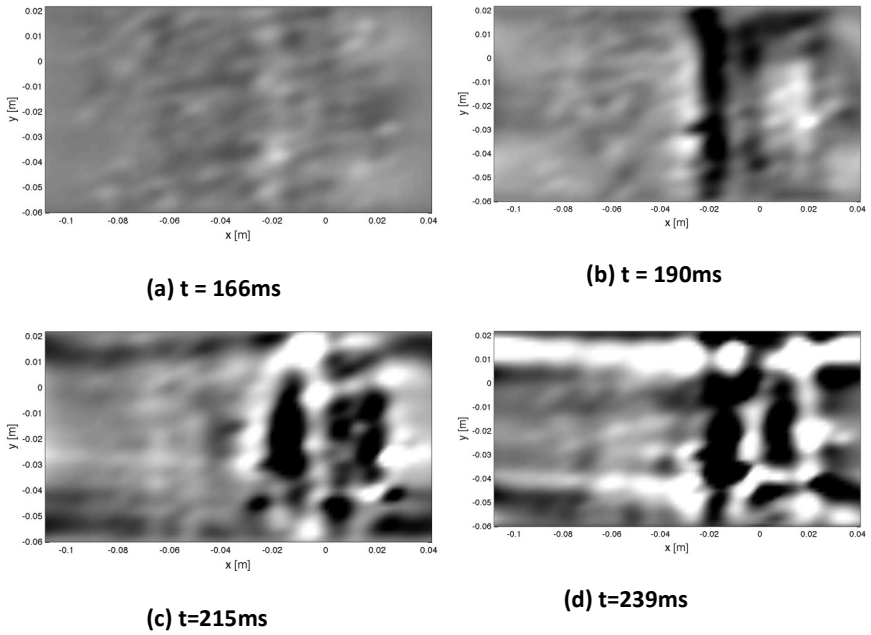

Fig. 3.25 - Photograms of the field of reflected waves on the external side of the skin at given time intervals.

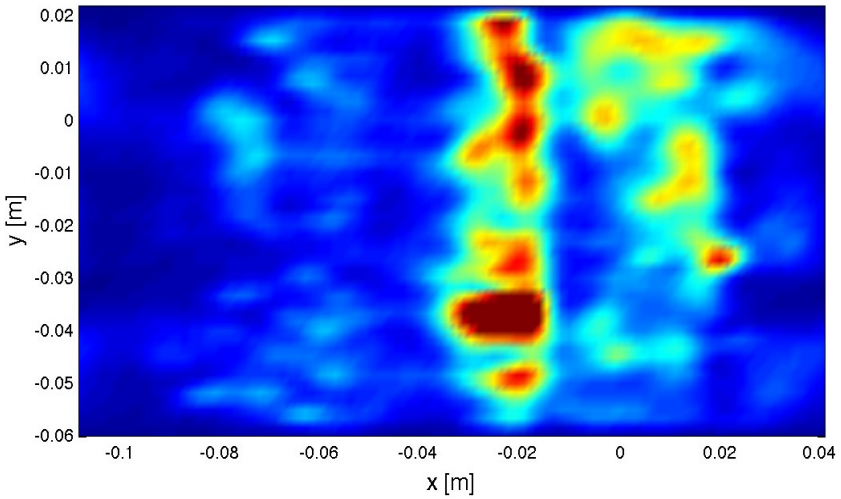

Fig. 3.26 - RMS of the field of reflected waves on the external side of the skin.

3.6.2. SKIN INTERNAL SIDE '1'

Data concerning the internal side '1' of the skin are shown in pictures 3.27-29. In this case, also, as for the external side, there are no indications referring to relevant defects. It is useful to observe, anyhow, that the signals measured on the internal side of the skin are absolutely similar to those measured on the external side. Such observation implies relevant practical consequences, producing the important result that it is possible to excite indifferently the external side or the internal one of the skin, the results remaining the same, depending on how it turns more useful to place the actuators and the sensors during the tests.

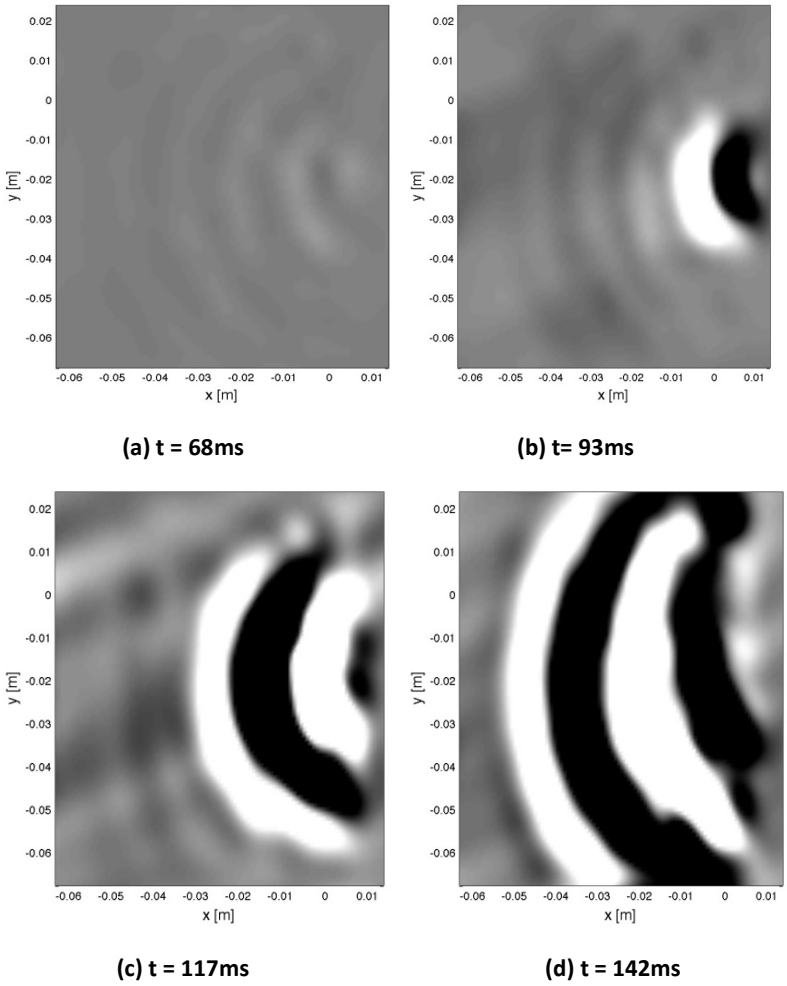

Fig. 3.27 - Photograms of the whole wave field (incident waves plus reflected waves) on the internal side '1' of the skin at given time intervals.

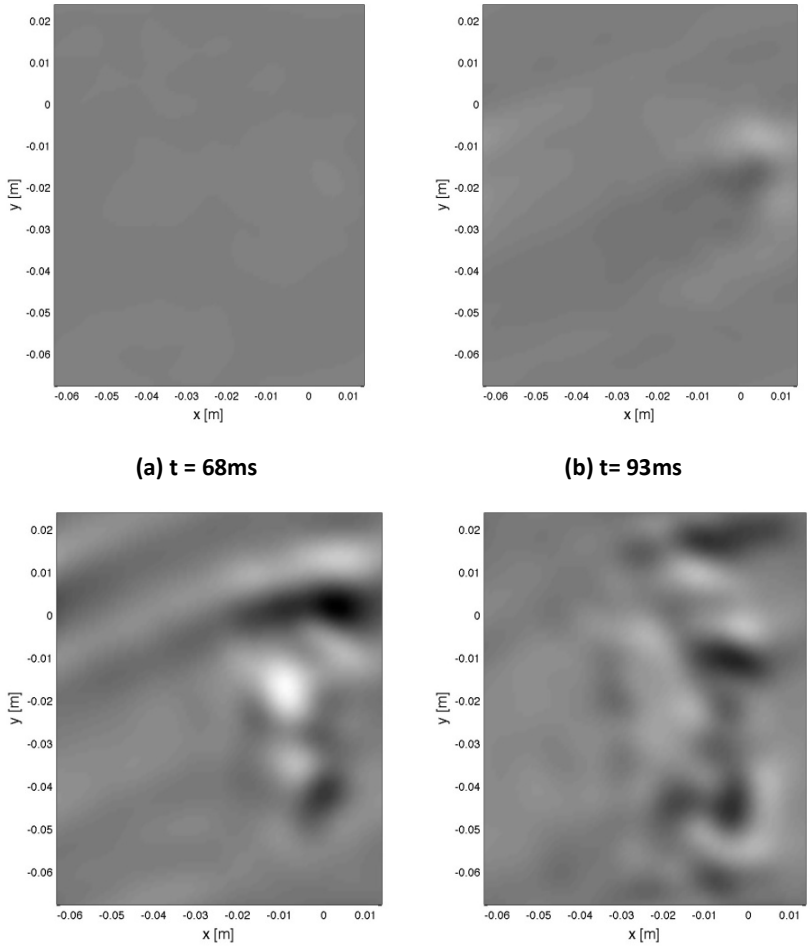

Fig. 3.28 - Photograms of the field of reflected waves on the internal side '1' of the skin at given time intervals.

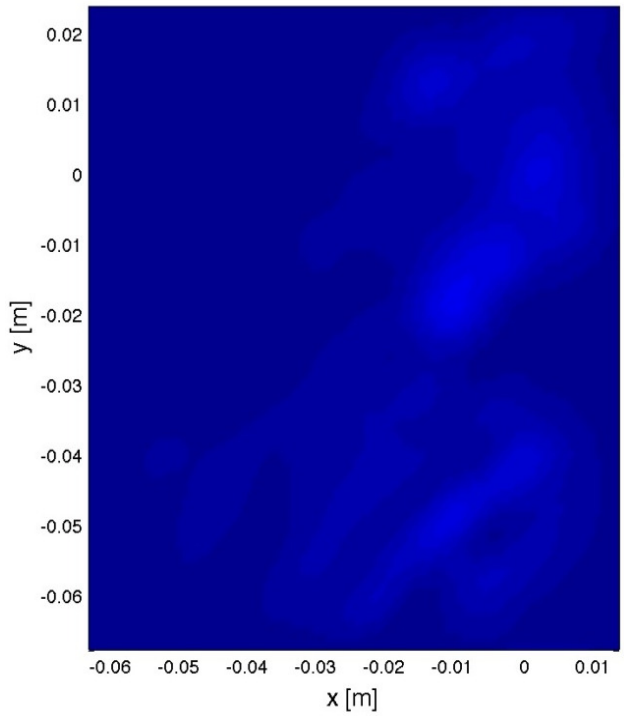

Fig. 3.29 - RMS of the field of reflected waves on the internal side '1' of the skin

3.6.3. SKIN INTERNAL SIDE ‘2’

The results concerning the internal side '2' of the skin are similar to those concerning the internal side '1; see figures 3.30-32.

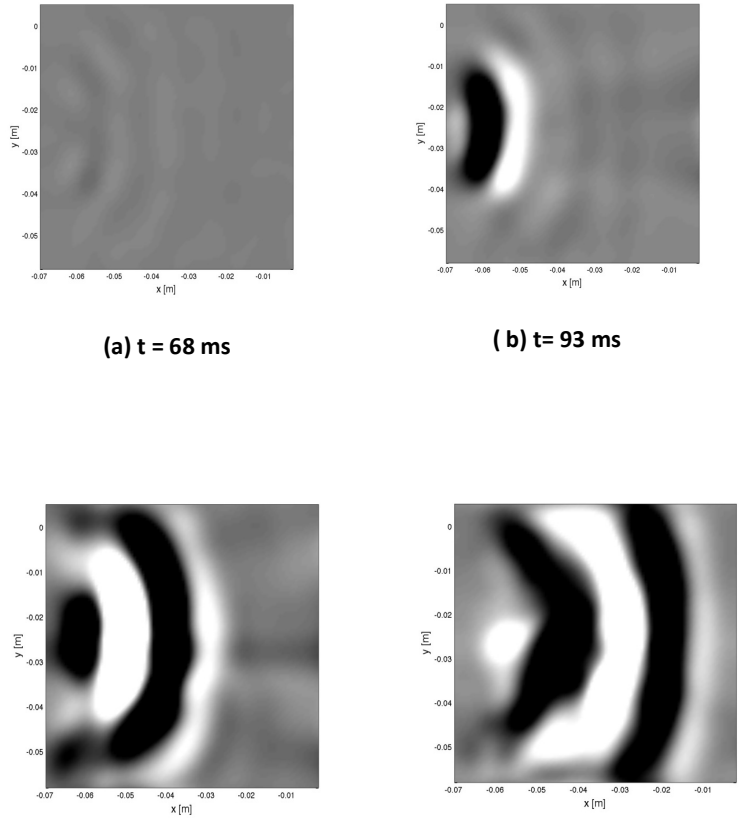

(a) t = 68 ms

(b) t= 93 ms

(c) t = 117ms

(d) t = 142ms

Fig. 3.30 - Photograms of the whole wave field (incident waves plus reflected waves) on the internal side '2' of the skin at given time intervals

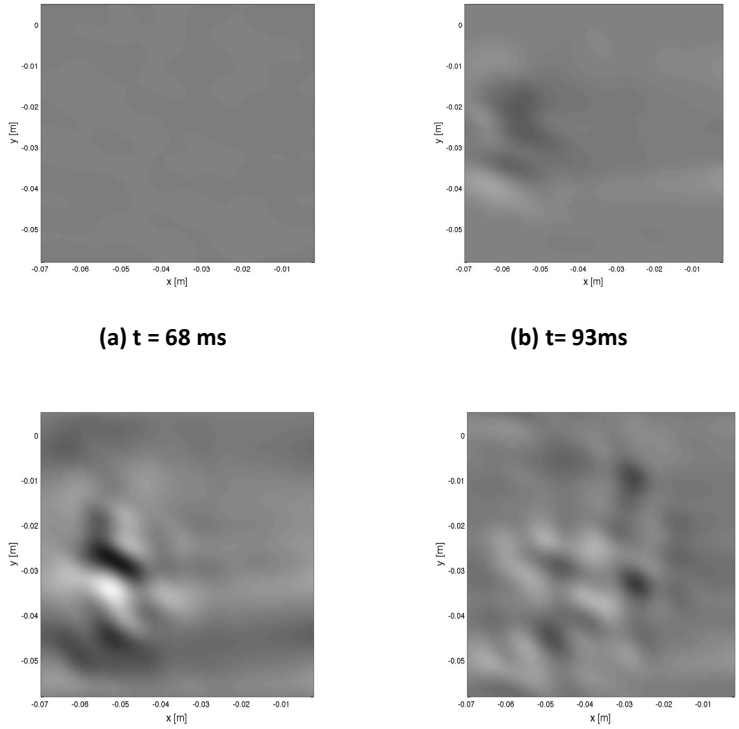

(a) t = 68 ms **(b) t= 93ms**

(c) t = 117ms **(d) t = 142ms**

Fig. 3.31 - Photograms of the field of reflected waves on the internal side '2' of the skin at given time intervals.

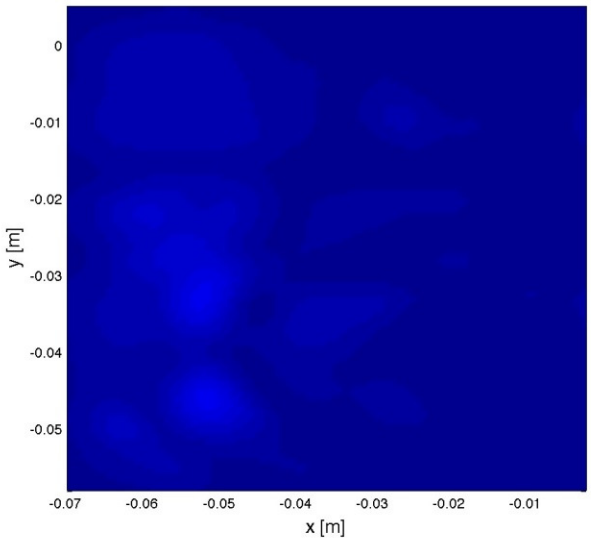

Fig. 3.32 - : RMS of the field of reflected waves on the internal side '2' of the skin.

3.6.4. WEB SIDES ‘1’ E ‘2’

The analysis regarding the two sides '1' and '2' of the web are for sure of greater interest. The results shown in pictures 3.33-38 highlight relevant distortions of the signal recorded on such elements, around the junction zone to the skin. Such distortions are to be attributed, highly probably, to the presence of irregularities in the area of connection or very close to it. The side '1', in particular, shows more evident distortions than side '2'. The latter result is accordant to the visual observation of a stronger wrinkling in the side '1' of the junction skin-web (see figure 3.9). Other possible causes of the distortions of the signal recorded on the web can be attributed to defects of bonding (or porosity) in the zones straight below the junction to the skin.

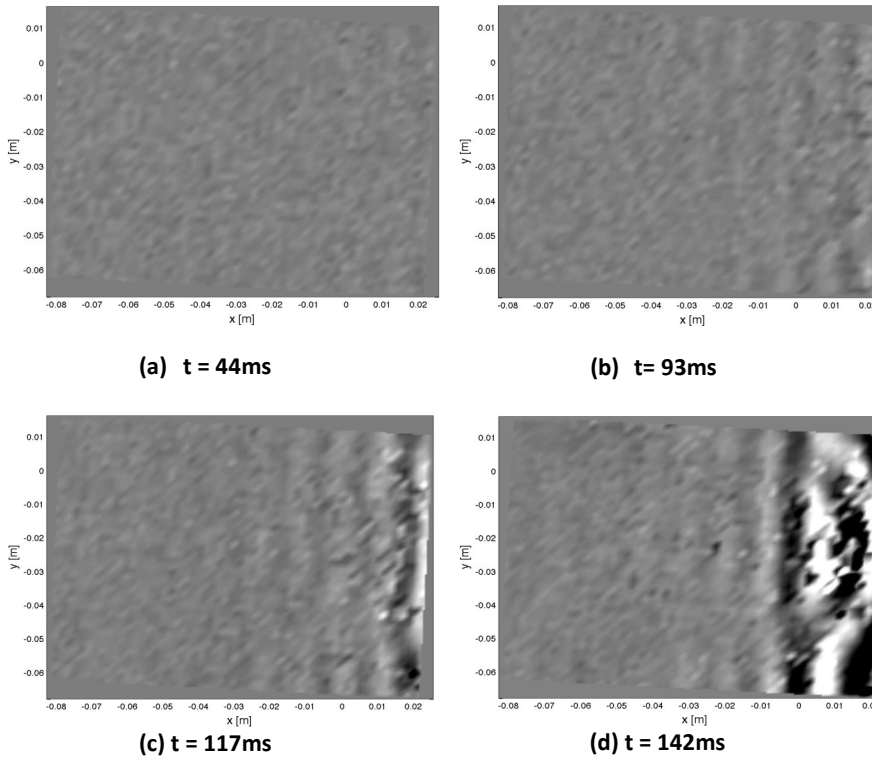

Fig. 3.33 - Photograms of the whole wave field (incident waves plus reflected waves) on the side '1' of the web at given time intervals

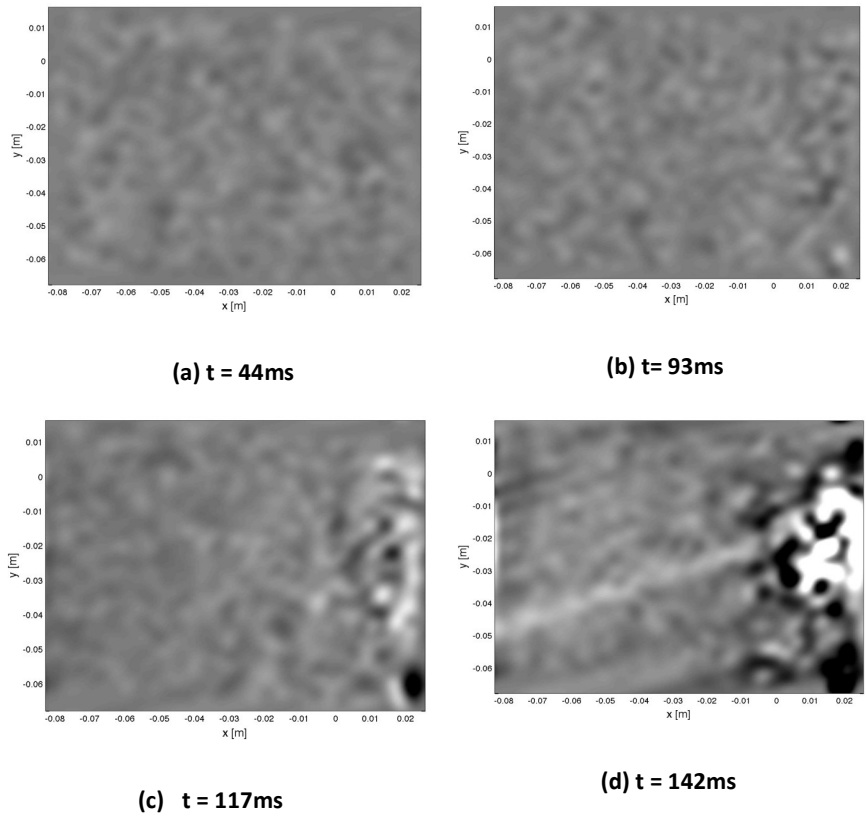

Fig. 3.34 - Photograms of the field of reflected waves on the side '1' of the web at given time intervals

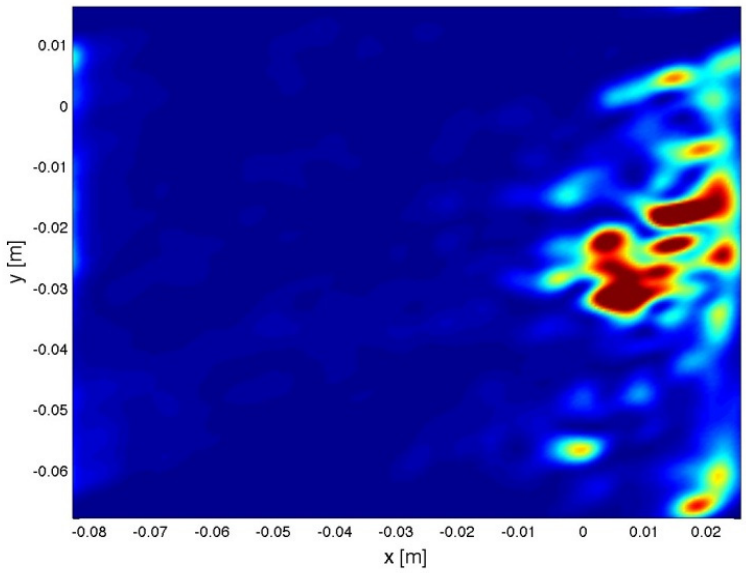

Fig. 3.35 - RMS of the field of waves reflected on side '1' of the web

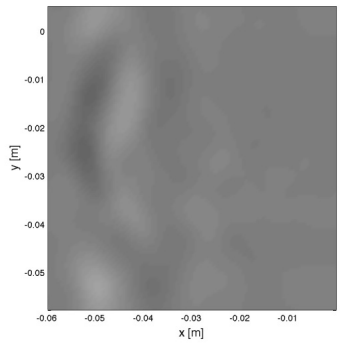

(a) t = 142 ms

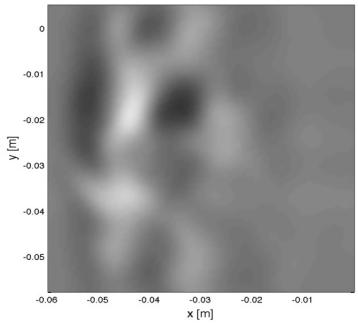

(d) t= 166 ms

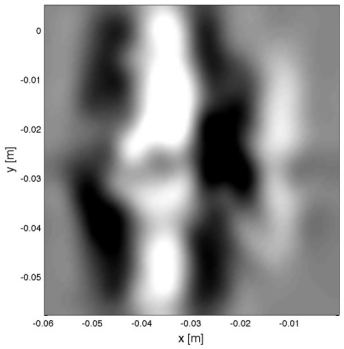

(c) t = 215 ms

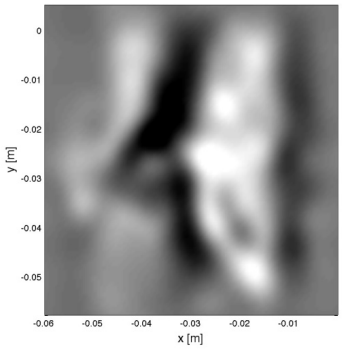

(d) t = 239 ms

Fig. 3.36 - : Photograms of the whole wave field (incident waves plus reflected waves) on the side '2' of the web at given time intervals.

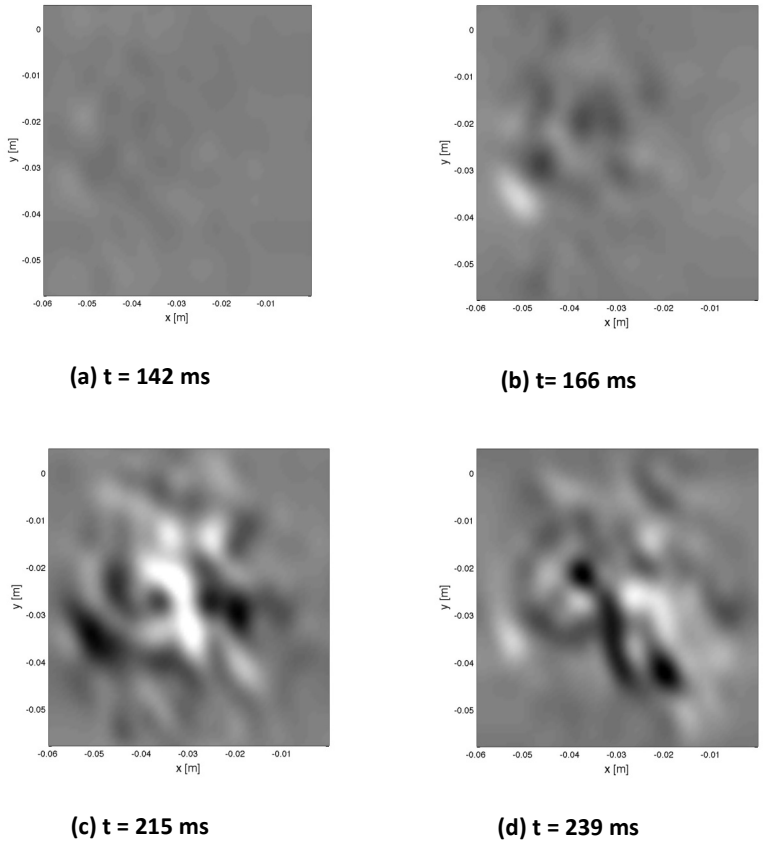

Fig. 3.37 - Photograms of the field of waves reflected on side '2' of the web at given time intervals

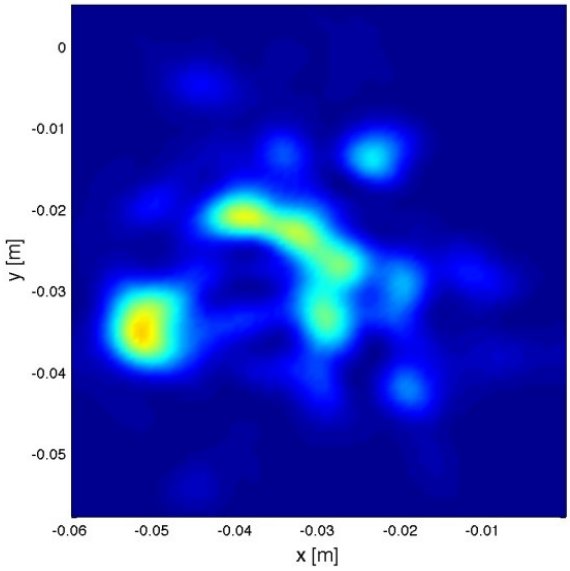

Fig. 3.38 - RMS of the field of waves reflected on side '2' of the web

3.7. COMPARATIVE ANALYSIS OF THE SIGNALS RECORDED ON THE OPPOSITE SIDES OF THE WEB

In this paragraph we will analyze, in a comparative way, the signals recorded using SLDV on the two sides '1' and '2' (also defined as WEB 1 and WEB2, respectively). These elements have been excited by using the piezoelectric actuators indicated as "piezo1" and "piezo2", respectively, in order to analyse possible differences of propagation of the signals generates, due to the presence of wrinkling and/or porosity defects corresponding to the node of junction skin web. Figures 3.39 and 3.40 show the points of the grids availed on the WEB1 and 2, in respect of which a comparison one to one has been carried out of the signals recorded on the two sides. These points are almost symmetrical to the web - skin knot (points 2429, 2343 and 1698 on the WEB1

and points 19, 89 and 614 on the WEB2). In figures 3.39 and 3.40 the analysis grids are overlapped to the RMS maps of the SLDV signals.

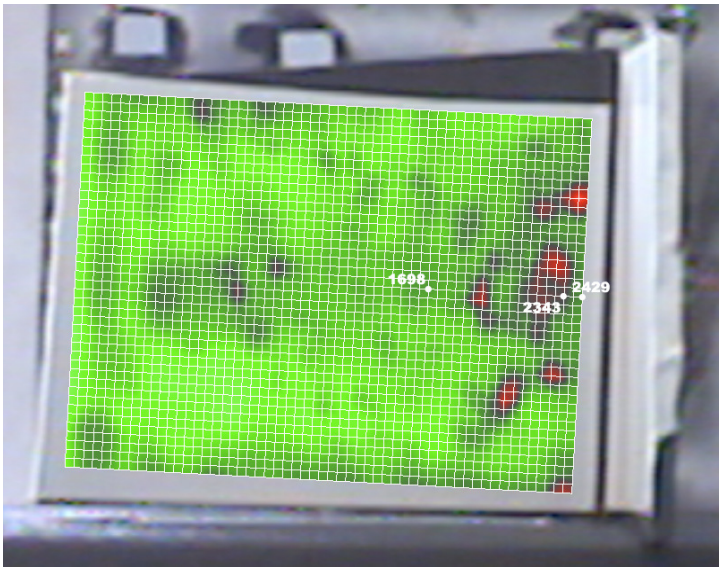

Fig. 3.39 - Analysis grid used on the side 1 of the web (WEB1) overlapped to the RMS map of the whole travelling wave on the same side.

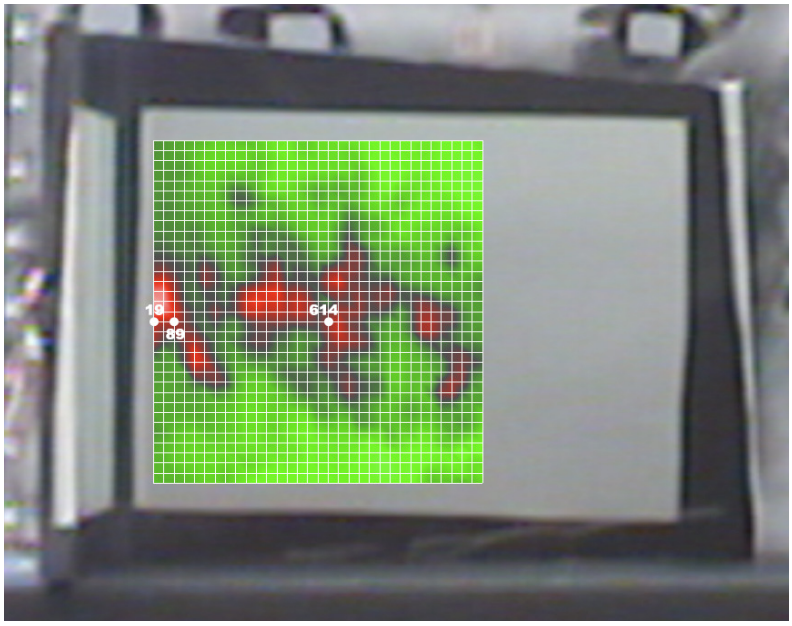

Fig. 3.40 - Analysis grid used on the side 2 of the web (WEB2) overlapped to the RMS map of the whole wave travelling on the same side.

Figure 3.41 compares the profiles velocity [mm/s] -time [s] measured at the points symmetrical on the WEB1 and 2. It is possible to notice that, starting from the radius, the points of top amplitude of the signals recorded on the two WEBS have been transferred (or "shifted") in time, with a time of delay proportional to the velocity of propagation of signals. The subsequent fig. 3.42 shows the Fourier transform ("Fast Fourier Transform" or FFT) of the signals seen in fig. 3.41. For both of the WEB the frequency of analysis varies in range from 0 to 100 kHz, which coincides with the frequency band accessible to the SLDV utilized. In correspondence to the point 2343 of the WEB1, placed in a "red" zone (high intensity) of the RMS map seen in picture 3.39, the FFT shows high energy contents of the travelling signal (see figure. 3.41, left diagram, central plot), which leads to imagine as possible the presence of a defect from wrinkling stronger in correspondence to side 1 of the junction knot skin-web,

than to what is observed on side 2. The RMS map of fig. 3.40 show the presence of "noises" diffused in the signal recorded on the WEB 2.

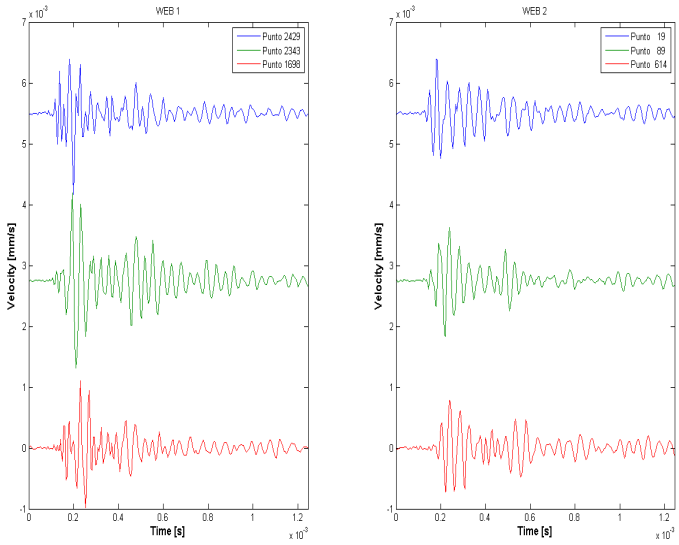

Fig. 3.41 - Diagrams velocity-time in correspondence to symmetrical points of sides 1 and 2 of the web, properly vertically offset.

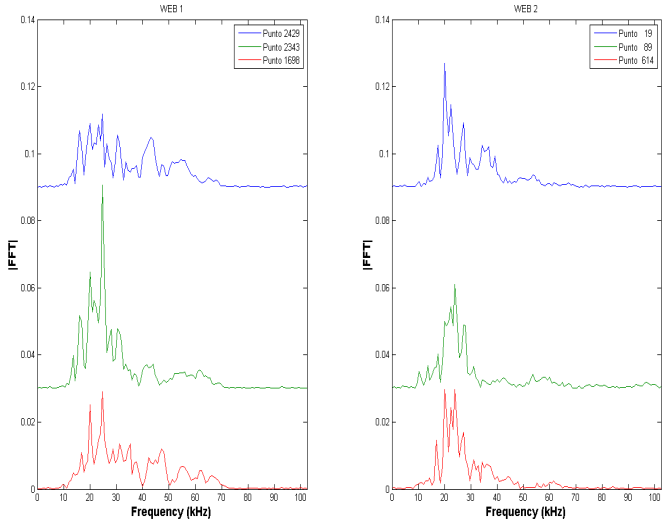

Fig. 3.42 - Fourier transform (FFT) of the signals shown in pic. 3.40, properly vertically offset.

In order to evaluate the variation in space of the energy transported by the signals travelling on the two sides 1 and 2 of the web, specific charts total energy-position have been built in correspondence with the longitudinal guidelines uniting the measuring points shown in figures. 3.39 and 3.40. In these charts, shown in fig. 3.43, the total energy transported by the signal has been identified with the area below the FFT curve relative to the single points here considered, in correspondence to the range of frequencies 10-70 kHz. A comparison between the charts in figure 3.43 and the RMS maps in figures 3.39 and 3.40 shows how the highest contents in energy are reached in correspondence of the red area (high intensity) of the RMS maps on each side of the web. The charts in figure 3.43 show also that the highest energy contents are reached in correspondence to the WEB1 (red coloured chart in pic 3.43), with the highest peak slightly shifted on the left if compared to the point of measure 2343 (see fig. 3.39). The charts in fig. 3.43 show in the abscise the numbers identifying the points of measures analysed by each WEB (they are increasing moving from the left towards the junction point skin-web, placed at the right

extremity of the abscise axe) and on the ordinate the total energy measured as described above. These observations confirm the previous ones as for the presence of an area with a stronger wrinkling in correspondence of the junction zone skin1-web1 and as for the presence of diffused noises of the signal travelling on the side 2 of the web.

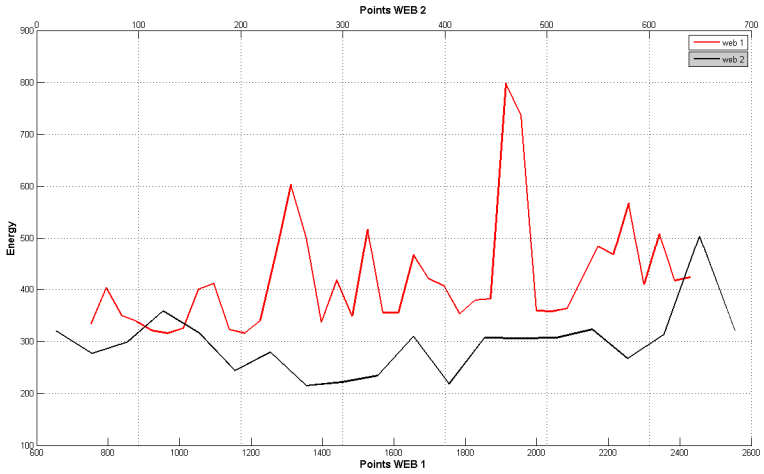

Fig. 3.43- Total energy versus positions graphs (WEB 1 and 2).

3.8. ANALYSIS OF FURTHER POLYTEC DATA

In the present paragraph we will present some analyses of the data provided by the firm PolytecGmbh from Waldbronn (Germany), which have been acquired within a demonstration of use of a scanning Laser Vibrometer3D in the headquarter of Alenia Aeronautica in Pomigliano d'Arco. These tests have been carried out in the month of May 2010. We will report some of the results observed, together with a comparison between the records obtained directly by using the 3D Laser Vibrometer and some elaborations of these data with the "Damage Index" maps described hereafter.

The data presented concern an experiment on a plate with stiffeners containing impact damages, carried out during the demonstration above mentioned. Figure 3.44 shows a general view of the setup employed.

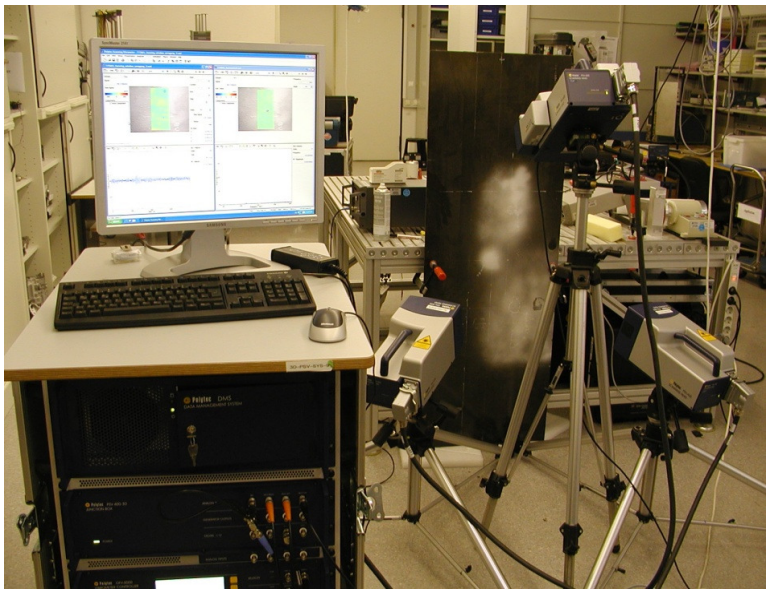

Fig. 3.44 - Polytec test setup.

3.8.1. TEST AND ITEM DESCRIPTION

As a general result, we found that the defects could indeed be located by the lamb wave tests, but that the exciting piezo has to be within max. 0.2- 0.6 m (depending on the sample) of the defect in order to have enough sensitivity for the detection. Small areas can therefore readily be examined, large areas are very time consuming.

With the current equipment, the test of an area of 0.3 x 0.3 m takes about 1-3 hours, depending on the chosen frequency and, thereby, the necessary point density. Higher frequencies lead to better spatial resolution for the localization of the defects, but need a higher grid density. With a stronger excitation source, larger areas could be scanned. This facilitates the search for a defect, as the scan

runs automatically over a larger area. The scan time itself will not be drastically reduced by this, as it depends mainly on the absolute number of points, the averaging count and the waiting time after a pulse for it to die out, which is independent on the scan range. But as the scan is automatic, tests of larger areas could then be performed e.g. at night time. Stiffening ribs and other deviations from a pure plane surface drastically influence the propagation of the wave. Especially for the rather large stiffening ribs of the bigger plate, a good sensitivity for defect detection is only given if excitation and defect are located between the same pair of stiffening ribs. In the following an image of the locations of delamination can be found.

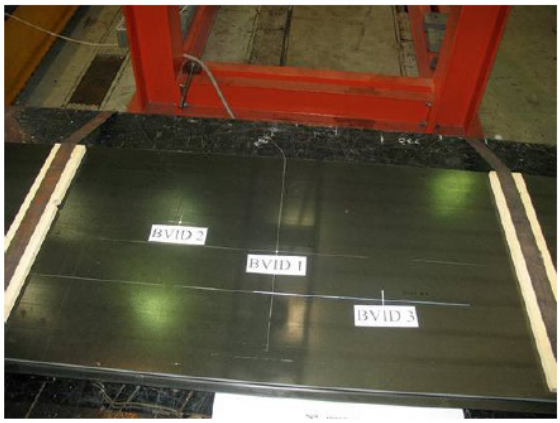

Fig. 3.45 - Impact locations.

Impact		Impact Energy		IMPACTOR (Head DIA 1 Inch)	Measurements	
Type (#)	No.	Lbs-inch	Joule	Weight [Lbs]	Delamination [inch] (X-Y)	Depth [inch]
BVID	1	1200 Cut-off	135.5	146	0.45 – 0.40	0.0045
BVID	2	489.4	55.3	146	1.45 – 1.15	0.0170
BVID	3	929	105	146	4.85 – 2.25	0.0340

Fig. 3.46 - Measurements of the delaminations.

3.9. RESULTS RECORDED BY POLYTEC WITH A 3D VIBROMETER OVER A PLATE WITH DEFECTS

To excite these disks, a special excitation signal has been used, made up of 5 periods of sine of a specific frequency, weighted by a Hanning function to have a smooth spectrum and followed by a long period of zeroes to allow the wave to die out until the arrival of the next wave package. To produce this signal, we had to take the generator of a system equipped by a spectrum card, as the NI 6110, which is used in the PSV 3D, does not allow a sufficiently high data rate. The excitation frequency was chosen as to have on one side a good spatial resolution for defects (high frequencies) and on the other hand a high excitation energy from the Piezo and low attenuation in the material (rather lower frequencies). Depending on the sample and the used type of Piezo a 270 kHz frequency has been used. A typical excitation signal can be seen in the following figures in time and frequency representation.

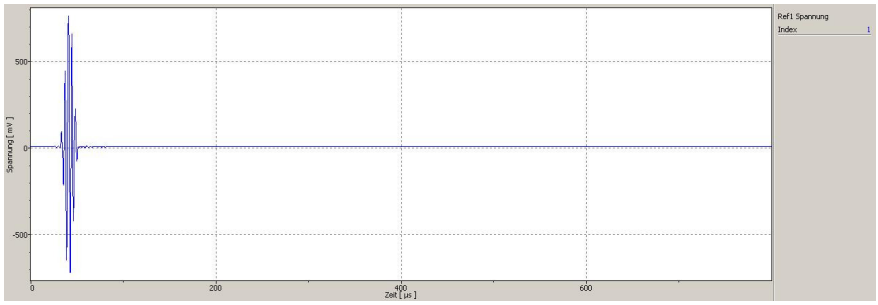

Fig. 3.47 - Excitation signal in time representation.

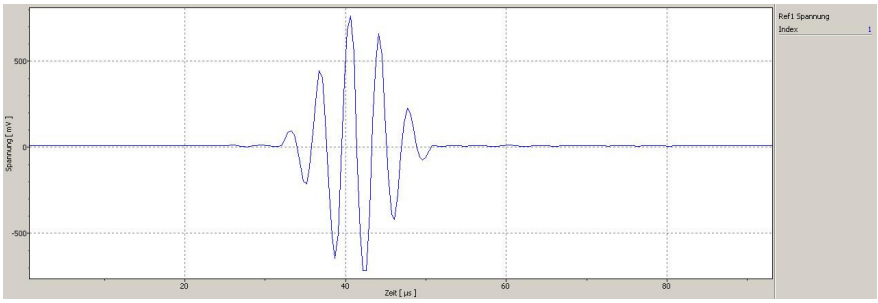

Fig. 3.48 - Zoomed view of the excitation signal in time representation

.

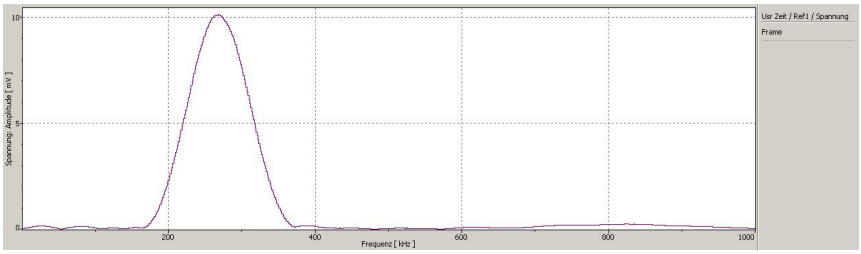

Fig. 3.49 - Excitation signal in spectral representation

To increase the excitation amplitude, a high frequency amplifier has been used. The used voltages are about 70V (0-peak). Band-pass filtering around the centre frequency of the excitation to enhance the signal to noise ratio has been applied. Averaging count was between 50 and 200 averages. The trigger source was an external TTL trigger from the signal generator or an analogical trigger on a monitor signal of the amplifier. The result remains the same for the different trigger signals. Such a plate has some rather thick (at the base about 3 cm) stiffening ribs at the backside. Lamb waves are supposed to be movements of a plate like structure. Its properties depend on the thickness of this plate. Therefore, stiffening ribs considerably influence the propagation of a lamb wave. Due to the large influence of the ribs, we concentrated on a defect which is far from all ribs with plate-like structures around it, which makes the observation of the wave propagation easier. We placed the Piezo between the same pair of ribs as the supposed defect in order to have a nicely propagating wave in the area of the defect.

The results of the Polytec acquisitions here shown are referred to a 270 kHz excitation over the plate seen in figure 3.44. The source of signal used by Polytec is altogether similar to the one employed within the tests analyzed in the previous paragraphs. Velocity fields measured in Z and Y directions, that is, respectively, in direction perpendicular to the plate and in direction parallel to the same plate, in correspondence of two representative time instants, (see Fig. 3.50).

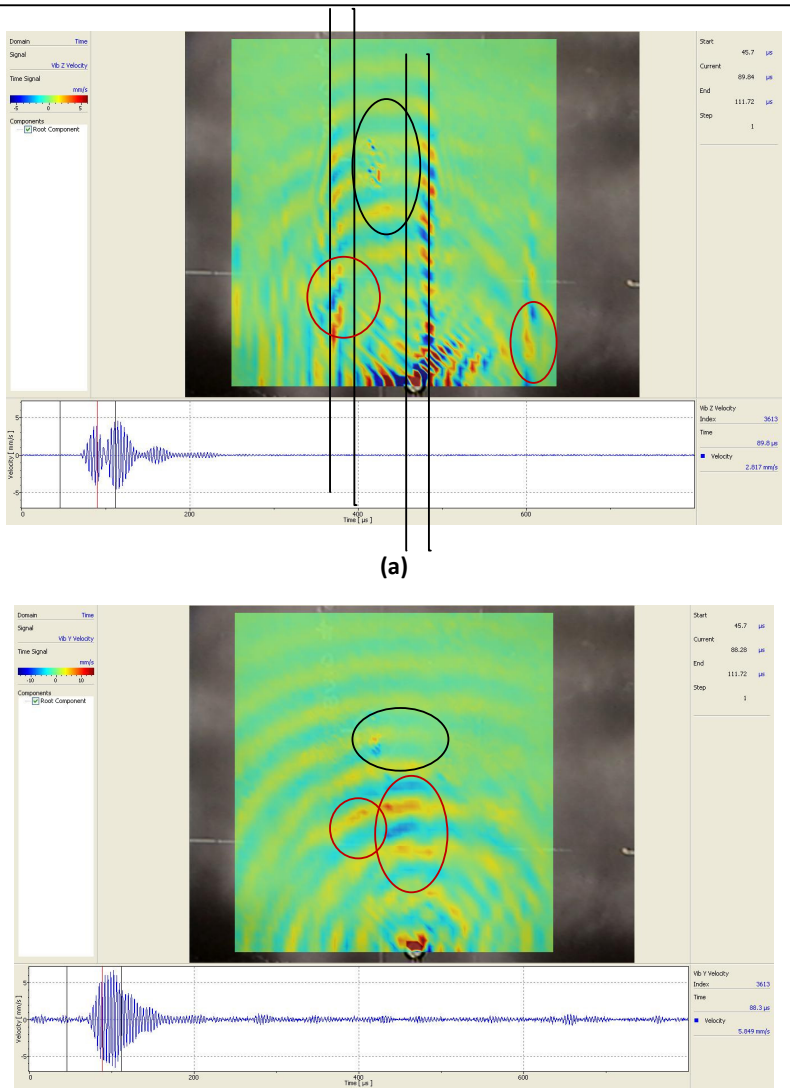

Fig. 3.50 - Response of a stiffened plate at a 270 kHz excitation applied through piezoelectric actuators on the bottom: vibrations in Z (a) directions and vibrations in Y (b) directions. The locations of real damages have been highlighted with black circle, while areas of incorrect damage indications have been highlighted with red ones.

Both of the velocity fields measured show the presence of two impact damages in the area indicates with circles/ovals in black in figure 3.50. The direct analysis, without filtering, of the RMS maps provided by the Vibrometer, though simple and doubtlessly useful, may nonetheless lead to false evidence of damages, or to difficult evaluations for the operator. Indeed, as shown in fig. 3.50, some area of the plate, not damaged (indicated with red circles/ovals) show a response similar to the one of the area really damaged.

3.10. POLYTEC DATA POST-PROCESSING BY MEANS OF PROPAGATION MAPS OF THE REFLECTED WAVES AND DAMAGE MAPS

The present paragraph shows the wave fields detected before and after the filtering procedure, which leads to identify only the reflected waves. The filtered data have subsequently been processed to realize proper damage maps. In order to simplify the perception, only the data concerning the vibration towards Y is analysed, since the analysis of measures towards Z only provides results completely similar to those previously presented. Figure 3.51 shows photograms extracted from the Polytec measure, corresponding to distinct instants of time. These photograms do not provide, obviously, further information in comparison to the data visualized directly by the device (see previous paragraph), but they enable nonetheless to evaluate the interaction between the profile of the wavefield and the damage and they make it possible to express a first visual evaluation over the presence of damages of any kind. Figure 3.51.c, in particular, identifies in detail the interaction between the incident wave and the damage. This picture makes it anyways hard to determine the number of damages present in the area showing the main distorsion of the wave field. A further analysis of the results provided by Polytec, obtained through the described filtering procedure, provides the results shown in figure 3.52. The visual analysis of the filtered data in the two given instants of time enables to conclude reliably as for the presence and the entity of the damages, considering the following reasons:

- it show exactly the reflections caused by the damage and, therefore, it characterizes its position;

- it suggests the possibility of the existence of two localized damages in the zone of reflection;

- it reduces notably the possibility of wrong damage indications, compared to the direct analysis of data provided by the Vibrometer (see circles/ovals in red in fig. 3.50).

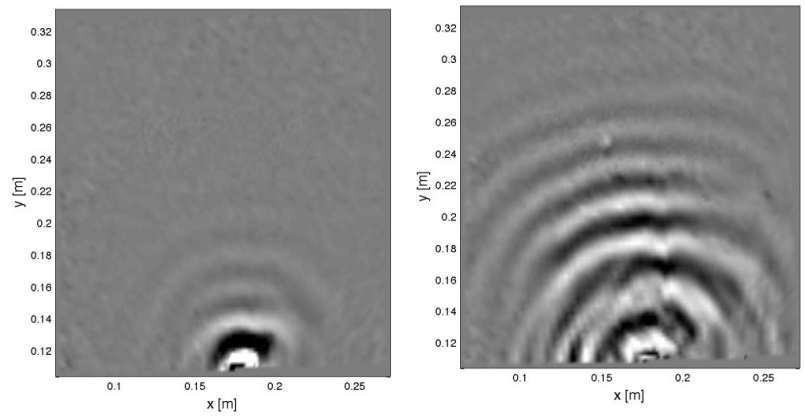

(a) t = 58ms

(b) t = 78ms

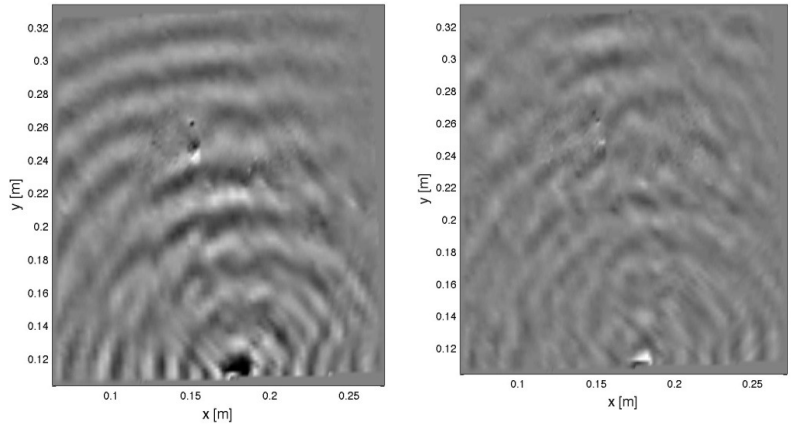

(c) t = 97ms

(d) t = 117ms

Fig. 3.51 - Photograms of the whole wave field (incident wave plus reflected wave) at given time intervals

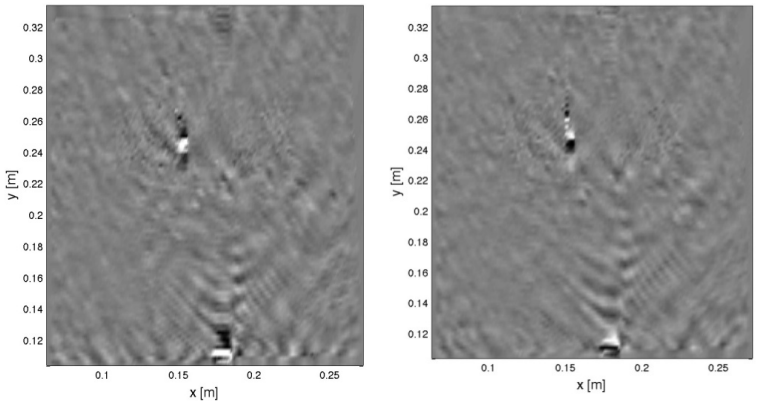

Fig. 3.52 - Photograms of the whole wave field (incident wave plus reflected wave) at given time intervals

The displacement data filtered, obtained trough integration in time of the corresponding speed data, have been subsequently elaborated in order to create a map of a proper scalar index of damage ("Damage Index" or DI), variable in the interval [0,1] (DI=0: absence of damage; DI=1: damage corresponding to a total decay o material, equivalent to the formation of a cavity), which may emphasize furthermore the presence of damages and their position within the area of measure.

The here considered damage index has been obtained through a comparison of deformation measures relative to a large grid and a thin grid centred on the process zone.

The DI map concerning the analyzed data is shown in figure 3.53. Its accurate analysis leads to the following results:

- Exact localization of damages:
- Conclusive identification of the number of damaged sites (two, highlighted by the ovals in figure 3.53);

Complete elimination of unauthentic indications.

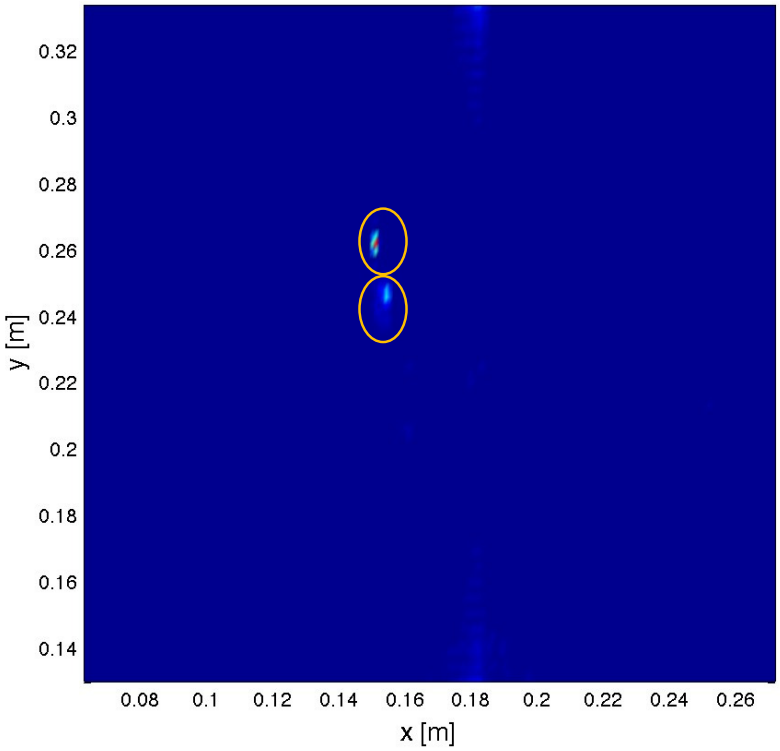

Fig. 3.53 - Damage index map with detailed indication of damaged zones (yellow ovals)

3.11. CONCLUSIONS

The results of the tests carried out over the specimen skin + web show the convenience and the utility of implementing a monitoring system of specimen in composite material, to be based upon the observations of Lamb waves with SLDV. The results of the tests done over this specimen, in particular, allow asserting the following conclusion:

1. The Lamb waves (or guided waves) propagate along structural skin-web junctions and are, therefore, adequate for the study of characteristics of the wave propagation in correspondence of such junctions and for the local identification of possible defects or damages.
2. Measures over the skin may be taken indifferently both with excitation on the internal side and with excitation on the external side, which confers a huge flexibility to the investigating techniques of guided waves, ahead of their practical implementation.
3. The presented results provide indications of anomalies and or distortion around the junction skin - web of the tested component, which can be attributed to the local presence of wrinkling and or porosity.
4. The above mentioned anomalies can be visualized effectively and precisely by means of proper filtering of the SLDV signal in domain of wave number/frequency.
5. The main distortions of the signal have been observed in the zone characterized by stronger wrinkling (side 1 of the junction skin-web).
6. Such indications are confirmed by a comparative analysis of the signals measured on the opposite sides of the skin.

As for the techniques of post-processing of the data recorded with the 3D laser vibrometer by Polytec over a stiffened plate with punctiform defects, we can conclude that such techniques lead to the following results:

1. Clear indication of the areas with high reflection and relative damage localization.

2. Elimination of spurious signals, which may be source of false indications of damage.

3. Exact indication of the number of damaged sites, even in case some of them are localized in positions close one to the other.

4. FINITE ELEMENT MODELING OF WAVE PROPAGATION IN ANISOTROPIC STRENGTHENED PLATES

The motivation that inspired this work lies in the possibility to utilize a flexible instrument, such as the Finite Elements (FE), to model a powerful damage identification tool, like the guided waves. A numerical model, that can predict the exact propagation of waves in material, could lead to the implementation of SHM systems able to monitor the presence of defects in the structure, their positions and dimensions. The main objective of this chapter is to verify the correctness of the wave propagation modeled with the FE. This is no trivial task because of the complex nature of wave propagation in plates, especially for the composite materials case. The first step in the present work consists of creating a model using Finite Elements (FE) that can represent how the waves move into a plate strengthened. This is no simple task because the phenomenon involved is very fast, the spatial scale is small and the results in literature are few and relative only to simple composite plates, with no stiffeners. The first FE model created is made of shell elements, while the second is made of solid elements. Both reproduce the behavior of the waves in the composite stiffened plate experimentally tested in the previous chapter. The sequence of lamination, the number of plies, the material adopted for this anisotropic plate was selected basing on the characteristics of the panels that have been produced at Alenia Pomigliano plant in order to carry out experimental measurements. All the numerical analyses were carried out by the finite element software MDNastran, whose details are defined in the first section of this chapter. For this kind of simulation, it is necessary to use an Explicit Dynamic solution (Sol 700 for MDNastran). As just said, we performed numerical analysis on the plate with stiffening ribs, which was scanned by means of SLDV 3D. There are impact damages (we suppose that BVID stands for barely visible impact damage) on it. As for the experimental test, we focused on the one which is not in the immediate vicinity of a stiffening rib. So we made a cut of the total model with five stiffeners, considering a portion of the model exactly reproducing the

very fine grid coming from the laser output [200X200 grid points on the skin side]. This resulted in a very computationally expensive numerical calculation.

4.1. OVERVIEW OF EXPLICIT DYNAMIC ANALYSIS FOR MDNASTRAN SOL700

A detailed theory of explicit analysis is outside the scope of this section. However, it is important to understand the basics of the solution technique (MD Nastran, SOL 700).

The equation of motion

$$Ma_n + Cv_n + Kd_n = F_n^{ext} \tag{4.1}$$

can be rewritten as

$$Ma_n = F_n^{ext} - F_n^{\text{int}} \tag{4.2}$$

$$a_n = M^{-1} F_n^{residual} \tag{4.3}$$

where

F_n^{ext} = vector of externally applied loads

F_n^{int} = vector of internal loads (e.g., forces generated by the elements)

$$F_n^{\text{int}} = Cv_n + Kd_n \tag{4.4}$$

M = mass matrix.

The acceleration can be found by inverting the mass matrix and multiplying it by the residual load vector. In SOL 700, like any explicit finite element code, the mass matrix is lumped which results in a diagonal mass matrix. Since M is diagonal, its inversion is trivial, and the matrix equation is a set of independent equations for each degree of freedom, as follows:

$$a_{ni} = F_{ni}^{residual} \Big/ M_i \tag{4.5}$$

The Leap-frog scheme is used to advance in time. The position, forces, and accelerations are defined at time level, while the velocities are defined at time level $n + 1/2$. Graphically, this can be depicted as:

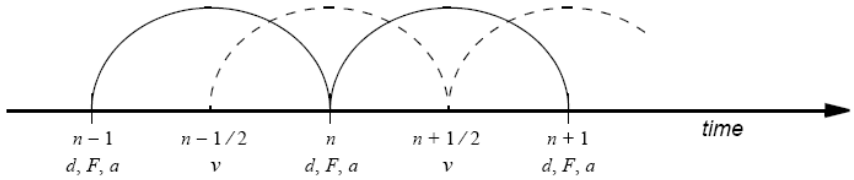

Fig. 4.1 - Explicit scheme

$$v_{n+1/2} = v_{n-1/2} + \frac{a_n\left(\Delta t_{n+1/2} + \Delta t_{n-1/2}\right)}{2} \tag{4.6}$$

$$d_{n+1} = d_n + v_{n+1/2}\Delta t_{n+1/2} \tag{4.7}$$

The Leap-frog scheme results in a central difference approximation for the acceleration and is second-order accurate in Δt . Explicit methods with a lumped mass matrix do not require matrix decompositions or matrix solutions. Instead, the loop is carried out for each time step as shown in the following diagram:

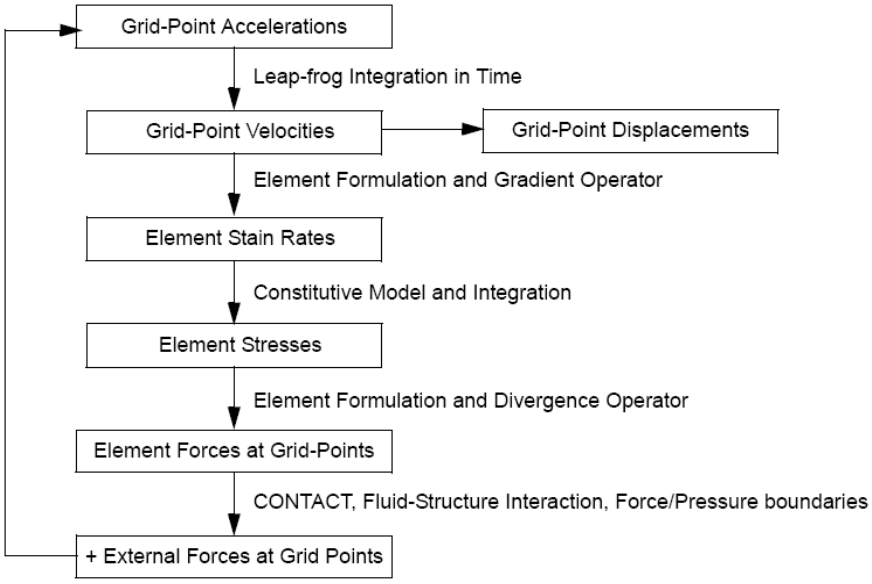

Fig. 4.2 - Explicit scheme diagram

Implicit methods can be made unconditionally stable regardless of the size of the time step. However, for explicit codes to remain stable, the time step must subdivide the shortest natural period in the mesh. This means that the time step must be less than the time taken for a stress wave to cross the smallest element in the mesh. Typically, explicit time steps are 100 to 1000 times smaller than those used with implicit codes. However, since each iteration does not involve the costly formulation and decomposition of matrices, explicit techniques are very competitive with implicit methods. Since the smallest element in an explicit solution determines the time step, it is extremely important to avoid very small elements in the mesh. Since it is impossible to do a complete eigenvalue analysis

every cycle to calculate the time step, an approximate method, known as the Courant Criterion, is used. This is based on the minimum time which is required for a stress wave to cross each element:

$$\Delta t = SL/c$$

where:

L = Smallest element dimension

c = Speed of sound in the element material.

For 1-D elements, the speed of sound is defined as:

$$c = \sqrt{E/\rho}$$

where:

E = Young's modulus

ρ = density

The time step for implicit solutions can be much larger than is possible for explicit solutions. This makes implicit methods more attractive for transient events that occur over a long time period and are dominated by low frequency structural dynamics. Explicit solutions are better for short, transient events where the effects of stress waves are important, as in our case. Explicit solutions have a greater advantage over implicit solutions if the time step of the implicit solution has to be small.

4.2. GEOMETRY OF MODEL

The first step to have the panel appropriately modeled consists of the definition of geometry. Dimensional parameters have been taken by technical design of the item, as shown in the table below.

Design parameters

Skin and stringers length	1524	mm	59.436	inches
Skin width	524	mm	20.436	inches
Cap bonded width	54.8	mm	2.1372	inches
Cap free width	40	mm	1.56	inches
Web height	60	mm	2.34	inches

Table 1– Design parameters

Data are expressed in both SI and UK / U.S.A. system. The two figures below show technical design of the item. All data are expressed in SI.

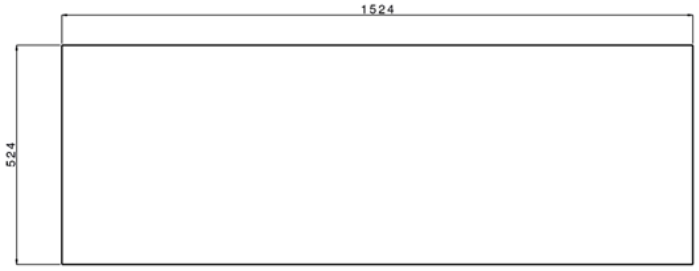

Fig. 4.3 - Skin geometry

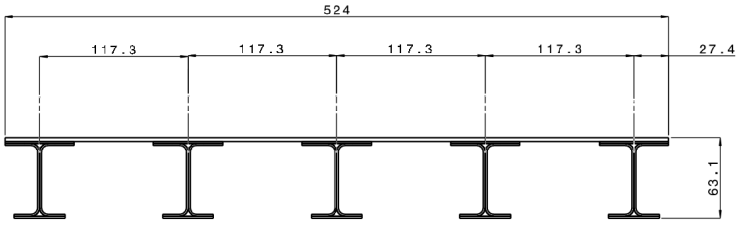

Fig. 4.4 - Item profile including skin and stringers

In figures below geometry defined in Patran environment is shown.

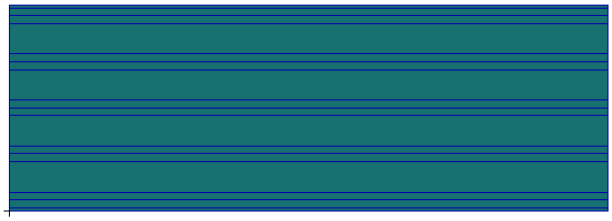

Fig. 4.5 - Panel geometry (view from above)

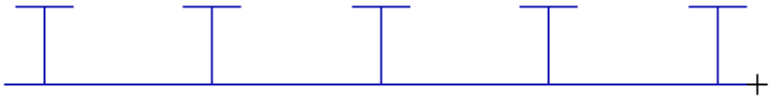

Fig. 4.6 - Panel geometry (frontal view)

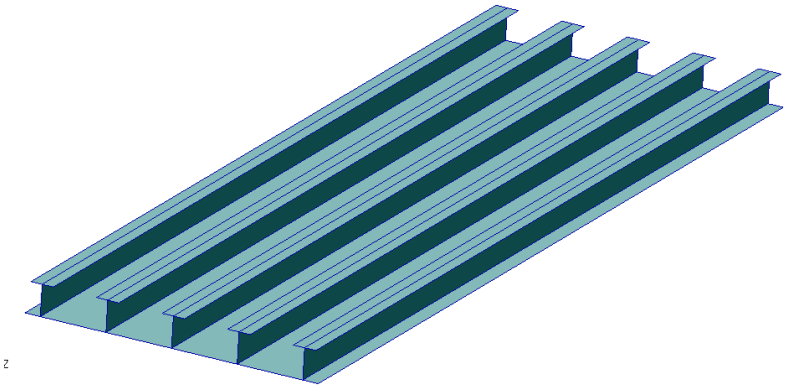

Fig. 4.7 - Panel geometry (lateral view)

4.3. MODELING OF THE EXAMINED PLATE BY SHELL ELEMENTS

Our first numerical analysis involved quadrilateral shaped elements with four nodes (which define isoparametric membrane-bending or plane strain quadrilateral plate elements), whose dimensions are equal to 0.05in x 0.05 in^2. This kind of meshing is quite heavy for MDNastran solver, but allows a wave propagation simulation very close to the real wave propagation coming from the laser output. The visualized wave is the one corresponding to the antisymmetric mode, A_0.This modeling technique cannot represent correctly the symmetric mode, S_0, because such representation requires capturing the expansion/contraction effects which are due to the presence of Poisson moduli ν_{13}, ν_{31}, ν_{32}, which link the in-plane displacements with the out-of-plane ones. The CQUAD4 elements have the shear moduli G_{13} and G_{23} , but they don't

have the Young's modulus in the direction normal to the plate E_{33} (2D Orthotropic behavior), which could transmit an anti-symmetric out-of-plane displacement or extension of the thickness; this phenomenon should be coupled with the in-plane extension or compression of the laminae. Such coupling is fundamental to correctly reproduce the symmetric mode, S_0, and it can be reached with solid elements and 3D orthotropic behavior. It is important to highlight that the delamination (which acts as a discontinuity in the material) causes a distortion of the wavefront, so it is immediate to localize the defect. The FE model of the strenghtned plate is created using Patran environment, the modeling software in the MSC suite of programs. As just said, shell elements chosen for the first simulation, unfortunately, cannot model the symmetric mode, because of the contemporaneous extension or compression of both sides of the plate. Moreover a more detailed propagation of the wave through the thickness could be achieved with solid elements (our second FE simulation). As in the lab tests, only a reduced part of model is necessary. Then, to avoid useless heaviness of run, a cut-off has been performed on model. Only the part where piezo actuators are installed has been selected. As shown in figure below only central stringers remain in the model.

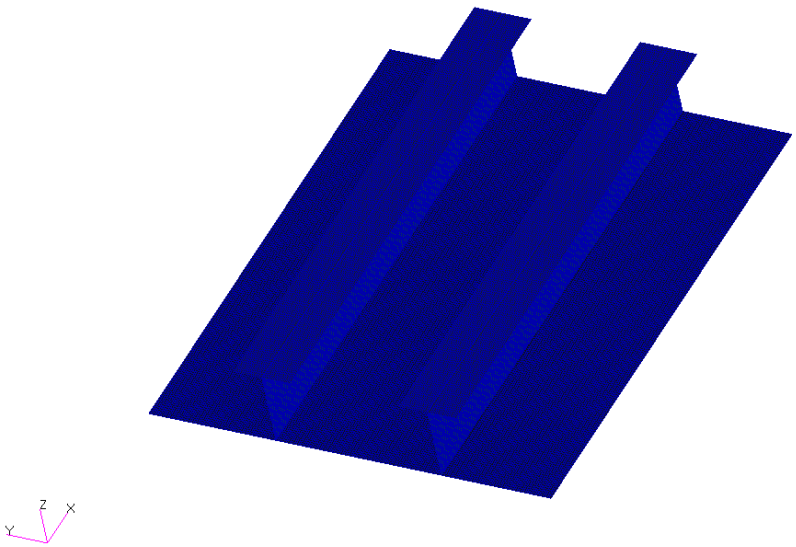

Fig. 4.8 - Cut-off of the total panel meshed

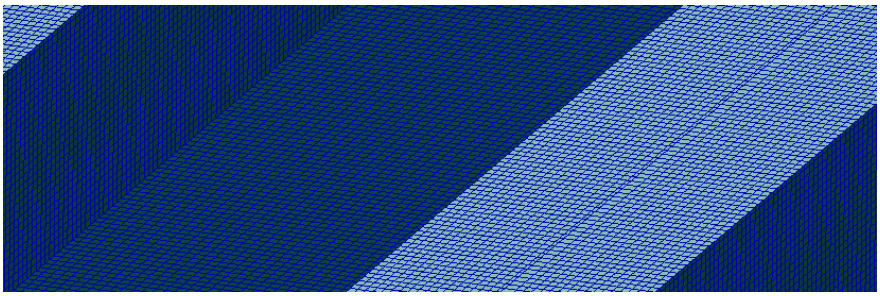

Fig. 4.9 - Enhancement of meshing.

Orientation: The plate is positioned in the x-y plane, so the z axis is normal to the plate. The same scenario applies for the solid element model.

Element type: The elements adopted to model the plate are the ones called CQUAD4 by Nastran. This abbreviation denotes a shell element, defined by four nodes. The mesh for wave propagation analysis should be the most regular as possible to avoid spurious dispersions and reflections. For this reason the plate is modeled by a structured mesh and, to further increase the regularity, elements square in plan are adopted.

Element size: Element size has a great importance in wave propagation analysis because it affects the minimum wavelength that can be represented in the analyses. Accordingly, the element size along the direction of propagation must be small enough to catch the shortest wavelength produced. Considering the tests described in the paragraph 3.4, the wavenumber corresponding to the highest amplitude is more or less equal to k=150-200 rad/m, which corresponds to: $\lambda \equiv \frac{2\pi}{\kappa} = 1.2in$. Moreover the number of nodes per wavelength should be at least 6, to get a good representation of the wave, so we chose an element size equal to 0.05 in, to have 6 nodes per wavelength. The same scenario applies for the F.E.M. model with solid elements.

Time step: The central-difference integration scheme is conditionally stable, so the time increments, also called time steps, must be shorter than a determined value in order to get convergence. The value of Δt is given by Eq.4.8,

$$\Delta t \leq \frac{L_{\min}}{c_L} \tag{4.8}$$

where c_L, given by Eq.4.9,

$$c_L = \sqrt{\frac{E(1-\nu)}{\rho(1+\nu)(1-2\nu)}} \tag{4.9}$$

is the longitudinal or dilatational wave speed. The maximum time steps are calculated using Eq.4.8, for our laminate is 1.96e-6 s.

4.4. LOADS AND CONSTRAINTS

For a wave propagation analysis the plate is free. There are no constraints of any kind, because Lamb wave propagates in plate with free boundaries. Constraints are not necessary to perform a dynamic analysis with high frequency and low intensity load. However, it is worth noting that the fully constrained boundary condition is in accordance with the experimental set up of chapter 3. The application of a load normal to the plate can be used to simulate the effect on an excitation by means of piezoelectric actuators (PZT). The load can be applied just on one side of the plate, exciting both the symmetric S_0 and anti-symmetric A_0 modes of Lamb wave. Applying the force on both sides of the plate can be used to produce either pure shear or pure bending, respectively, if the forces have the same or different directions. Therefore the symmetric and anti-symmetric modes of Lamb waves can be generated separately, as can be seen in Fig.4.10; such an approach, based on two separated excitation sources, is mainly used in FE models rather than in lab, because of technical difficulties in positioning the two actuators perfectly, in checking that the force generated is the same and in synchronizing them properly.

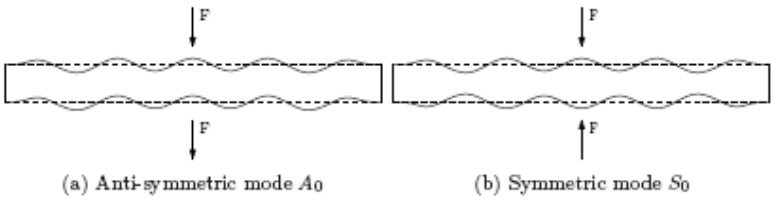

Fig. 4.10 - Pure modes by excitation of the plate on both sides

In the model the load is applied in the bottom of the plate and just on one side (as in the test). Another important parameter is the frequency of excitation, because the behaviour of the Lamb wave significantly changes with the frequency. The 5.5 cycles sinusoid signal is modulated by the Hanning window to reduce the leakage, as reported in literature [30, 31]. The excitation signal in time and frequency domain is shown in Fig.4.11. The signal is defined in tabular

mode, as a series of 500 coordinates of time and amplitude. The value of the force, assumed to be 1 N, is multiplied by the amplitude to get the input signal.

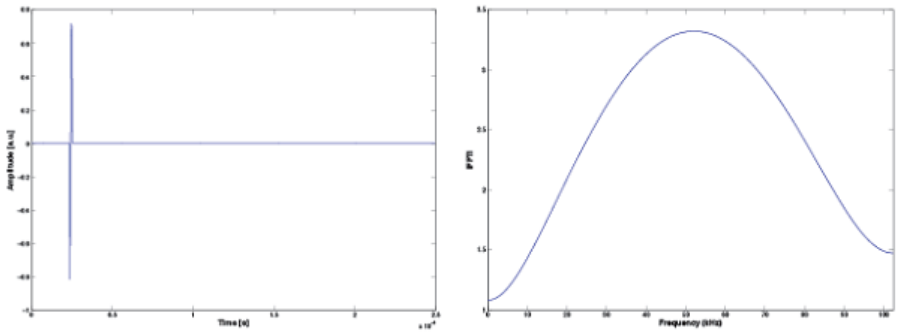

Fig. 4.11 - Input excitation signal in time and frequency domain, 5.5 cycles at 270 kHz

The force is applied normally to the plate and it is distributed over 3 nodes around the point of application to represent better a finite dimension source of excitation, like a PZT and to reduce the local effects of a concentrated load in a FE model. To simulate piezo loading, a cylindrical coordinates system has been created in the zone where piezo has been physically glued on the panel. Z-axis of coordinates system is normal to skin model surface. Then, a both time and spatial dependent load has been created. Time dependency follows equation rules already studied in chapter 3. Spatially load has a constant intensity and in oriented along radial direction on cylindrical coordinates system. In this manner, concentric waves will propagate on model. Such a load has been applied to those elements corresponding to physical application of piezo actuator. The same scenario is applied to the solid element model.

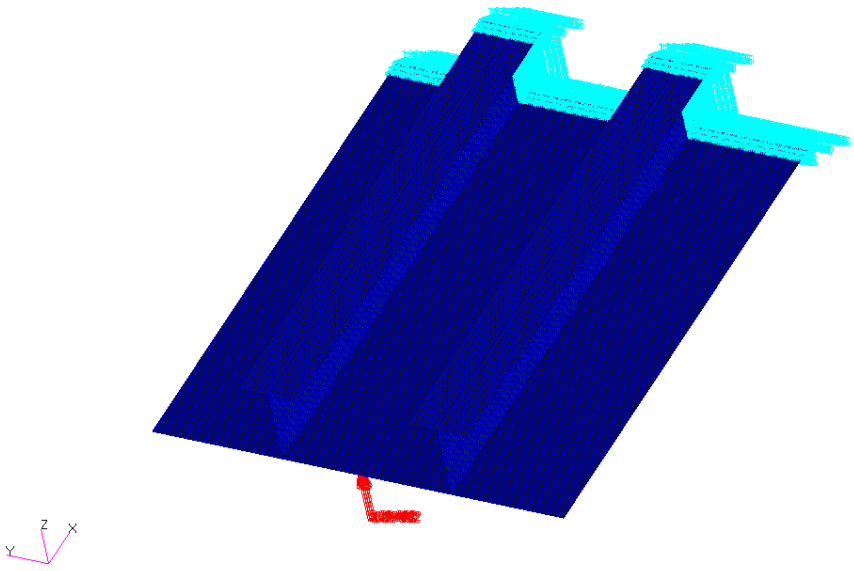

Fig. 4.12 - Loads and constrains on the model

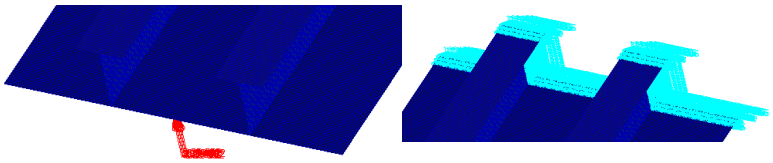

Fig. 4.13 - Details of previous image

4.5. MATERIAL PROPERTIES AND LAY-UP

The material adopted for the plies consists of unidirectional laminae made of carbon and glass fibers both in epoxy resin. Each lamina has an orthotropic behavior whose characteristics cannot be reported (Alenia Confidential). In the following figure, the property scalar plot is reported; delamination, whose location has been highlighted with a black circle, has been simulated with reduced properties.

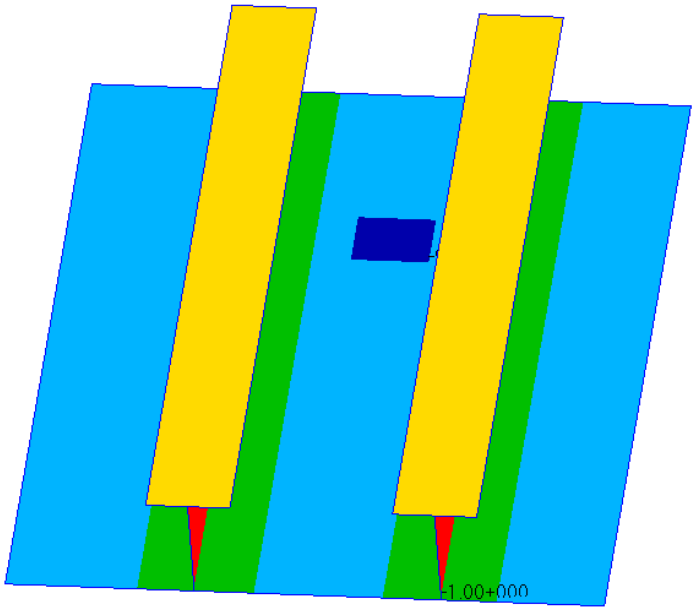

Fig. 4.14 - Property set name scalar plot

Composite properties, whose detail are Alenia Confidential, have been applied to model quads, simulating real mechanical features of the material. The material used for this first model is 2D orthotropic.

4.6. WAVE PROPAGATION IN F.E. MODEL WITH SHELL ELEMENTS

The analysis performed is dynamic explicit non-linear (MDNastran, SOL 700). In this section the results of wave propagation analyses are reported. The information obtained from the analysis of the FE model is, among the others, the time histories of the velocities of the nodes over the plate (as in the acquiring of the laser vibrometry). These histories are the values that the velocities of the nodes assume during the observation time. Each node of the plate can have more time histories, one for each degree of freedom of interest. The degree of freedom that reproduces the wavefront propagation is the in-plane velocity V_1, while the out of plane velocity V_3 cannot reproduce in time the wave behavior, because there are no elements in the thickness direction. The reported results are the field output representation of the in-plane velocities V_1 in four time instants, to represent the shape of the wavefront and its evolution. The visualized wave is the one corresponding to the antisymmetric mode. The results are displayed in Fig.4.15. As it can be seen, there is the desired match with the experimental results, inhering the waveform is fully represented. The results coming from F.E.M are very close to the one extracted from the Matlab environment corresponding to the real velocity value at each node of the user-defined grid in Fig.4.19. Please note the wave's distortion due to the presence of delamination (third figure).

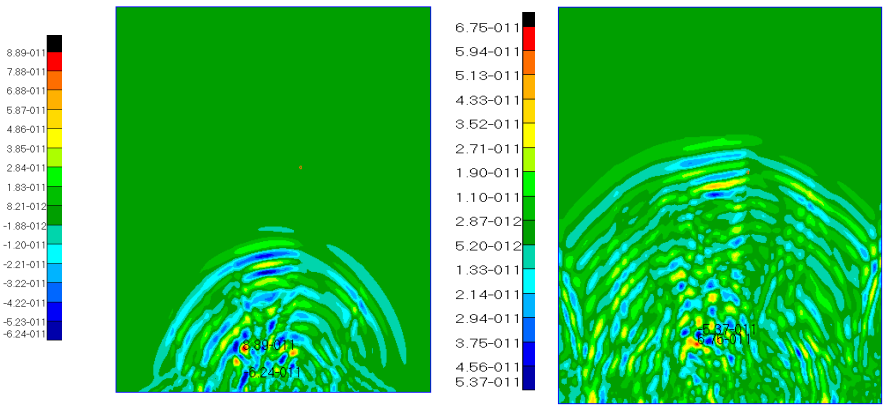

t=0.0428848ms t=0.071266ms

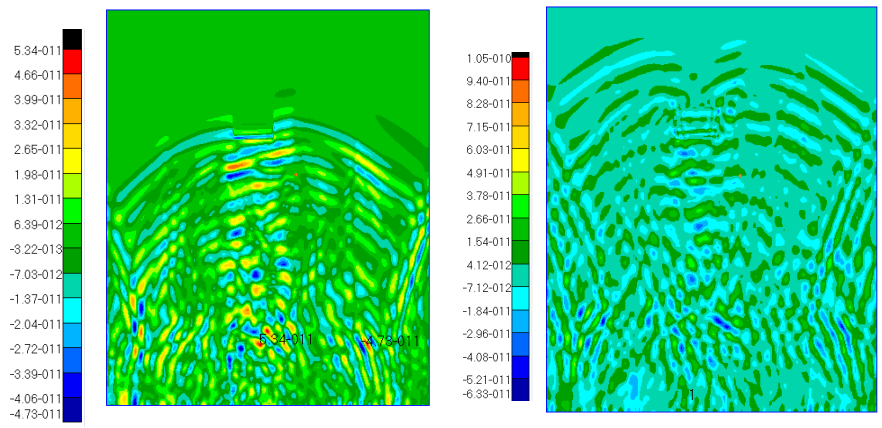

t= 0.080071 ms t= 1.00477 ms

Fig. 4.15 - Field output of the out of plane velocity V_1 for stiffened plate with delamination, modeled with shell elements

4.7. MODELING OF THE EXAMINED PLATE BY SOLID ELEMENTS

In order to perform this second analysis, we used HEX8 elements with eight nodes, whose dimensions are equal to 0.05X0.05X0.05 in^3. This kind of meshing allows a simulation very close to lab test results in Z-direction too, because of the presence of E_{33}, Young's modulus.

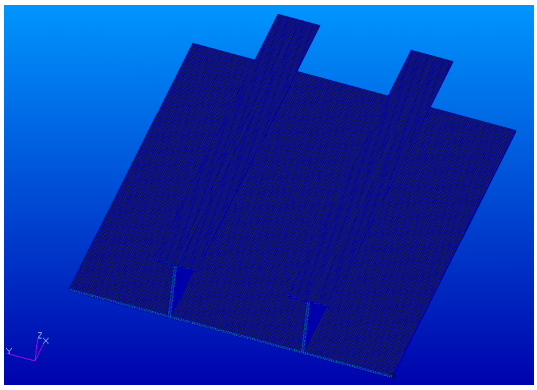

Fig. 4.16 - Cut-off of the total panel meshed with hex8 elements

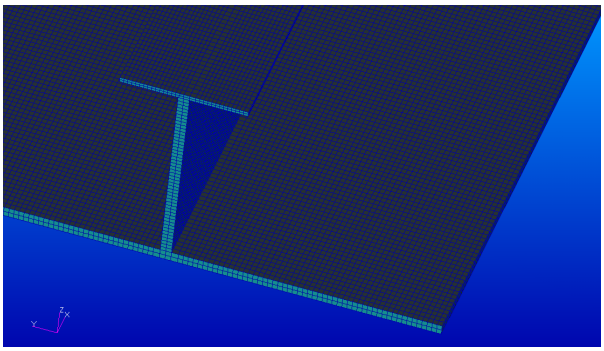

Fig. 4.17 - Enhancement of meshing.

Element type: The elements adopted to model the plate are the ones called HEX8 by MDNastran. This abbreviation defines the connections of the six-sided solid element with eight grid points. The regularity of the mesh is maintained (as in the previous model).

4.8. MATERIAL PROPERTIES AND LAY-UP

The second FE model is similar to the previous one with shell elements: the orientation is the same, the boundary conditions are the same, as well as the dimensions of the plate, the input signal and the output requests. The only differences concern the material adopted and the through-the-thickness refinement. In fact, to describe the orthotropic behavior of laminate, the orthotropic material model, that is available in MDNastran, requires the Young's modulus in the three directions, the three shear moduli and the three Poisson's moduli. Equivalent laminate properties have been applied to the HEX8 elements. The material used for this second model is 3D orthotropic, considering E_{11}, E_{22}, E_{33}, ν_{12}, ν_{23}, ν_{31}, G_{12}, G_{23}, G_{31}, allowing the response of the plate in the Z direction. The subscript 11 is referred to a quantity along the direction of the fiber, the subscript 22 to a quantity directed normal to 11, but in the same plane of the lamina and the subscript 33 to a quantity normal to the plane of the lamina.

4.9. WAVE PROPAGATION IN F.E. MODEL WITH SOLID ELEMENTS

The reported results are the field output representation of the out of-plane velocities V_3 in four time instants, to represent the shape of the wavefront and its evolution. There is no perfect match in frequency because of the too poor elements in the thickness. A refined model with more elements in the thickness direction to exactly reproduce the wavefront propagation not only in wave

shape, but in frequency too is in progress. Such refined analysis will take place only when we'll get higher potency calculation machines.

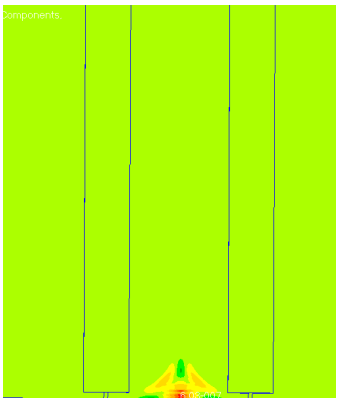

t=0.43094 ms (Stringer side)

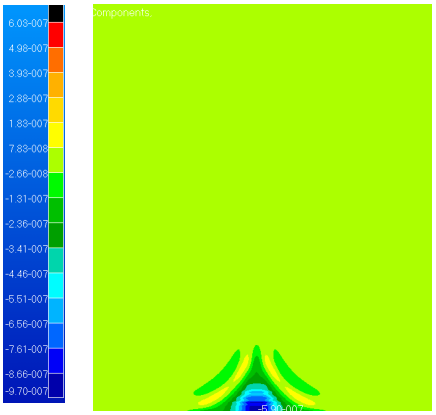

t=0.43094 ms (skin side)

t=2.5279 ms (Stringer side)

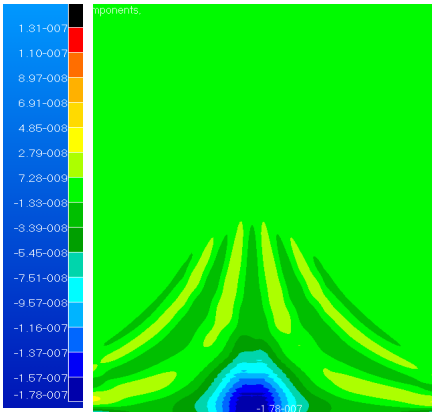

t=2.5279 ms (skin side)

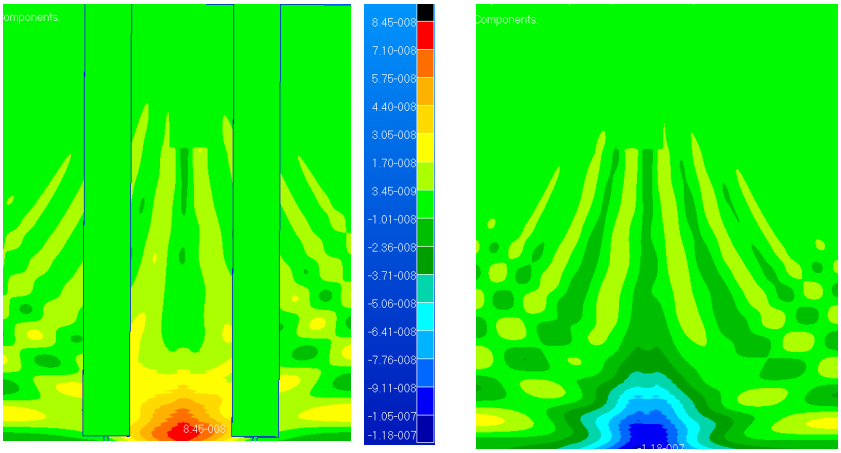

t=4.446832 ms (Stringer side) t=4.446832 ms (skin side)

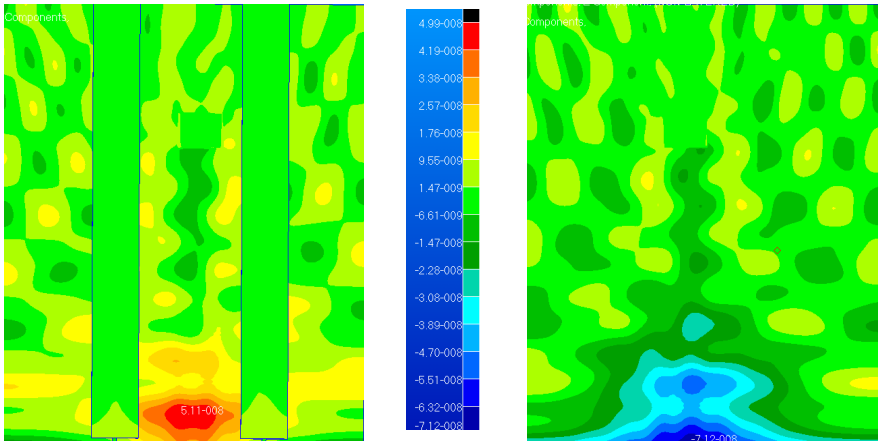

t=4.446832 ms (Stringer side) t=4.446832 ms (skin side)

Fig. 4.18 - Field output of the out of plane velocity V_3 for stiffened plate with delamination, modeled with solid elements

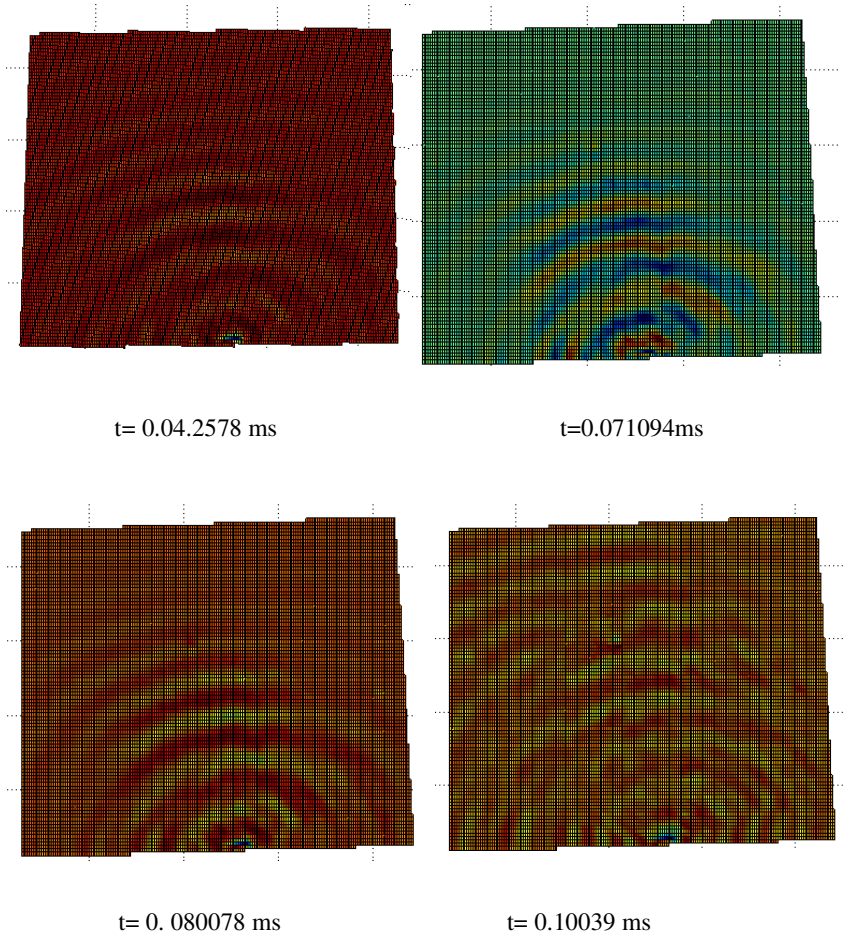

Fig. 4.19 - Plot of the velocity recorded from the laser vibrometry at different time instants.

5. CONCLUSIONS AND FUTURE WORK

This work presents an attempt to integrate modal-based and guided waves inspections, in order to overcome the drawbacks of the two techniques, while combining their advantages. Most of the damage measurements assume the possibility of comparing current measurements with baseline information regarding the undamaged state of the structure. This a significant drawback as it assumes the availability of data on the component under test in its pristine state and the basic assumption that any measured change is due to damage only and not to environmental or boundary conditions changings applied to the component.

The here considered SHM procedure concerns innovative techniques for a structural monitoring of aeronautical components, all of them based upon the use of a Scanning Laser Doppler Vibrometer. The vibrometer is used to detect the dynamic response of the component under test, in wave propagation regime. The signal so recorded consists of space and time maps of vibration velocity off-plane. The purpose of the study lies in the analysis of such maps, using filtering techniques that separate reflected waves from the incident ones, so that they can enable to identify defects. In a SLDV, the laser beam placement is controlled by a user-defined grid on the structure. This offers the possibility of accurately estimating deflection derivatives of various orders and in turn allows the estimation of curvatures and strain energy distributions. Such measurement refinement is unattainable in a timely manner using accelerometers and/or strain gauges. Furthermore, the damage index formulation presented in [30, 27] requires the use of data from an undamaged structure to be used as a reference. This may represent a problem towards the practical implementation of the

technique, as historical data might not always be available, and variations may be induced by a number of reasons other than structural damage. The innovative application of a novel technique (introduced by Ruzzene) for the first time to stringerized composite specimens, allowed the generation of baseline information directly from the measured dataset. Specifically, reference data has been synthesized by under-sampling measurements recorded directly on the damaged specimen.

Furthermore, full wavefield measurements, obtained with a laser scanning vibrometer, were combined with effective signal and imaging processing algorithms to support characterization of guided waves as well as detection, localization and quantification of structural damage. These wavefield images contain a wealth of information that clearly show details guided waves as they propagate outward from the source, reflect from specimen boundaries, and from discontinuities within the structure. The analysis of weaker scattered waves has been facilitated by the removal of source waves and the separation of wave modes, which is effectively achieved via wavenumber–frequency domain filtering in conjunction with the subsequent analysis of the resulting residual signals. Incident wave removal highlighted the presence and the location of weak scatterers, while the separation of individual guided wave modes allowed the characterization of their separate contribution to the scattered field and the evaluation of mode conversion phenomena. The effectiveness of these methods has been demonstrated through their application to detection of a delamination in a composite stiffened plate and detection of defect/wrinkling in a T-shaped skin to stringer component, as shown in chapter 3.

The most significant technological innovations achieved through these theses are:

- The option key to excite the surface of a complex structure (in this case, the skins of a composite stingerized panel) and to derive the velocity profile on surfaces orthogonal to the excited one (in our

case the web of the stringer) has been checked. Obviously, in such a way, it is automatically also validated the opposite approach. This is crucial, as it would allow to install the piezo elements on the stringers, to excite them and to read velocities of points over the entire surface of the skin, without disassembly. Up to now, only cases of standard solicitation have been analyzed in literature, or cases where the velocities were acquired on the same surfaces excited. Today, therefore, there is no published study on the analysis conducted in such a manner.

- The damage index was also applied to stiffened and greatly complex geometries. Up to now, in literature only analysis applied to simple flat panels can be found.
- The FEM simulation was carried out on stiffened panels. In literature there are only simulations carried out on simple structural elements like flat panels without any stiffener.

Furthermore, results put in clear evidence that the match between the data obtained by FEM simulation and those obtained by laboratory tests, although it is only relative to the waveform detected in the two numerical models and not in frequency, is a fundamental starting point, because it has been demonstrated that the shape of the wavefront propagation can also be adequately numerically reproduced in stringerized panels (about these studies there is no existing literature). The subsequent and more immediate development, therefore, is to reproduce even the match in frequencies.

This type of implementation will be performed with the following approach:

- The FEM model will be refined using a larger number of elements along the thickness, in order to calibrate the exact frequency of the excited waves.

- A further development will consist in using the reverse-FEM techniques. This will be achieved by informing the model with experimental data,

i.e. loading the model with the experimental velocities measured on the grid, node by node. Through this type of simulation it will be possible to obtain a large number of detailed local information, not obtainable only with vibrometric relief, such as the stress intensity factor around the delamination (hole).

REFERENCES

[1] Staszewkij, W., Boller C., and G. Tonlinson. (2004). Health monitoring of aerospace structures. *John Wiley & Sons*, West Sussex, England.

[2] Hall S. R. and T. J. Conquest. (1999). "The total data initiative-structural health monitoring, the next generation", *Proc. Of the USAF ASIP, 2nd ed.*

[3] Sohn H., Farrar C. R., Hemez F. M., Sunk D. D., Stinemates D. W. And B. R. Nadler. (2003). Health monitoring of aerospace structures. *John Wiley & Sons*, West Sussex, England.

[4] Worden K. and J. M. Dulieu-Barton. (2005). "A overview of intelligent fault detection in systems and structures", *Struct. Health Mon.* , West Sussex, 3(1), pp. 85-98.

[5] Staszewski W. J., Boller, C., Tomlinson, G. (2004). "Health Monitoring of Aerospace Structures. Smart Sensors And Signal Processing", *Wiley & Sons Ltd.*

[6] Rose, J. L. "A baseline and Vision Of Ultrasonic Guided Wave Inspection Potential", *Journal of pressure Vessel Technology,* Vol. 124, pp. 273 - 282.

[7] Raghavan A., Cesnik C. E. S., (2007). "Review of Guided-wave Structural Health Monitoring", *The Shock and Vibration Digest.*, Vol. 39, N0. 2, pp. 91 – 114.

[8] Doebling . K., Banerjee S., and F. Ricci. (2004). "Automated structural health monitoring system using acoustic emission and modal data", *Proc. Of SPIE.*, 5394, pp. 1 – 10.

[9] Sharma, V., Ruzzene, M., Hanagud, S. (2006). "Perturbation Analysis of Damaged Plates", *International Journal of Solids and Structures*, vol. 43, Issue 16, pp. 4648 – 4672.

[10] Luo, H., Hanagud, S. (1997). "An integral Equation for Changes in the Structural Dynamics Characteristics of Undamaged Structures", *International Journal of Solids and Structures*, vol. 34, pp. 4557 – 4579.

[11] Lestari, W. (2001). "Damage of Composite Structures: Detection Technique, Dynamic response and Residual Strenght", Ph.D Thesis, Georgia Institute of Technology.

[12] Cawley, P., Adams. R. D. (1979). "The Locations of Defects in Structures from Measurements of Natural frequencies", *Journal of Strain Analysis*, 14 (2), pp. 49 - 57.

[13] Stubbs, N., Osegueda, R., (1990). "Global Non-Destructive Damage Evaluation in Solids", *Modal Anaysis: The International Journal of Analytical and Experimental Modal Analysis*, 5 (2), pp. 69 - 79.

[14] Hearn, G., Testa, R. B., (1991). "Modal Analysis for Damage Detection in Structures", *Journal of Structural Engineering* 117 (10), pp. 81 - 97.

[15] Richardson, M. H., Mannan M. A., (1992). "Remote Detection and Location of Structural Faults Using Modal Parameters", *Proc. Of 1oth International Modal Analysis Conference*, pp. 502 - 507.

[16] West, W. M., (1984). "Illustration of the Use of Modal Assurance Criterion to Detect Structural Changes in an orbiter Test Specimen", *Proc. Air Force Conference on Aircraft Structural Integrity,*, pp. 1 - 6.

[17] Yuen, M. M. F., (1985). "A Numerical Study of the Eigenparameters of a Damage Cantilever", *Journal of Sound and Vibration,*, 103, pp. 301 – 310.

[18] Fox, C. H. J., (1992). "The Location of Defects in Structures: A Comparison of the Use of Natural frequency and Mode Shape Data", *Proc. Of 1oth International Modal Analysis Conference*, pp. 522 - 528.

[19] kim, J. H., Jeon, H.-S., Lee, C.-W., (1992). "Application of the Modal Assurance Criteria for Detecting and locating Structural Faults", *Proc. Of 10th International Modal Analysis Conference*, pp. 536 - 540.

[20] Ko, J. M., Wong, C. W. Lam, H. F., (1994). "Damage Detection in Steel Framed Structures by Vibration Measurement Approach", *Proc. Of 12th International Modal Analysis Conference*, pp. 280 - 286.

[21] Zhong, S., Oyadiji, S.O., (2007). "Crack detection in simply supported beams without baseline modal parameters by stationary wavelet transform", *Mechanical Systems and Signal Processing*, 21, pp. 1853 - 1884.

[22] Rucka, M., Wilde, K., (2006). "Application of continuous wavelet transform in vibration based damage detection method for beams and plates", *Journal of Sound and Vibration*, pp. 536 - 550.

[23] Chang, C.C., Chen L.-W., (2005). "Detection of the location and size of cracks in the multiple cracked beam by spatial wavelet based approach", *Mechanical Systems and Sugnal processing*, 19, pp. 139 - 155.

[24] Ho, Y.K., Ewins, D.J., (2000). "Numerical Evaluation of the Damage Index", *Stantford university, Palo Alto, California*, pp. 995 - 1011.

[25] Ho, Y.K., Ewins, D.J., (2000). "On the Structural Damage Identification with Mode Shapes", *European COST F3 Conference on System Identification and Structural Health Monitoring*, pp. 677 - 686.

[26] Kim, J.T., Stubbs, N., "Crack detection in Beam Type Structures using frequency Data", *Journal of Sound and Vibration*, 259 (1), pp. 146 - 160.

[27] Cornwell, P., Doebling, S.W., Farrar, C.R., "Application of the Strain Energy Damage Detection Method to Plate-like Structures ", *Journal of Sound and Vibration*, 259 (1), pp. 146 - 160.

[28] Richardson, M.O.W. and M.J. Wisheart. (1996). "Review of low-velocity velocity impact properties of composite materials," *Applied Science and Manufacturing*, **27A** (12), pp. 1123-1131.

[29] Lestari W. and P. Qiao. (2005). "Damage detection of fiber-reinforced polymer honeycomb sandwich beams," *Composite Structures* **67**, pp. 365-373.

[30] Z. Su, L. Ye, and X. Bu, "A damage identification technique for cf/ep composite laminates using distributed piezoelectric transducers," *Composite Structures*, no. 57, pp. 465–471, 2002.

[31] K. Diamanti, C. Soutis, and J. Hodgkinson, "Lamb waves for the nondestructive inspection of monolithic and sandwich composite beams," *Composites: Part A*, no. 36, pp. 189–195, 2005.

[32] S. Park, C.-B. Yun, and Y. Roh, "Damage diagnostics on a welded zone of a steel truss member using an active sensing network system," *NDT&E International*, no. 40, pp. 71–76, 2007.

[33] K. F. Graff, Wave motion in elastic solids. *Dover Pubblications*, Inc., 1991.

[34] J. L. Rose, Ultrasonic waves in solid media. Cambridge University Press, 1999.

[35] J. D. Achenbach, Wave propagation in elastic solids. Dover Pubblications, Inc., 1984.